Title

Improved Thermochemistry of Zinc Aluminate Interfaces for Enhanced Mechanical Performance at the Nanoscale

Author

Sotelo Martin, Luis Enrique

Publication Date

2022

Peer reviewed|Thesis/dissertation

Improved Thermochemistry of Zinc Aluminate Interfaces for Enhanced Mechanical Performance at the Nanoscale

By

LUIS ENRIQUE SOTELO MARTIN
DISSERTATION

Submitted in partial satisfaction of the requirements for the degree of

DOCTOR OF PHILOSOPHY

in

Materials Science and Engineering

in the

OFFICE OF GRADUATE STUDIES

of the

UNIVERSITY OF CALIFORNIA

DAVIS

Approved:

_____
Ricardo Castro, Chair

_____
Jeffery Gibeling

_____
Klaus van Benthem

Committee in Charge

2022

Table of Contents

List of Figures

List of Tables

Abstract

Nanocrystalline oxides have been studied for their excellent mechanical and optical properties as well as their great chemical stabilities. These properties make them ideal materials for applications such as armored windows, laser gain media, and catalyst supports. Despite their desirable properties, we have a limited understanding of their mechanical behavior at small grain sizes. This makes it difficult to predict and tailor their properties for commercial applications. Furthermore, this class of materials is inherently metastable due to the sizeable energy contributions from their large interfacial areas. This high energy makes them susceptible to coarsening and grain growth which would diminish the properties that make them desirable. This work will focus on addressing these two issues by studying nanocrystalline zinc aluminate ($ZnAl_2O_4$) as a model material. This material was chosen due to its relatively high thermal conductivity which makes it a more attractive material, particularly for laser gain media and catalyst supports, than other oxides.

The first goal of this work will address the interfacial stabilities of zinc aluminate nanoparticles and fully dense samples. Solid-solid (surface) and solid-vapor (grain boundary) interfacial energies were tailored using dopant segregation as predicted by molecular dynamics simulations: atomistic simulations on a nanoparticle and two grain boundary structures were used to assess the segregation behavior of four dopants [Sc^{3+} (74.5 pm), In^{3+} (80.0 pm), Y^{3+} (90.0 pm), and Nd^{3+} (98.3 pm)]. The candidate dopants were chosen to induce segregation by maximizing the elastic strain in the lattice (i.e., large ionic radii). All four dopants were estimated to have favorable segregation energies to surfaces and grain boundaries with Y^{3+} consistently having the lowest energies at interfaces. Accordingly, undoped and doped (0.5 mol% Y_2O_3) were prepared to experimentally compare their interfacial energies and coarsening behaviors. Surface energies were estimated by water adsorption microcalorimetry which revealed that surface stabilities were effectively improved in doped nanopowders, as predicted in simulations. This behavior was correlated with coarsening inhibition and lower estimated diffusion coefficients, indicating Y^{3+} improves zinc aluminate stability against coarsening via kinetics and thermodynamics. Similarly, differential scanning calorimetry was used to measure grain boundary energies as a function of grain size for fully dense samples from both compositions. Grain boundary energies were lower for doped samples at each grain size studied which not only predicts limited grain growth for dense samples, but also elevated hardness and toughness.

The mechanical performance (i.e., hardness and toughness) of Y-doped and undoped samples were compared to identify the effects of improved grain boundary stabilty. Hardness and toughness values were statistically similar for both compositions, indicating the dopant had negligible effects on zinc aluminate mechanical properties using a concentration of 0.5 mol%. The only exception was at larger grain sizes (above 25 nm) where Y-doped samples had significantly higher hardness. This was presumed to be a result of higher concentrations of Y^{3+} in these samples due to lower grain boundary area, hence limiting grain boundary mediated deformation or improving dislocation pinning from dopants segregated to dislocation cores. A more pronounced effect on mechanical properties was found when comparing stoichiometric zinc aluminate (Al:Zn = 2.01:1) to Al-rich zinc aluminate (Al:Zn = 2.87:1). Stoichiometric zinc aluminate exhibited elevated hardness with decreasing grain size until grain sizes of ~20 nm, while Al-rich samples underwent further hardening to grain sizes near 12 nm. Distinct cracking patterns were observed in both samples, suggesting the excess Al postponed the softening by stabilizing high-energy grain boundaries.

The results from this work show that interfacial stability can be enhanced significantly by doping zinc aluminate with $Y^{3+.}$ This can be used to effectively tune zinc aluminate coarsening behavior at the nanoscale. The present work also showed that excess Al can be used to tune the grain size hardening behavior of nanocrystalline zinc aluminate; however, it remains unclear whether a similar effect can be induced by doping with Y^{3+} due to the low concentrations used here. These conclusions will prove beneficial as we employ nanocrystalline ceramics for the next generation of armored windows and catalysts.

Acknowledgements

I would first and foremost like to thank my research advisor Dr. Ricardo Castro for his support and consistent belief in my ability to succeed as a researcher throughout my studies which were key contributors to my success at UC Davis. Dr. Castro's innate scientific curiosity and contributions to the community will continue to inspire me throughout the rest of my professional career. I would also like to thank Dr. Jeffery Gibeling and Dr. Klaus van Benthem for serving on my thesis committee and for their comments that helped shape the formatting of this work. I would especially like to thank Dr. Jeffery Gibeling for helping establish the Jeffrey and Marsha Gibeling Fellowship that financially supported my studies at UC Davis. Likewise, I am thankful for the financial support from the Army Research Office and the National Science Foundation that funded the research projects I worked on during my PhD.

I am grateful for all of the support that I received from my past and present colleagues in the Nanoceramic Thermochemistry Laboratory: Dr. Kimiko Nakajima and Brian Rogers for all of the hours they put into training me on various equipment as well as Isabella Costa and Nicole O'Shea providing helping hands as I wrapped up my experimental work. I would also like to thank Dr. Spencer Dahl for serving as a support system for me as we navigated our doctoral journeys in parallel.

This dissertation would not have been possible without all of the emotional support I received from the friends I met through the Society of Hispanic Professional Engineers (SHPE). I would particularly like to acknowledge all members of the two iterations of the Region 1 Leadership Teams and Region 1 Graduate Committees that I was a part of. Getting to connect with and meet other graduate students and professionals so committed giving back to their communities was truly inspirational. Getting to connect with other graduate students from similar cultural backgrounds on the Region 1 Graduate Committee was a great motivator throughout the last few years.

Lastly, I would like to thank all of my friends and family for their continuous support throughout my time as a PhD student. Out of these, I would especially like to my mother and father for providing me with the best example of true hard work. I could not have made it through this degree without the support of my two sisters: Stephanie and Jessica. Despite being younger than me, their intellect and perseverance in their respective degrees helped motivate me to complete this journey. Of all my friends and family, I would like to thank my girlfriend, Lizeth Hernandez, the most. I could not have finished this degree without her constant reassurance and willingness to come to lab with me late at night or on the weekends. Aside from this, her and her family provided me with a home away from home during my time in Davis.

I hope I can use this degree as a tool to inspire younger Latino students to pursue STEM degrees and to support their careers in any ways possible throughout the remainder of my life.

Chapter 1: Introduction

1.1: Motivation

Nanocrystalline materials have long been topic of interest within the scientific community due to the unique properties they exhibit in comparison to their bulk counterparts[1–8]. This stark contrast between nano and bulk properties is directly related to the substantial increase in interfacial area at the nanoscale: as grain sizes decrease into the nanocrystalline regime, surfaces (solid-vapor interfaces) and grain boundaries (solid-solid interfaces) begin to dictate macroscopic material properties[9–12]. Their optical transparency[4,13–32], elevated hardness (to a degree)[13,24,26,29,33,34], and inherent high specific surface area make nanostructured ceramics prime candidates for applications such as armored windows[15,27,29,34–36], laser gain media[21,22,32,37], and catalysis[38–42] among others.

Grain boundaries and surfaces are highly energetic regions within any given material because of the large quantity of unsatisfied bonds[43–45]. In bulk ceramics, this excess energy is negligible since less than 10% of the material lies within the interfaces[46], but the high interfacial areas present in nanomaterials contribute significantly to their total energies which generally gives rise to poor thermal stability against coarsening[2,45–49]. Attempts have been made to inhibit coarsening in ceramic nanomaterials both on thermodynamic and kinetic fronts which primarily involves the segregation of dopants to interfaces[50–58]. Thermodynamically, dopant segregation reduces the number of unsatisfied bonds in surfaces and grain boundaries which has been proven to successfully stabilize both nanocrystalline metal[59–62] and ceramic interfaces[50–57,63,64]. Dopant segregation also impacts the kinetics of coarsening in dense ceramics; dopants that lie within grain boundary sites provide a drag force which hinders grain boundary mobility, hence limiting grain growth[51,52,54,63,65–68]. The thermal stability of nanocrystalline ceramics is an area of intrigue for ceramic researchers since this defines their viability for commercial applications.

In addition to the thermodynamic complications associated with nanoceramics, our narrow understanding of the mechanisms underlying their mechanical behavior has provided notable research challenges. Grain size hardening, and subsequent softening, have been well-documented in nanostructured ceramics[13,24,26,27,29,33,34,36,69,70] and metals[60,71–74]; however, it is still uncertain whether this behavior is caused by the same mechanisms observed in metals. Dislocation motion, grain boundary sliding, and creep are widely cited as dominant deformation mechanisms in bulk metals, with the latter two becoming increasingly relevant in the nanocrystalline

regime[3,11,59,72,75,76]. Although there is some evidence in literature of these mechanisms being present in nanocrystalline ceramics[13,66,77], this is not well-understood since their ionic nature makes this type of deformation unfavorable at room temperature. Furthermore, there is significant discord surrounding the relationship between grain size and fracture toughness in nanostructured ceramics due to the plethora of limitations associated with accurate determination of fracture toughness values[64,78–81].

My studies will focus on enhancing our current understanding of the thermodynamic and mechanical behaviors of transparent nanoceramics for armored windows. Specifically, analyzing the effects of Al-enrichment and dopant segregation on nanocrystalline zinc aluminate interfacial stability. This work will further elucidate the role of dopants in tuning nanoceramic properties as we continue to assess their viability for commercial applications.

1.2: Hypothesis

The hypothesis of this work stems from previous work on interfacial stabilization of nanostructured materials, proposing that macroscopic properties can be tuned by altering the thermochemistry of interfaces. This collection of studies aims, in part, to correlate the improved interfacial thermodynamics of doped zinc aluminate with enhanced stability against coarsening to complement similar work on other nanocrystalline oxides[50–52,55,57,63]. Another key goal of this work is to expand our knowledge of the relationship between grain boundary stability and mechanical behavior in nanoceramics. There exists an abundance of studies that report weakened nanoceramics, including reduced fracture toughness[8,78,81] and breakdowns in grain size hardening[13,27,33,70] but only recently have we begun to showcase the role of grain boundary stability in controlling these trends[70]. A second goal of this work is to build upon our working knowledge of the interplay between grain boundary stability and mechanical performance of nanocrystalline ceramics by using both Al enrichment and rare-earth doping as methods to alter the stabilities of zinc aluminate grain boundaries. Generally, this work seeks to advance our ability to tune the mechanical and thermal properties of nanoceramics by enhancing interfacial thermodynamics to demonstrate their feasibility for applications such as next-generation armored windows.

1.3: Objectives

1. Juxtapose the grain size hardening behavior of zinc aluminate sintered by two different spark plasma sintering techniques.
2. Experimentally investigate the role of Al enrichment on the grain size hardening behavior exhibited by zinc aluminate.
3. Computationally assess the segregation of an array of dopants to zinc aluminate surfaces and grain boundaries.
4. Experimentally determine the surface energies of undoped and Y-doped zinc aluminate using water adsorption microcalorimetry.
5. Analyze the grain growth behaviors of undoped and doped zinc aluminate.
6. Experimentally determine grain boundary energies of undoped and Y-doped zinc aluminate using differential scanning calorimetry.
7. Compare Vickers hardness and indentation fracture toughness for undoped and Y-doped zinc aluminate.

Chapter 2: Background

2.1: Interfacial Chemistry in Nanocrystalline Ceramics

2.1.1: Surface and grain boundaries in nanomaterials

Material properties are defined by the properties of their bulk and interfacial (solid-solid and solid-vapor) components; however, interfacial effects are often considered negligible in coarse-grained materials. This type of assumption is typically valid due to the limited interfacial areas present in these materials as shown in **Figure 2.1**[33,82]:

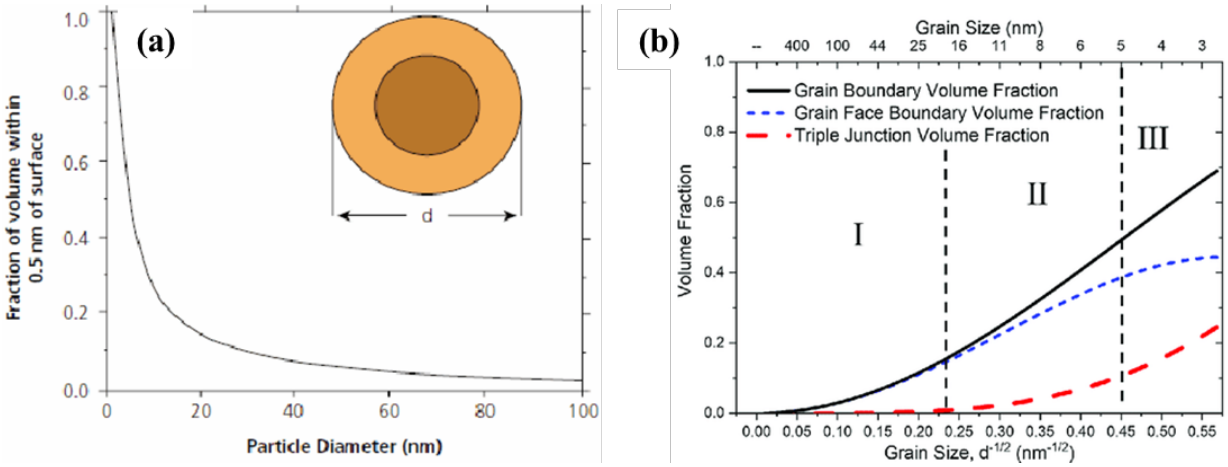

Figure 2.1: Geometric approximations showcasing sharp increases in the percentage of atoms within (a) 0.5 nm of surfaces with decreasing (spherical) particle diameters[82] and (b) 1 nm of grain boundaries with decreasing (tetrakaidecahedron) grain sizes for fully-dense ceramics[33].

The opposite becomes true in the nanoscale; this class of materials, defined by their characteristically-small crystal sizes and high interfacial areas, exhibit properties such as room-temperature creep and superplasticity in metals[83,84] and optical transparency in ceramics[24,30,32] that are limited in their coarse-grained counterparts. Although these properties make nanocrystals prime candidates for a range of applications, their high interfacial areas render them thermally unstable[47,85] and make them susceptible to weak deformation mechanisms at small grain sizes[13,64].

The excess energies associated with grain boundaries and surfaces result from the high number of unsatisfied bonds and are influenced by a number of factors including crystal size, impurity concentration, and misorientation angle (for grain boundaries)[86]. Because of this, researchers have yet to develop experimental methods for measuring individual interfacial energies; although, significant work has been done to measure average surface (γ_s) and grain

boundary energies (γ_{gb}) of nanocrystalline oxides using a variety of calorimetric techniques[54,87–91]. Some of these measurements on model materials like yttria-stabilized zirconia and magnesium aluminate are included in **Table 2.1** below:

Material	**Calorimetric Technique**	γ_{gb} **(J/m^2)**	γ_s **(J/m^2)**	**References**
8YSZ	OMSC[87]	0.73[87]	1.16[88]	Chen et al.[87] Costa et al.[88]
10YSZ	OMSC[88] OMSC[89] DSC[90]	0.68[89] 0.94[90]	1.51[88] 0.69[90]	Costa et al.[88] Chen et al.[89] Li et al.[90]
12YSZ	OMSC[88]	—	1.80[88]	Costa et al.[88]
15YSZ	OMSC[89]	0.64[89]	—	Chen et al.[89]
MAO	DSC[91]	0.57[91]	1.49[91]	Pereira et al.[91]

Table 2.1: Reported values for interfacial energies of different compositions of yttria-stabilized zirconia (8YSZ, 10YSZ, 12YSZ, 15YSZ) and magnesium aluminate (MAO) measured by oxide melt solution calorimetry (OSMC)[87–89] and differential scanning calorimetry (DSC)[90,91].

These measurements have become vital tools for comparing mechanical performance[64,70] as well as sintering behavior[35,63] of various nanocrystalline ceramics while giving researchers a means of quantifying improvements in the relative stabilities of nanoceramic interfaces.

2.1.2: Stabilization of nanoceramic interfaces

The primary method used to improve the energetic landscape of nanomaterials involves saturating dopants at grain boundaries and surfaces to increase their coordination and is commonly referred to as dopant segregation[92]. This technique has been applied to nanostructured metals[59,60] as well as ceramics[50–53,63]. Studies using this technique have reported systematic decreases in interfacial energies as predicted by the Gibbs adsorption isotherm[92]:

$$\gamma = \gamma_0 - \Gamma_B(RTlnX_B - \Delta H_{seg}) \qquad \textbf{(2.1)}$$

where γ is the interfacial (surface or grain boundary) energy with segregated dopants, γ_0 is the undoped interfacial energy, Γ_B is the interfacial excess of the dopant, X_B is the concentration of dopant, and ΔH_{seg} is the segregation enthalpy of the dopant in the system[92]. This model relates an interfacial (surface or grain boundary) energy to the concentration of the dopant in the material, predicting a linear decrease given a spontaneous segregation enthalpy. In practice, this trend holds true until the point where segregation sites are saturated with dopants and further increases in dopant concentration result in second phase formation. This behavior is illustrated in curve (3) of **Figure 2.2** which depicts this linear decrease in interfacial energy and a subsequent plateau indicative of a second phase.

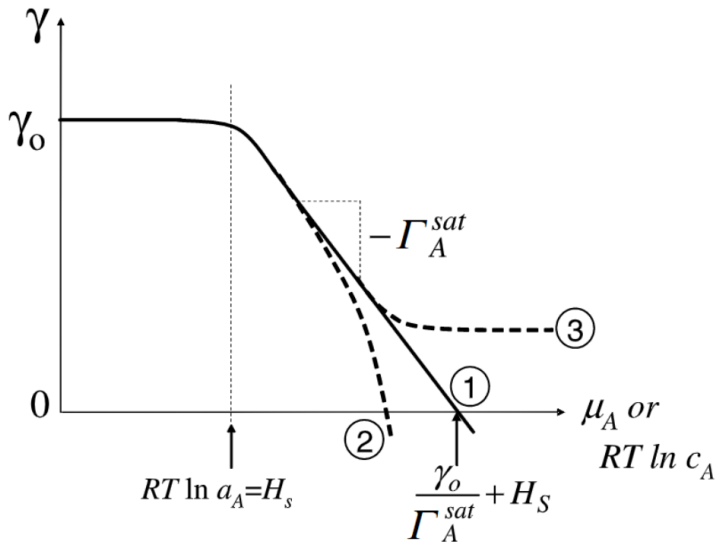

Figure 2.2: Schematic representation of the Gibbs adsorption isotherm applied to dopant segregation as depicted by Kirchheim[92]. The relationship in curve (3) occurs when the system surpasses the point of interfacial saturation, and a dopant-rich second-phase begins to form.

To induce interfacial segregation, **Equation 2.1** states that dopant atoms must have a negative segregation enthalpy within the lattice. Segregation enthalpy is a function of a dopant's electrostatic and elastic interactions with the lattice, so a dopant's charge and ionic radius are key predictors of its ability to segregate to surfaces and grain boundaries[50]. To facilitate segregation, researchers commonly opt for dopants that are isovalent with one of the host atoms, such as La^{3+} in yttria-stabilized zirconia[63,93] or Y^{3+} and Gd^{3+} in magnesium aluminate[53]. Doing so simplifies the defect chemistry associated with segregation by limiting space charge and dipole interactions

between dopant complexes and the lattice, making dopant segregation predominantly a function of elastic mismatch with the host atoms.[94]

The defect chemistry in spinels (AB_2O_4) like magnesium aluminate ($MgAl_2O_4$) and lithium manganese oxide ($LiMn_2O_4$) becomes increasingly complex due to the inversion that occurs between atoms in A and B sites. In magnesium aluminate, this effect has been found to induce self-segregation of Al and Mg atoms due to the enhanced elastic strain from site inversion[95,96]. This self-segregation induces a space-charge layer in spinels that inherently limits the predictability of dopant segregation[94,97]. Despite this, researchers have successfully observed the effects of dopant segregation in spinels[50,55,98]. There have been multiple reports of reduced interfacial energies measured by calorimetry: Hasan et al. found the average grain boundary energy in dense magnesium aluminate to decrease from 0.53 J/m^2 to 0.32 and 0.36 J/m^2 using Gd^{3+} and Y^{3+}, respectively[50]. Nakajima et al. achieved comparable results by doping lithium manganese oxide with Sc^{3+}; in this case, average surface and grain boundary energies decreased by 44% and 11% each[98]. Despite the limited effect on the system's grain boundary energy, Nakajima et al. observed a clear segregation to the grain boundary region using electron energy loss spectroscopy as shown in **Figure 2.3**[98]:

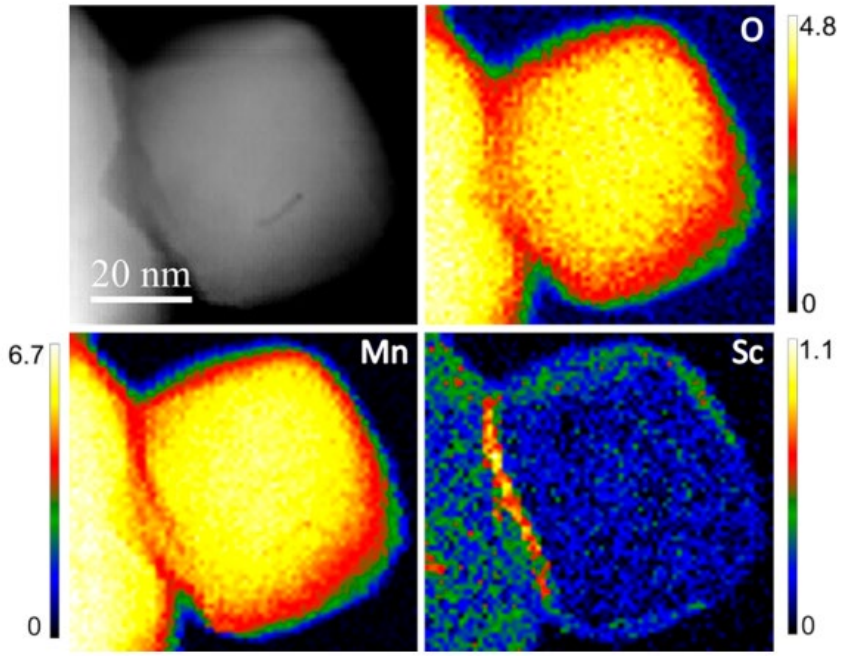

Figure 2.3: Electron energy loss spectroscopy maps of Mn, O, and Sc in Sc-doped lithium manganese oxide nanoparticles by Nakajima et al.[98]. The red-orange contrast in the Sc map represents Sc decorating the grain boundary region of the nanoparticle system.

Given the high interfacial area of nanocrystalline ceramics, even marginal improvements to interfacial energies have significant implications on their macroscopic properties and potential applications. This idea has made solute segregation and interfacial engineering a prominent area of research within the materials science community and enabled the tunability of mechanical performance and coarsening behavior at the nanoscale.

2.2: Enhanced Stability Against Coarsening in Ceramic Nanoparticles

Ceramic nanoparticles normally grow by Ostwald ripening – evaporation of smaller particles onto larger ones driven by the high curvature (or high surface energy) of small particles[99,100]. This process is defined by **Equation 2.2** developed by Lifshitz and Slyozov which states that particle radii grow according to $t^{1/3}$:

$$R_t^3 - R_0^3 = \frac{8\gamma_s c_\infty V_m D}{9RT} t \qquad \textbf{(2.2)}$$

where R_t is the particle radius at time t, γ_s is the surface energy, c_∞ is the solubility limit of the particle, V_m is the molar volume, D is the self-diffusion coefficient, R is the ideal gas constant, and T is the temperature[101]. The characteristic equation for Ostwald ripening indicates that high surface stabilities and limited diffusion are required to impede nanoparticle growth. The previous section featured an in-depth discussion on how dopant segregation can be utilized to enhance nanoparticle stability, but **Equation 2.2** reveals that diffusion must also be discussed to fully understand a system's propensity for growth.

Material diffusion rates are functions of the individual diffusion rates of their species; for example, self-diffusion rates in magnesium aluminate and cerium oxide are determined by the slow diffusion of oxygen vacancies in the lattice[100,102]. This suggests that diffusion and growth of magnesium aluminate and ceria nanoparticles can be hindered by limiting the formation of oxygen vacancies. A study by Ting and Lu looked to compare the defect concentrations in magnesium aluminate samples with varying Al contents: Mg-rich, stoichiometric, and two Al-rich concentrations[102]. The following Brouwer diagram was developed to explain the effects of increasing Al content on the presence of oxygen vacancies:

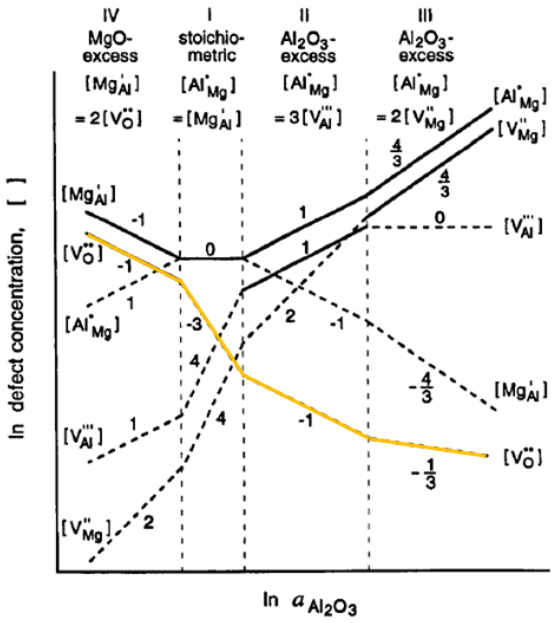

Figure 2.4: Brouwer diagram developed by Ting and Lui demonstrating the dominant defects present in magnesium aluminate at four different Al_2O_3 concentrations modified to highlight the concentration of oxygen vacancies[102].

Ting and Lu concluded from this that adding excess Al into magnesium aluminate will suppress the formation of oxygen vacancies to compensate for the excess positive charge in the system[102]. The opposite is also true: looking at hypo-stoichiometric concentrations (i.e., Mg-rich), the number of oxygen vacancies increases to accommodate for negatively charged defects[102]. This result can be easily translated to the concept of dopant segregation to predict changes in defect chemistry. Introducing trivalent dopants into otherwise stoichiometric magnesium aluminate nanoparticles will generate positively charged defects which limit the formation of oxygen vacancies which, in turn, would hinder Ostwald ripening.

Furthermore, it is vital to understand the relationship between kinetics and thermodynamics in determining particle growth behavior. These two mechanisms can either work concomitantly to limit Ostwald ripening (e.g., by decreasing diffusive properties and enhancing surface stability) or compete if they have opposing effects. The latter was discussed by Wu et al. in Mn-doped ceria nanoparticles where surface energies were improved while diffusion was accelerated[100]. In this work, it was presumed that adding Mn^{3+} to ceria nanoparticles would facilitate the formation of oxygen vacancies: cerium exists in the 4+ state which makes Mn^{3+} substitution a negatively

charged defect[100]. In itself, this would predict an increase in ceria growth rates; however, coarsening inhibition was instead reported due to the decrease in surface energies from Mn^{3+} surface segregation[100]. Researchers typically design systems to prevent this competition by favoring both thermodynamics and coarsening. Gouvêa et al. studied tin oxide nanoparticles doped with magnesium oxide to target reduced coarsening[103]. Doped nanoparticles also resisted growth here, but it was believed that this system had both limited diffusion and improved surface stabilities relative to the undoped case[103].

Similar behavior can be induced at grain boundaries to limit sintering and grain growth in dense nanoceramics[52,54,104]. Some cases of this include reduced grain growth in dense Gd-doped zirconia[52] and Y-doped magnesium aluminate[50]. However, this behavior will not be discussed in detail here since the scope of this work will instead focus primarily on the growth behavior of ceramic nanoparticles.

2.3: Grain Size Hardening in Nanocrystalline Ceramics

Nanocrystalline metals are commonly reported to possess enhanced hardness and toughness as a result of increased dislocation density relative to bulk materials[3]. Although comparable results have been reported for nanoceramics[24,26,33,34,64,70], trends remain unpredictable even within the same material systems. Inconsistent results have typically been attributed to a number of reasons including residual stress from sintering, nanopores, and second phase precipitation[105]. To improve our control over the mechanical behavior of nanostructured ceramics, it is first necessary to enhance our understanding of the dominant deformation modes in the nanocrystalline regime.

Research on mechanical behavior of nanoceramics has primarily focused on grain size hardening due to the reproducibility and simplicity associated with indentation testing[24,26,33,34,64,70]. Numerous studies have attempted to estimate fracture toughness of such materials by means of indentation[64,106] despite the well-documented limitations associated with the technique[80,107]. Conclusions drawn from both hardness and indentation toughness measurements will both be discussed here to provide an overview of our current understanding of nanoceramic mechanical performance.

The ionic character of ceramics has led researchers to believe that dislocations have a minimal role in dictating their mechanical behavior[108]. Despite this, the ceramic community has

drawn parallels between grain size hardening in ceramics and the Hall-Petch behavior in metals[24,26,33]. Hall-Petch strengthening is a well-known phenomenon that relates a metal's yield strength to its average grain size (D), stating that strength scales with $D^{-0.5}$ as in **Equation 2.3**:

$$\sigma_{HP} = \sigma_0 + kD^{-0.5} \quad \textbf{(2.3)}$$

where σ_{HP} is the yield strength at a given grain size, σ_0 represents the dislocation movement resistance within polycrystalline grains, D is the grain size, and k is the Hall-Petch slope[72]. This equation is normally adapted for Vickers hardness to describe the improved hardness in ceramics at small grain sizes[24,26,33].

It has been widely acknowledged that the Hall-Petch relationship breaks down at low grain sizes in metals as grain boundary deformation (e.g., creep and grain rotation) become dominant[105,109]. The existence of such a breakdown is controversial for ceramics since both trends have been reported at small grain sizes even in the same material[24,27,33,34]. The opposing trends are depicted in **Figure 2.5** which includes plots of Vickers hardness against grain size in the Hall-Petch form for two different studies on magnesium aluminate:

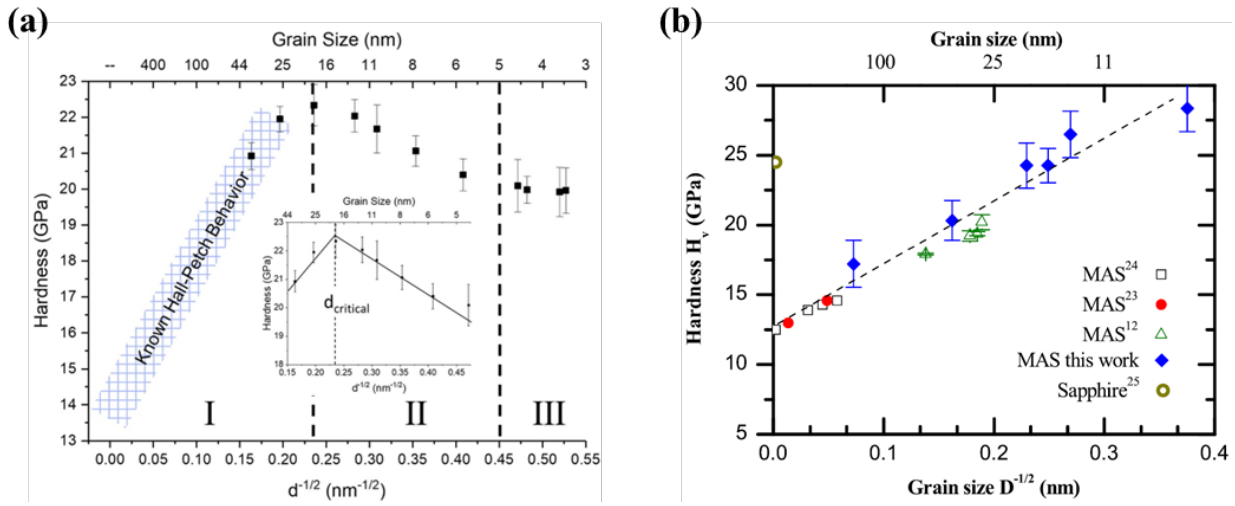

Figure 2.5: Vickers hardness plotted against the inverse square root of grain size from studies by (a) Ryou et al. on nanocrystalline magnesium aluminate sintered using a multianvil apparatus[33] and (b) Muche et al. on nanocrystalline magnesium aluminate sintered by deformable-punch spark plasma sintering[24].

Ryou et al. reported enhanced hardness in magnesium aluminate as grain sizes approached 18 nm; however, further decreases in grain sizes led to an inversion in the Hall-Petch relationship

(**Figure 2.5a**)[33]. Ryou et al. correlated the critical grain size for this breakdown with an appreciable increase in the volume fraction of triple junctions (estimated geometrically assuming tetrakaidecahedron grains) in magnesium aluminate, suggesting the Hall-Petch breakdown could result from elevated crack nucleation at the intersection between grains[33]. On the other hand, Muche et al. did not noticed any softening in magnesium aluminate down to grain sizes of 7.1 nm (**Figure 2.5b**)[24]. This extended grain size hardening was attributed to improved stability in grain configurations from using compliant punches during spark plasma sintering[24]. The inconsistencies between these studies highlight our limited control over grain size hardening in ceramics and indicate that more work must be done to understand the deformation mechanics in these systems.

Studies on nanoceramic deformation have primarily focused on the analysis of milled cross-sections below indentation surfaces and have helped identify the presence of extensive crack networks, shear bands, and dislocation pileups underneath indentations[13,26,70]. Images from representative studies are included in **Figure 2.6** below:

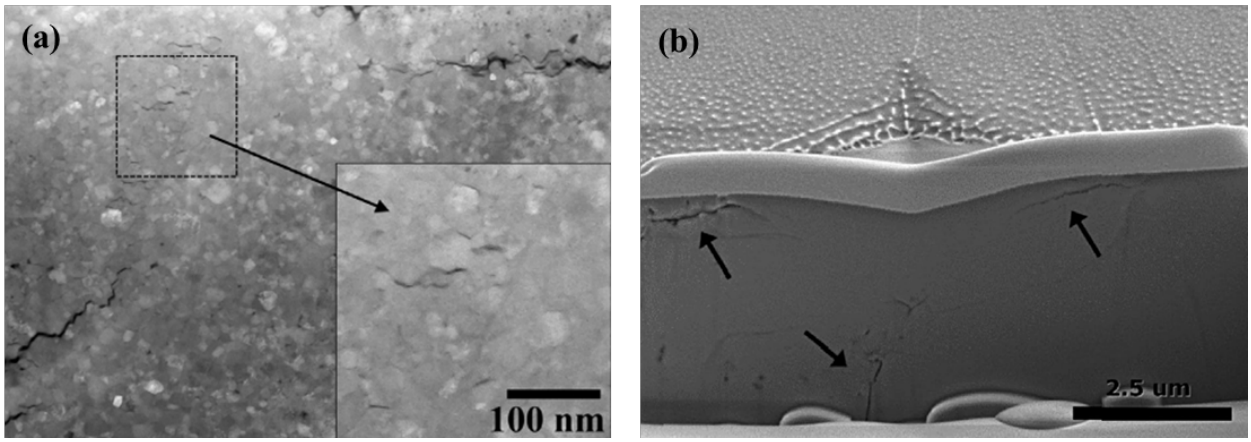

Figure 2.6: (a) High angle annular dark field image of a cross-section milled underneath indentations on a magnesium aluminate sample with average grain sizes of 22 nm by Ratzker et al.[13] and (b) scanning electron microscopy image of an indentation cross-section in a zinc aluminate sample with an average grain size around 10 nm by Yang et al.[26].

The image from Ratzker et al. shows shear bands underneath a magnesium aluminate indentation which confirms that grain boundary plasticity is active in nanocrystalline ceramics[13]. Other images in this study showed a substantial number of dislocations present in larger-grained (~40 nm) samples, which suggests that grain size hardening in ceramics may be dominated by the same mechanisms as in metals, with a transition to grain boundary deformation at small grain

sizes[13]. Similarly, Yang et al. looked at milled cross-sections of zinc aluminate samples to analyze the crack patterns[26]. The image in **Figure 2.6b** captured an extensive network of lateral cracks in small-grained samples, which highlights the role that cracks may have in the Hall-Petch breakdown: despite not measuring any softening in this study, the increased cracking serves as a hint that this may occur with further decreases in grain size[26].

Other studies have focused on predicting mechanical performance by looking at trends in grain boundary energies[64,70]. Bokov et al. measured hardness as a function of grain size for nanocrystalline yttria-stabilized zirconia to compare this with average grain boundary energies measured by differential scanning calorimetry[70]. They found that the critical grain size for the Hall-Petch breakdown coincided with an increase in the average grain boundary energy as shown in **Figure 2.7** below:

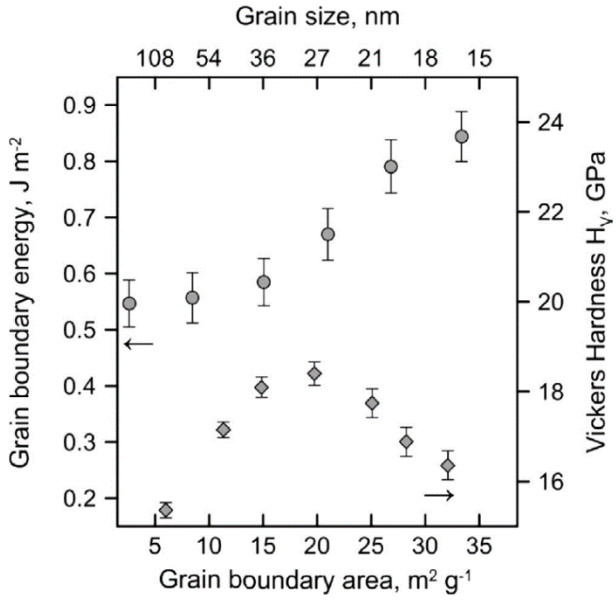

Figure 2.7: Grain boundary energies and Vickers hardness of nanocrystalline yttria-stabilized zirconia plotted as function of grain boundary area by Bokov et al.[70].

It can be assumed that this increase in grain boundary energy at small grain sizes is activating grain boundary deformation mechanisms as noted by Ratzker et al.[13] which, in turn, results in lower hardness at these grain sizes. By generalizing this result, one can hypothesize that mechanical behavior of nanocrystalline materials can be controlled by tuning grain boundary energies.

In the previous sections, we discussed using dopant segregation to improve the coarsening behavior of ceramic nanoparticles by leveraging the Gibbs adsorption isotherm[92]. By applying this idea instead to grain boundaries, we can envision improved control over mechanical properties in nanostructured materials. There have already been several reports of enhanced hardness by doping nanocrystalline metals[59,110], but this idea has yet to be applied to study hardness in ceramics. A separate study by Bokov et al. investigated indentation fracture toughness in nanocrystalline yttria-stabilized zirconia doped with various amounts of La^{3+} and found that toughness was proportional to the dopant concentration[64]. It was concluded that La^{3+} preferentially segregated to high-energy grain boundaries which led to enhanced crack branching in doped samples[64]. This result highlights the role of grain boundary thermodynamics in defining the mechanical properties of nanocrystalline ceramics and forecasts one focus of this work.

Chapter 3: Grain Size Hardening in Stoichiometric and Al-Rich Zinc Aluminate

Abstract

The increase in hardness with decreasing grain size is a well-known size effect known as the Hall-Petch relationship. In ceramics, there has been controversy surrounding the existence of a low size limit below which size-induced hardening no longer occurs and softening is observed instead. Here, this so-called inverse Hall-Petch relationship was observed in quasi-stoichiometric dense nanocrystalline zinc aluminate while an extension of the normal Hall-Petch behavior was demonstrated by Al-rich zinc aluminate nanoceramics. Vickers hardness increased with grain refinement for quasi-stoichiometric samples prepared by High Pressure Spark Plasma Sintering, exhibiting a maximum of 18.6 GPa at a grain size of 21.4 nm. Conversely, Al-rich zinc aluminate produced by the same technique strengthened up to 19.2 GPa at 12.6 nm grain sizes. Cross-sections of Vickers indentation imprints showed that while quasi-stoichiometric zinc aluminate showed a change in sub-surface cracking pattern from larger to smaller grain sizes (before and after the Hall-Petch breakdown), the Al-rich samples had sub-surface cracking similar to those found in large grain sizes in quasi-stoichiometric samples. These results suggest that softening at small grain sizes is driven by the activation of shear and fracture at weak grain boundaries which can be mitigated by Al enrichment.

3.1: Introduction

The observed strengthening of polycrystalline materials with decreasing grain size is known as the Hall-Petch relationship[75,76] and follows the empirical relation:

$$\sigma_{HP} = \sigma_0 + kD^{-0.5} \quad \textbf{(3.1)}$$

where σ_0 is known as dislocation movement resistance within polycrystalline grains, D is the grain size, and k is the so-called Hall-Petch slope. This relation has been reported in a wide variety of materials and grain sizes[24,26,34,72,111–113] with proposed mechanisms usually being dislocation dynamics and interactions with grain boundaries[113]. Although the intrinsic network of ionic and covalent bonds significantly limits dislocation density in ceramics, the linear dependence between micro-hardness and the inverse square root of grain size is still believed to result from grain

boundary effects on dislocation motion. It has been proposed that increasing grain boundary area leads to Hall-Petch strengthening by augmenting dislocation pile-ups at grain boundary regions[69,114]. However, the grain boundary region itself becomes increasingly relevant as the stress surpasses the dislocation slip energy release capacity, thus activating a second mechanism of strain accommodation. This is referred to as the quasi-plasticity model[24,26] which suggests that grain boundary shearing enhances strain accommodation and leads to elevated hardness with decreasing grain size.

An inverse Hall-Petch relation is commonly observed in metals[67,71,73,74,115,116] when grain sizes are in the low nanometer range (typically below 10 nm). This is associated with a transition in the dominant load-accommodation mechanism from dislocation-based plasticity to grain boundary sliding[75]. There is still discord regarding the presence of an inverse scaling law in nanoceramics[24,26,27,33,34]. For example, Ryou et al. observed the decrease in hardness with decreasing grain size in magnesium aluminate with grains refined below 18.4 nm[33]. On the other hand, Muche et al. sintered the same spinel to a grain size of 7.1 nm and did not detect significant softening, attributing this behavior to grain shearing as stated in the quasi-plasticity model[24,34]. The inverse relation was also observed by Sokol et al.[27] challenging the data presented by Muche et al.[24], but they did not discuss the underlying deformation mechanisms that may be responsible for the observed relation.

Ryou et al. pointed out a direct correlation between the breakdown of the Hall-Petch relation and an increase in the volume fraction of grain boundary triple junctions, suggesting the suppression of grain boundary sliding may lead to nanocracks near triple junctions and in turn, decreasing hardness[33]. However, nanocracks have been directly observed underneath indentations on zinc aluminate nanoceramics without a Hall-Petch inversion[26]. Complementing concepts introduced by Ryou et al. and Yang et al. propose that crack patterns and associated energies dictate the dominant load accommodation mechanism and therefore govern grain size hardening (or softening) in nanoceramics. This concept was further supported by Bokov et al., who demonstrated a correlation between increasing grain boundary energy and the onset of the inverse Hall-Petch relation in yttria-stabilized zirconia[70]. By definition, grain boundaries bring excess energy to the system as they constitute locally unsatisfied chemical bonds and ionic coordination. Bokov et al. reported that the population of high-energy grain boundaries grows as grain sizes decrease in nanoceramics[70]. This leads to weaker interactions between grains which facilitates intergranular

fracture under indentation. The low activation energy for fracture manifests itself as a decrease in hardness following the inverse Hall-Petch relation. This proposed relationship between grain boundary energy (or grain boundary strength) and Hall-Petch behavior suggests that the inverse Hall-Petch relation could be mitigated by avoiding an increase in grain boundary energy, suggesting 'colossal' hardening may be achieved in nanoceramics[70].

Yang et al. have shown that an inverse Hall-Petch slope is not observed in zinc aluminate down to grain sizes around 10 nm[26]. Like Muche et al., the samples were fabricated using deformable-punch spark plasma sintering (DP-SPS). This technique uses a complying WC punch designed to deform in the final stages of sintering, causing full densification with minimal grain growth. This technique differs fundamentally from Ryou et al.'s approach that uses a multianvil boron nitride die[33], which is akin to Bokov et al.'s high-pressure spark plasma sintering (HP-SPS) setup[70] that uses diamond-SiC punches. Since both Ryou et al. and Bokov et al. report the existence of an inverse Hall-Petch, it is tempting to attribute the extended Hall-Petch relationship observed by Muche et al. and Yang et al. to the DP-SPS fabrication technique and its effects on material structure.

The effect of off-stoichiometry has not been well studied in the context of the Hall-Petch relation despite its potential for altering grain boundary properties. For example, it has been reported that grain boundary chemistry varies in magnesium aluminate depending on the cationic excess[117]. Al-rich samples show excess Al^{3+} cations in the grain boundary regions, affecting the local space charge layer and phenomena such as grain boundary migration[96]. Similarly, Yang et al. illustrated the effect of zinc aluminate non-stoichiometry on grain boundary energetics and showed that increasing the ratio of Al:Zn can suppress coarsening during sintering[118]. Considering the large fraction of grain boundaries in the nanocrystalline regime, interfacial chemistry can play a significant role in dictating the dominant load accommodation mechanism. To our knowledge, there are no studies discussing the role of stoichiometry on the mechanical properties of zinc aluminate nanoceramics.

In this study, a quasi-stoichiometric nanocrystalline $ZnAl_{2.01}O_4$ powder and an Al-rich $ZnAl_{2.87}O_4$ nanopowder were synthesized via co-precipitation to juxtapose the effects of sintering conditions and stoichiometry on the hardness of zinc aluminate nanoceramics. Nanopowders were sintered with HP-SPS utilizing inner punches composed of a diamond/SiC composite as well as DP-SPS using compliant WC inner punches to different grain sizes. These samples were then

indented to determine Vickers hardness. The results reveal that the sintering technique is not sufficient to reverse the hardness trend in dense nanocrystalline zinc aluminate but suggest the Hall-Petch inversion could be postponed with Al excess.

3.2: Experimental Procedures

3.2.1: Synthesis and nanopowder characterization

Nanocrystalline $ZnAl_{2.01}O_4$ (S-ZAO) powder was synthesized through a modified co-precipitation route[26,118]. $Zn(NO_3)_2 \cdot 6H_2O$ and $Al(NO_3)_3 \cdot 9H_2O$ (Sigma Aldrich, >98%) were dissolved in deionized water in the metal stoichiometric molar ratio of 1:2. Prior to synthesis, water contents were measured for both nitrate powders to ensure the stoichiometric ratio was maintained. The pH was kept at ~8.5 throughout the synthesis to inhibit formation of $Zn(NH_3)_4^{2+}$: the stability of the complex would reduce the amount of Zn^{2+} ions in the precipitate leading to an Al-rich environment[26,118]. The precipitate was washed three times with ethanol then dried in an oven at 80°C for 72 hours.

Upon drying, the hydroxide was ground into a fine powder and calcined in a Thermo Scientific Lindberg/Blue M (Thermo Fisher Scientific Inc., Waltham, MA) box furnace at 550°C for 4 hours. The calcination temperature was chosen to ensure complete crystallization while limiting grain growth using results from a high temperature x-ray diffraction (XRD) study on a Bruker D8 (Bruker, Billerica, MA) operated at 40 kV, 40 mA (CuKα radiation, λ=1.5406 Å). $ZnAl_{2.87}O_4$ (E-ZAO) powder synthesized according to Yang et al[26,118] was instead calcined at 630°C for 4 hours in the same furnace. Zinc aluminate nanoparticles were analyzed by XRD to perform phase and crystallite size analysis with whole pattern fitting in the JADE 6.1 (Materials Data Inc., Livermore, CA) software. Powder diffraction file #05-0669 was used for all x-ray analysis.

3.2.2: Spark plasma sintering

Synthesized nanopowders were degassed at 400°C for 16 hours in a Micromeritics SmartVacPrep (Micromeritics Instrument Corp., Norcross, GA) then transferred to a glovebox kept in a dry nitrogen atmosphere to keep nanoparticles moisture-free. Two previously proven spark plasma sintering (SPS) techniques were used to sinter zinc aluminate: high-pressure spark

plasma sintering (HP-SPS)[27,64,70,93] and deformable-punch spark plasma sintering (DP-SPS)[24,26,34]. For both techniques, powder was loaded into dies inside the glovebox to minimize exposure time in atmospheric air then quickly transferred to SPS model 825S (Syntex Inc., Kawasaki, Japan).

The HP-SPS setup used a die (inner diameter (ID): 4 mm, outer diameter (OD): 19 mm) made of diamond/SiC composite (Hyperion Materials & Technologies, Deerfield Beach, FL). Punches with the same diameter composed of the same material were placed on the top and bottom of the die to transfer the load. This setup was placed inside a graphite die (ID: 19 mm, OD: 45 mm) to ensure sufficient electrical conductivity. The DP-SPS setup involved a graphite die (ID: 5 mm, OD: 19 mm) with 5 mm diameter punches made of cemented tungsten carbide (WC)–6% Co that was then placed inside a larger graphite die. The WC punches undergo plastic deformation at elevated temperatures/pressures which allows grains to slide at the punch/sample interface. The surfaces of the WC punches that were in contact with the sample were polished and coated in a thin layer of boron nitride to avoid contamination and serve as a lubricant for removal of the sintered pellet. After either DP-SPS or HP-SPS sintering, each pellet was annealed at 150°C below its sintering temperature to release any residual strain and allow for oxidation of carbon or any potentially reduced elements.

3.2.3: Pellet characterization

Electron microprobe analysis (EMPA) was performed using a Cameca SX-100 (Cameca, Gennevulliers, France) electron microprobe to confirm stoichiometry on one sintered pellet from each synthesis batch. Atomic counts were measured at 10 different points on each pellet and averaged to give an Al:Zn ratio of 2.01:1 for S-ZAO and 2.87:1 for E-ZAO.

Relative densities were measured for most pellets using Archimedes' principle which revealed an average density of 4.53 (±0.05) g/cm^3 for S-ZAO and 4.20 (±0.05) g/cm^3 for E-ZAO samples. Because SEM images showed absence of porosity, the difference in densities can be attributed to distinct stoichiometries and does not necessarily indicate varying degrees of porosity.

Crystallite sizes were calculated for all pellets using XRD and confirmed by imaging on a FEI Nova NanoSEM 430 (FEI Company, Hillsboro, OR) scanning electron microscope (SEM) to represent grain sizes. Pellets were sputter-coated in a 30-50 nm layer of carbon for improved resolution. A minimum of 300 grains were counted for each sample using the ImageJ software.

Extensive SEM analysis was performed to confirm lack of porosity in samples, and none could be found.

Transmission electron microscopy (TEM) sample preparation was performed using a lift-out routine on a Thermo Scientific Scios DualBeam SEM/FIB (Thermo Fisher Scientific Inc., Waltham, MA). The Scios is equipped with a Ga ion column and Thermo Fisher Scientific Easy-Lift lift-out needle. The lift-out routine and settings for each step followed those described by Schaffer et al. and Baram et al.[119,120]. High-resolution TEM (HRTEM) micrographs were acquired using a JEOL JEM 2100F-AC transmission electron microscope (JEOL Ltd., Tokyo, Japan) at an accelerating voltage of 200 kV and a convergence setting of Alpha 2. A Gatan Rio 16 camera (Gatan, Pleasanton, CA) was used to record images.

Pellets were cleaned with acetone to remove excess adhesives and polished again down to 0.1 μm diamond paste to remove residual gold, palladium, and carbon. An Evolution 220 Spectrometer (Thermo Fisher Scientific Inc., Waltham, MA) was used along with the OOIBase 32 software to record and analyze UV/Vis in-line transmission spectra. Before measurements, an empty sample holder was placed between the light source and detector to establish a baseline; for measurements, pellets were fixed on the holder.

3.2.4: Hardness testing

Obtained pellets were polished down to 0.1 μm diamond paste to ensure flat surfaces for hardness testing. Microindentations were performed with a Vickers pyramid on a Mitutoyo HM-220A (Mitutoyo Corporation, Sakado, Japan) applying a constant load of 40 gf. Preliminary tests showed that higher loads caused significant spallation in the indentation zone. Therefore, this study focused on 40 gf indentations with minimal to no spallation to assess the intrinsic property of the nanoceramics, consistently with Ryou et al. who noted a reduction in hardness with increased spallation[33]. There is evidence to suggest indentation load has little to no effect on Vickers hardness in zinc aluminate if spallation is not observed[26]. Therefore, to determine hardness, 5-10 spallation-free indents were imaged under SEM for each sample after sputter-coating in a 5 nm gold/palladium for better resolution.

Sub-cracking mechanisms present during microindentation experiments were investigated by sectioning indents using focused ion beam (FIB) on a Thermo Scientific Scios DualBeam SEM/FIB (Thermo Fisher Scientific Inc., Waltham, MA). Initially, a 2 μm-thick W coating was

deposited onto the indents to protect from ion beam damage. This was followed by gradual removal of the material with a Ga-ion beam with 30 kV accelerating voltage and 1-30 nA of current.

3.3: Results

3.3.1: Microstructural characterization

Figure 3.1 shows x-ray diffraction (XRD) patterns for quasi-stoichiometric (S-ZAO) and Al-rich (E-ZAO) zinc aluminate nanopowders following calcination at 550°C and 630°C for 4 hours, respectively. Both XRD patterns reveal single phases with peaks corresponding to the characteristic spinel structure. Peaks are significantly broad in both cases, leading to calculated crystallite sizes of 6.0 nm and 7.6 nm for S-ZAO and E-ZAO, respectively. **Figure 3.2** shows TEM images of the dispersed powders, showing relatively isotropic particles with grain dimensions consistent with crystallite sizes calculated from XRD. There was no significant difference in agglomeration and particle morphology between the two compositions.

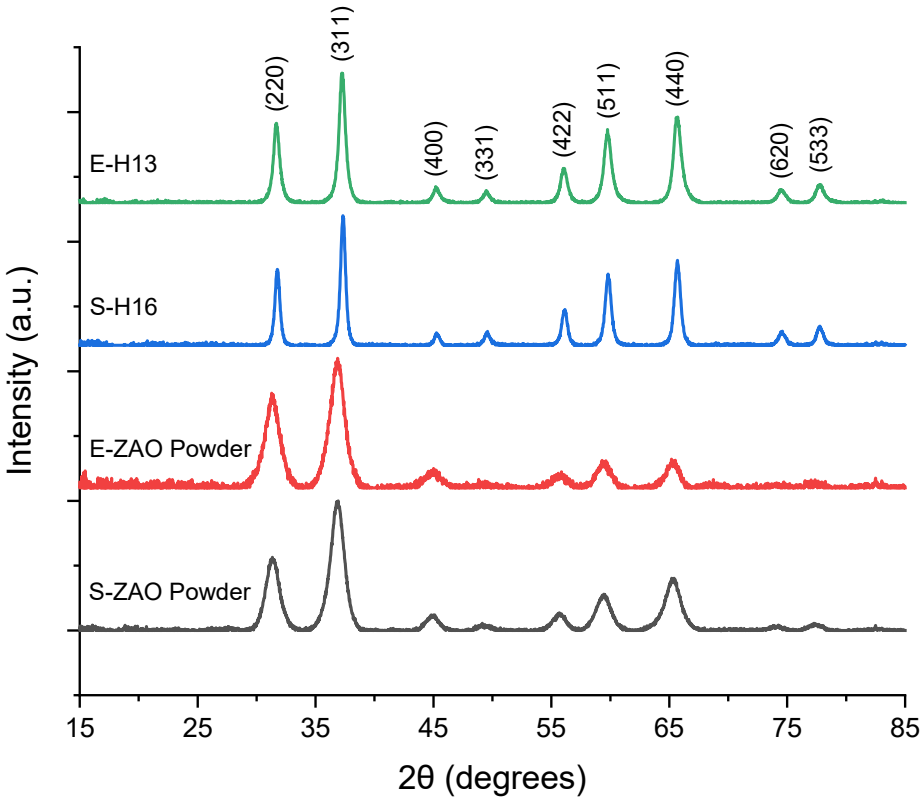

Figure 3.1: X-ray diffraction patterns of S-ZAO (calcined at 550°C for 4 hours) and E-ZAO (calcined at 630°C for 4 hours) nanopowders along with sintered pellets S-H16 and E-H13. Peak sharpening in pellet patterns is due to grain growth during sintering.

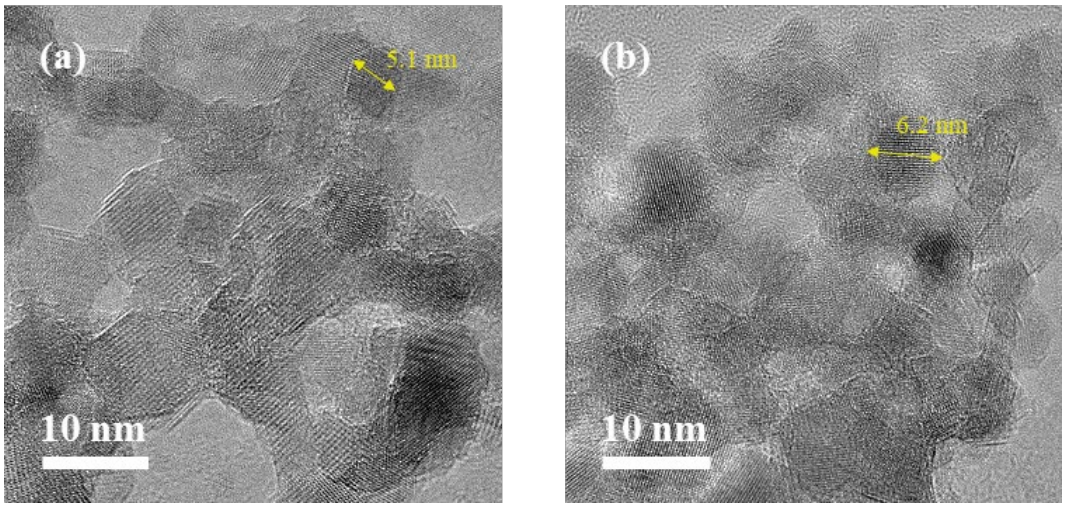

Figure 3.2: Bright field transmission electron microscopy (TEM) images taken of (a) S-ZAO nanoparticles calcined at 550°C for 4 hours and (b) E-ZAO nanoparticles calcined at 630°C for 4 hours. The images show uniform particles with sizes consistent to those measured using x-ray diffraction.

The powders were subjected to densification with spark plasma sintering (SPS) utilizing either the deformable-punch (DP-SPS) or the high-pressure (HP-SPS) setup, as detailed in the experimental section. Densification conditions are listed in **Table 3.1** with samples labeled according to the stoichiometry (S or E for quasi-stoichiometric and Al-rich, respectively), processing parameters (D or H, for deformable-punch and high-pressure diamond/SiC setup, respectively), and rounded numbers for the measured grain size.

Sample	Grain Size (nm)	Sintering Conditions	Annealing Conditions	$HV_{40\ gf}$ (GPa)
S-D14	14.4	**780°C**/1.6 GPa/5 min	630°C/1 hr	17.0 (±0.3)
S-D15	14.7	**780°C**/1.6 GPa/5 min	630°C/1 hr	17.6 (±0.2)
S-D20	20.2	**820°C**/1.4 GPa/5 min	670°C/1 hr	18.8 (±0.2)
S-H12	12.7	**730°C**/2.2 GPa/NH	580°C/1 hr	17.5 (±0.7)
S-H14	14.9	**730°C**/2.2 GPa/4 min	580°C/1 hr	17.8 (±0.6)
S-H15	15.3	**780°C**/2.0 GPa/NH	630°C/1 hr	18.4 (±0.4)
S-H16	16.7	**800°C**/1.4 GPa/NH	650°C/1 hr	18.4 (±0.5)
S-H18	18.7	**780°C**/2.0 GPa/4 min	630°C/1 hr	18.5 (±0.2)
S-H21	21.4	**850°C**/1.4 GPa/NH	700°C/1 hr	18.6 (±0.1)
S-H26	26.4	**900°C**/1.4 GPa/NH	750°C/1 hr	18.6 (±0.3)
S-H34	34.1	**850°C**/1.4 GPa/4 min	700°C/1 hr	18.0 (±0.6)
S-H48	48.2	**950°C**/0.8 GPa/4 min	800°C/1 hr	17.7 (±0.6)
E-D17	16.9	**820°C**/1.4 GPa/5 min	670°C/1 hr	18.8 (±0.9)
E-H12	12.4	**780°C**/2.0 GPa/4 min	630°C/1 hr	19.1 (±0.4)
E-H13	12.6	**780°C**/2.0 GPa/4 min	630°C/1 hr	19.2 (±0.6)
E-H18	17.8	**820°C**/1.6 GPa/5 min	670°C/1 hr	18.7 (±0.4)

Table 3.1: Summary of sintered ZAO pellets including sintering conditions and final grain sizes. Samples were labeled according to the stoichiometry (S or E for quasi-stoichiometric and Al-rich, respectively), processing parameters (D or H, for deformable-punch and high-pressure, respectively), and rounded numbers for measured grain sizes. Hardness values were all measured at loads of 40 gf.

Also shown in **Figure 3.1** are XRD patterns for representative sintered pellets of each stoichiometry. Although patterns for only samples S-H16 and E-H13 are shown in the figure, all sintered pellets were tested and showed the spinel phase with absence of a second phase, at least to the technique detection limit. Peaks were sharper than those found for nanopowders, but still consistent with nanoscale dimensions. Despite multiple attempts, E-ZAO samples could not be densified to high transparency with grain sizes higher than 17.8 nm: traces of an Al-rich second

phase systematically nucleate during densification and compromise transparency. Similar limitations have been previously observed during the fabrication of doped nanoceramics[50]. For instance, 3-mol% La-doped magnesium aluminate could not be sintered to high densities at grain sizes above 61 nm using SPS[50]. This was attributed to second phase nucleation from excessive La segregation to the grain boundaries due to limited grain boundary area at large grain sizes. This may suggest that excess Al in dense E-ZAO samples is segregated to the grain boundary regions, which would be consistent with observations in Al-rich magnesium aluminate[97], but further studies are needed.

All pellets included in this study were visibly transparent for both S-ZAO and E-ZAO. The in-line transmission obtained for S-H21 showed approximately 76% of light transmission in the visible spectrum range (500-750 nm) which is consistent with data reported in literature for nanocrystalline[26] and microcrystalline[121] zinc aluminate. High levels of transmission may be attributed to a lack of porosity and high density in samples: pores are known to act as efficient light scattering centers in dense ceramics[14,17,122].

3.3.2: Hardness tests

Samples underwent Vickers indentation tests at a fixed load of 40 gf to limit spallation[13,33] as discussed in the experimental section. Hardness values are included in **Table 3.1** along with the corresponding grain sizes. The hardness data is also consolidated and plotted as a function of the inverse of the root square of the grain size in **Figure 3.3** along with data obtained by Fu et al. for sub-microscale zinc aluminate[18].

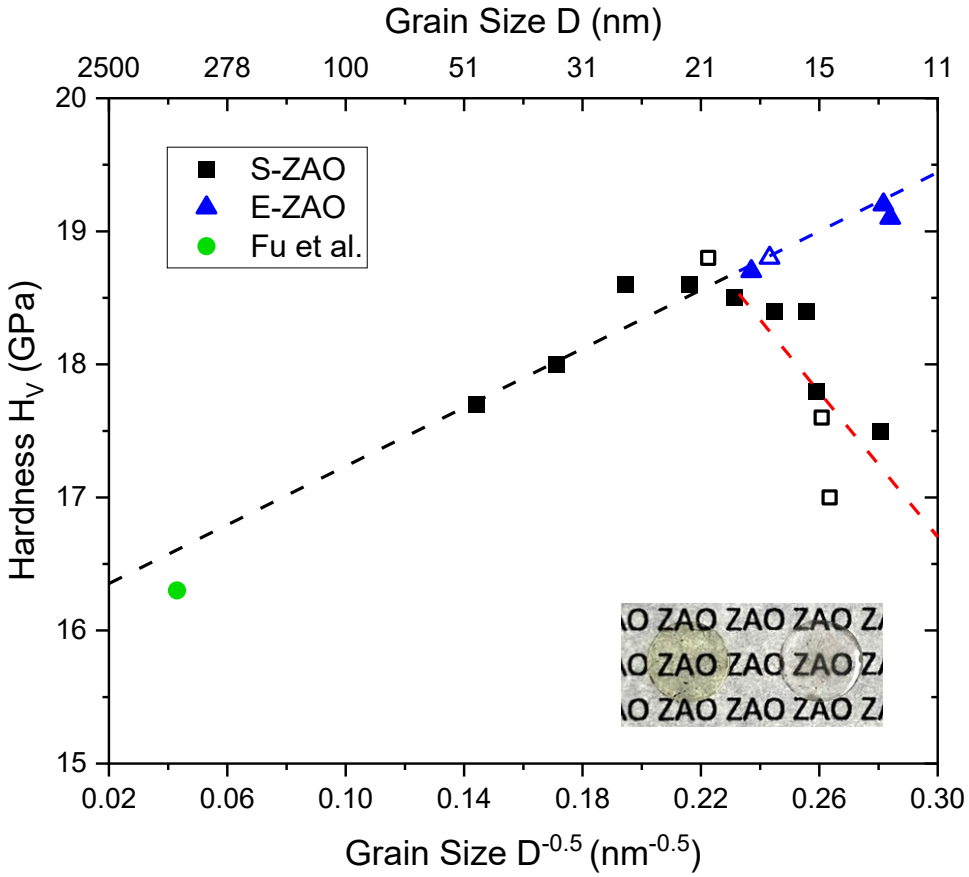

Figure 3.3: Vickers hardness plotted in Hall-Petch form for all S-ZAO (blue) and E-ZAO (red) samples along with data for sub-microscale zinc aluminate reported by Fu et al. Samples sintered by high pressure spark plasma sintering are denoted with a filled symbol while those sintered using deformable-punch spark plasma sintering are denoted by a hollow one. The inset image shows samples S-H21 (left) and E-H18 (right) both with 4 mm diameters.

Hardness for HP-SPS prepared S-ZAO increased with decreasing grain size down to about 24 nm where it reached 18.8 (±0.3) GPa. The number in parentheses represents a 95% confidence interval around the mean hardness, e.g., the true average hardness for this sample will lie between 18.5 and 19.1 GPa. The hardness is overall higher than what is reported in the literature for micron and submicron scale grains, which is consistent with grain size hardening. Softening is observed below 24 nm in these samples in typical inverse Hall-Petch fashion; the onset of this breakdown occurs at grain sizes similar to 10YSZ and magnesium aluminate[27,33,70]. The presence of a Hall-

Petch inversion in HP-SPS S-ZAO contradicts data from Yang et al. who reported hardening persists down to grain sizes as low as 10.1 nm[26].

The data for S-ZAO prepared by DP-SPS are also plotted in the graph and apparently follow the same trend of the HP-SPS processed ones. This is somewhat surprising considering recent claims that DP-SPS could be responsible for the postponement of the Hall-Petch relation to grain sizes below 10 nm[24,26]. On the other hand, E-ZAO processed with both DP-SPS and HP-SPS exhibited higher hardness values, particularly for smaller grain sizes, suggesting an apparent extension of the Hall-Petch relationship down to 12.6 nm. S-ZAO and E-ZAO hardness values were fairly consistent until the onset of the Hall-Petch breakdown in S-ZAO: the Hall-Petch slopes were 13.9 GPa·nm$^{0.5}$ and 9.4 GPa·nm$^{0.5}$ for S-ZAO and E-ZAO, respectively. Conversely, the slope for Yang et al.'s samples was reported as 23.9 GPa·nm$^{0.5}$, which is notably larger than the slopes from this study. Fully dense samples with grain sizes below 12.6 nm could not be attained. Yang et al. did not report the stoichiometry of their powders, but the present data suggests it is possible their samples were Al-rich and similar to E-ZAO. This would contradict the idea proposed by Koch and Narayan that an inverse Hall-Petch relation is only observed for defect-rich samples[105].

3.3.3: Indentation analysis

Indentations in ceramics are characterized by the formation of cracks underneath the indented region. The elastic deformation region formed during indentation is small. Although some deformation can occur in nanoceramics, particularly when nanoscale grains rotate and slide against each other[13,66,68,123], the total load accommodation from this mechanism is limited. Instead, sub-surface cracking becomes the prominent energy dissipation mechanism during Vickers hardness tests. Hence, indentations were cross-sectioned using focused ion beam (FIB) milling to reveal crack geometries beneath the surface to elucidate the differences in hardness trends for S-ZAO and E-ZAO, especially at small grain sizes. For proper comparison, secondary electron images were captured of cross-sectioned indentations from the quasi-stoichiometric at grain sizes before and after the Hall-Petch inversion for S-ZAO, and at a comparable small grain size for E-ZAO.

Figure 3.4 shows the aforementioned cross-sections where all samples present a network of sub-surface cracks which indicate load energy accommodation as in the quasi-plasticity model[24,26]. The density of cracks apparently reduces as the grain sizes increase in both S-ZAO and

E-ZAO, suggesting differences in the energy absorption mechanisms for large and small-grained samples, which is consistent with previous reports[26,33,70,124]. Long lateral cracks are present at small grain sizes in S-ZAO (S-H12 and S-H15). Similar lateral cracks are found, to a lesser extent, at large grain sizes in S-ZAO (S-H34 and S-H48). These types of cracks called lateral vents result from intense residual stresses introduced by material relaxation during the unloading stage of microindentation[125]. Yang et al. concluded that lateral vents are intergranular in zinc aluminate[26], which suggests that indentation stresses are relieved through fracturing of weak grain boundary networks in this case. E-ZAO samples with small grain sizes (E-H12) exhibit limited lateral vents, and a crack pattern more similar to that of S-H48. The second type of cracking mechanism found in these samples is the median vent which Lawn and Wilshaw define as stable cracks that form along the indenter plane during the loading cycle[125]. A median vent is clearly observed for S-H48 but is not found at smaller grain sizes in S-ZAO. Interestingly, median vents are persistent for E-ZAO across the studied grain sizes. For reference, indentation cross-sections obtained by Yang et al.[26] (who reported absence of the inverse Hall Petch relation) were added to the figure. Unlike the quasi-stoichiometric case, the shift in cracking pattern from large to small grain sizes is not as pronounced in E-ZAO.

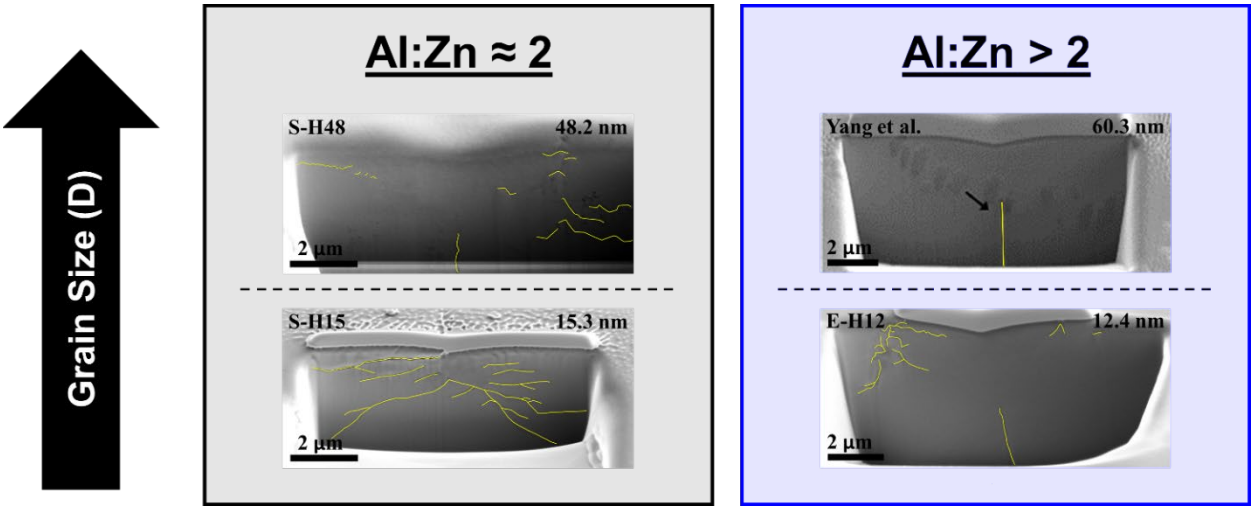

Figure 3.4: Secondary electron images of ion milled cross-sections under Vickers indentations for S-H15, S-H48, and E-H12. Also included is a $ZnAl_2O_4$ cross-sections imaged by Yang et al. Lateral vents exist in stoichiometric sample S-H15, and to a lesser extent in S-H48. On the other hand, Al-rich samples only exhibit lateral vents at small grain sizes. Median vents are present in all Al-rich samples, but only in the larger-grained stoichiometric samples (S-H48).

The collection of data suggests the Al excess is altering the fracture behavior, resulting in increased hardness. This could be explained by grain boundary stabilization, as reported by Hu et al. in metal alloys[110]. This concept has been brought up particularly in Ni-Mo alloys and shows that segregation of elements to grain boundaries can delay the inverse Hall-Petch relation by reducing their excess energies (local bond strengthening) and ability to slide via pinning. Although grain boundary sliding is reduced at room temperature in ceramics, excess Al could enhance grain boundary toughness thus reducing lateral vents and postponing the Hall-Petch breakdown.

3.4: Discussion

This study provides evidence that an Al excess in zinc aluminate is responsible for postponing the onset of the Hall-Petch inversion to smaller grain sizes, and even suggests that prior work in which the inverse Hall-Petch is not observed may be explained by this concept[24,26,34]. Because lateral vents result from intense residual stresses caused by unloading the indenter[107], their presence in quasi-stoichiometric zinc aluminate provides some insight into the behavior of the plastic zone of deformation during indentation. This would imply that Al-rich samples can better

accommodate these residual stresses. A possible explanation for this is the localization of the excess Al similar to ionic dopants which can pin the movement of grain boundaries in grain growth experiments at elevated temperatures, either by kinetics or thermodynamics[50–53,63]. Chiang and Kingery have shown that excess Al can impact the coarsening behavior of non-stoichiometric magnesium aluminate by modifying grain boundary chemistries[95,96]. The change in load accommodation at room temperature observed here is somehow equivalent to recent works on dopant-engineered grain boundaries in metals[59,60,126] and ceramics[64]. In ceramics, La-doped YSZ shows increased toughness[64].

Hardening by Al enrichment is also evident by the degree of spallation or chipping occurring during the Vickers indentation tests in samples of both stoichiometries. As mentioned, all samples were indented with a relatively small load (40 gf) in this study to limit spallation in quasi-stoichiometric zinc aluminate. Spallation was not present to the same extent in Al-rich samples from this study, and was not reported in the study performed by Yang et al.[26] It is known that spallation or chipping directly results from lateral vents underneath indentations[13,107,125], so the spallation in quasi-stoichiometric samples is consistent with the sub-surface crack patterns.

The hypothesis that an Al excess is affecting grain boundary load accommodation capacity is aligned with a recent study by Ratzker et al. on the plastic deformation mechanisms in nanocrystalline magnesium aluminate undergoing Vickers hardness testing[13]. Ratzker et al. found evidence that indenter strain in nanocrystalline magnesium aluminate is accommodated by a combination of dislocation motion and grain boundary plasticity (e.g., rotation and sliding)[13]. This agrees with the model developed by Sheinerman et al.[124] for grain size hardening in nanocrystalline ceramics which claims that grain boundary sliding activation energy dictates the onset of the inverse Hall-Petch relation. The yield strength for deformation by grain boundary sliding is defined here as:

$$\sigma_{GBS} = \frac{M}{b^3}\left(\frac{\Delta F}{N_A} + k_B T ln \frac{\dot{\gamma} D}{3 b v_D}\right) \qquad \textbf{(3.2)}$$

where ΔF is the activation energy for grain boundary sliding, v_D is the Debye frequency, b is the interatomic distance, N_A is Avogadro's number, k_B is Boltzmann's constant, $\dot{\gamma}$ is the shear strain rate, and D is the grain size. Dislocation slip is described by the traditional Hall-Petch relationship in **Equation 3.1**. This model predicts that a Hall-Petch inversion begins when most grains in the system deform by grain boundary sliding instead of dislocation slip; hence, the parameter ΔF is key to determining a material's grain size hardening behavior. We applied this model to the zinc

aluminate data from this study assuming values of $\dot{\gamma} = 10^{-3}$ s^{-1} and $b = 0.286$ nm[109,124]. To better illustrate the extended Hall-Petch relationship in E-ZAO, S-ZAO samples before the Hall-Petch inversion were combined with E-ZAO to estimate the Hall-Petch parameters ($\sigma_0 = 16.3$ GPa, $k = 10.6$ GPa·$nm^{0.5}$) for the fit as shown in **Figure 3.5**.

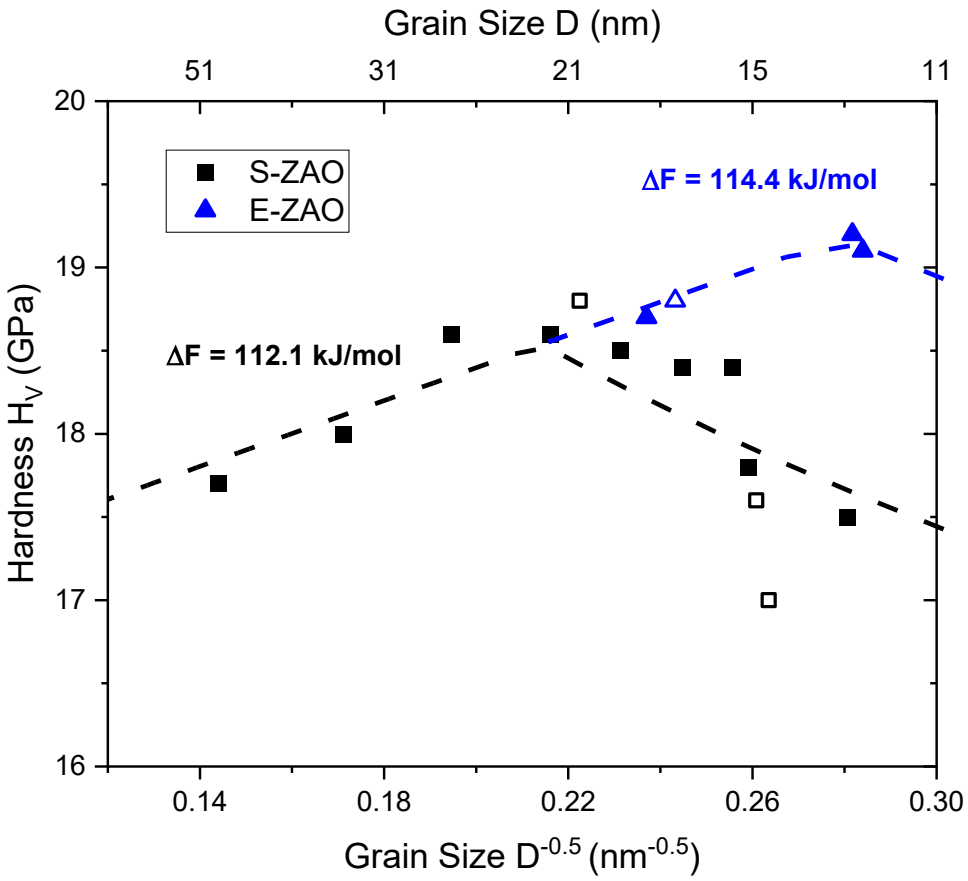

Figure 3.5: Vickers hardness plotted in Hall-Petch form for all S-ZAO (black) and E-ZAO (blue) samples along with their fits (dashed lines) according to the Sheinerman et al. model. Samples sintered using deformable-punch spark plasma sintering are denoted in hollow symbols. The model estimates a grain boundary sliding activation energy of 112.1 and 114.4 kJ/mol for S-ZAO and E-ZAO, respectively.

According to the model, S-ZAO exhibits a Hall-Petch breakdown at a grain size of 21.8 nm with a maximum hardness of 18.6 GPa while E-ZAO does not show an inversion until a grain size of 12.8 nm. The activation energies for grain boundary sliding are 112.1 and 114.4 kJ/mol for

S-ZAO and E-ZAO, respectively. The fit agrees well with our experimental data and suggests that Al excess increases ΔF by 2.3 kJ/mol ultimately leading to an extension of the Hall-Petch relationship to smaller grain sizes in E-ZAO. Using the same model to fit data from Yang et al. for zinc aluminate, an activation energy of 120.2 kJ/mol was achieved. This is consistent with the significantly extended Hall-Petch relation observed by Yang et al. and supports the idea that the sample was likely rich in Al.

Although some limited grain boundary sliding and rotation has been experimentally observed in nanoceramics[13,66], grain boundary shearing and fracture are likely more relevant load accommodation mechanisms in nanoceramics[26,33,70], as described by the quasi-plasticity model. Sheinerman et al.'s derivation of **Equation 3.2** does not disqualify the interpretation of ΔF (named activation energy for grain boundary sliding) as being the activation energy for grain boundary "shearing" or even "fracture initiation". This interpretation would make more physical sense without compromising the model itself. The crack patterns observed underneath indentations provide further evidence for grain boundary shearing and fracture as the cause of the Hall-Petch inversion in zinc aluminate.

Figure 3.6 juxtaposes the models fitted using the Sheinerman et al. study with the sub-surface crack patterns observed with SEM. This figure highlights the idea that the postponed Hall-Petch inversion in E-ZAO stems from the distinct shift in crack pattern: small-grained E-ZAO samples crack more similar to large-grained S-ZAO (mode II) than small-grained E-ZAO (mode III). The decrease in lateral vents in E-ZAO suggests that excess Al is effective in strengthening zinc aluminate grain boundaries to prevent shear and fracture which is manifested macroscopically as increased hardness.

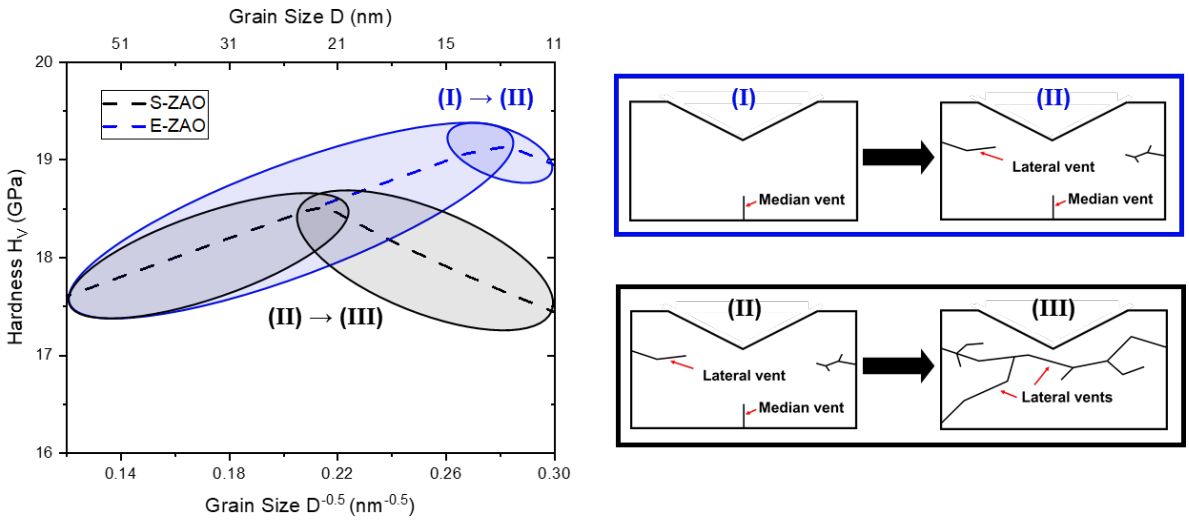

Figure 3.6: (I) Indentation cross-section exhibiting only a median vent found only in E-ZAO (II) cracking pattern featuring limited lateral vents, and a median vent which was found in large-grained S-ZAO and small-grained E-ZAO, and (III) pattern observed in small-grained S-ZAO with lateral vents extending through the entirety of the cross-section. S-ZAO transitions from mode (II) cracking to mode (III) with decreasing grain size while E-ZAO instead moves from mode (I) to mode (II).

The positive results in improving hardness by Al enrichment in zinc aluminate could provide a better alternative to the recent usage of rare-earths as dopants to improve the mechanics of nanoceramics[64]. In addition to the cost associated with the addition of rare-earth elements to the system, a further complication with rare-earth doping in spinel materials is the propensity for the rare-earth oxide to form a second phase as reported by Hasan et al. in magnesium aluminate[50]. The spinel structure is known for its ability to accommodate significant deviations from stoichiometry: single phases have been reported in magnesium aluminate for deviations as large as 1.84:1 and 3.00:1 Al:Mg, or $MgAl_{1.84}O_4$ and $MgAl_{3.0}O_4$ respectively[102]. Zinc aluminate has exhibited a similar ability to incorporate excess Al in the lattice without second phase formation: Areán et al. synthesized single-phase bulk ceramics at Al:Zn ratios of 2:1, 4:1, and 8:1 ($ZnAl_{4.00}O_4$, $ZnAl_{8.00}O_4$, and $ZnAl_{16.00}O_4$)[127]. Yang et al. show this is also possible in nanocrystalline zinc aluminate by synthesizing $ZnAl_{2.40}O_4$ [118], opening a great perspective for further studies.

3.5: Conclusions

The present work serves as evidence that Al excess can extend the normal Hall-Petch relationship to smaller grain sizes in zinc aluminate spinel. While the inverse Hall-Petch relation was observed at a grain size of 21.4 nm for quasi-stoichiometric zinc aluminate, Al-rich samples exhibited improved hardening to a grain size of 12.6 nm as demonstrated by Vickers hardness tests. Analysis of sub-surface cracking showed that Al enrichment altered the cracking patterns formed beneath Vickers indentations, representing a change in the total load accommodation; this is reflected by an increase in hardness in Al-rich zinc aluminate. The data indicates that grain boundaries are likely enriched with Al which improves grain boundary toughness by serving as a pinning agent for grain shearing, similar to reports for rare-earth doping. Data fitting suggests an increase in the activation energy for grain boundary shearing/fracturing, but further studies and superior models are required to confirm this. Altogether, the data demonstrates the composition of zinc aluminate spinel is critical for understanding the grain size dependence of its mechanical properties. Moreover, by contrasting DP-SPS and HP-SPS, we provide evidence that sintering technique has an insubstantial effect on the Hall-Petch inversion in nanocrystalline oxides.

Chapter 4: Y^{3+} Surface Segregation Promotes Coarsening Inhibition in Nanocrystalline Zinc Aluminate

Abstract

The thermal stability of zinc aluminate nanoparticles is critical for their application as catalyst supports. In this study, the stability of zinc aluminate nanoparticles was improved upon doping with 0.5 mol% Y_2O_3. The dopant was observed to segregate to 3the nanoparticle surfaces and effectively reduce excess energies while hindering coarsening. Atomistic simulations on a 4 nm zinc aluminate nanoparticle provided the segregation potential of four dopants with varying ionic radii (Sc^{3+}, In^{3+}, Y^{3+}, and Nd^{3+}). Segregation energies were generally proportional to ionic radii, with Y^{3+} showing the highest potential for surfaces segregation. Direct measurements of surface thermodynamics indicated a decrease in average surface energy for doped zinc aluminate from 0.99 (undoped) to 0.85 J/m^2 (doped). Further, diffusion coefficients calculated from the coarsening curves for both compositions at 850°C were 4.8×10^{-12} (undoped) and 2.5×10^{-12} cm^2/s (doped) indicating coarsening inhibition results from a combination of a reduced driving force (surface energy reduction) and decreased atomic mobility.

4.1: Introduction

Zinc aluminate ($ZnAl_2O_4$) spinel is an excellent material to facilitate the catalysis of toluene degradation[128,129], hydroformylation[130,131], and hydrogenation[130,132,133] due to its characteristically wide bandgap and high chemical and thermal stabililty[130,134,135]. In the form of nanocrystals, if the support itself is the catalyst, the high specific surface area increases catalytic activity as the number of active sites directly scales with the available surface area. If zinc aluminate nanocrystals act as a support instead, the associated high surface areas are also beneficial as they assist in uniformly dispersing active metals.

However, the excess energies associated with the inherently high surface areas of nanocrystals give rise to processing challenges and limitations concerning operating temperatures. High surface energies lead to reduced activation energies for coarsening at the nanoscale[136], enabling grain growth at lower temperatures. Kinetic approaches have often been used to limit coarsening in the nanocrystalline regime[137], but surface thermodynamics also play a significant role in dictating the coarsening process[47,138]. Similar to other metal oxides, zinc aluminate

nanoparticles grow via Ostwald ripening[139], where small particles evaporate/precipitate or diffuse onto larger ones to reduce the surface energy of the system by mean grain enlargement[140–142]. This growth mechanism is identified by its cube-root dependence on time, as shown in **Equation 4.1**:

$$R_t^3 - R_0^3 = Kt \qquad \textbf{(4.1)}$$

where R_t is the mean particle radius at a given time t, R_0 is the mean radius at the onset of growth, and K is a rate constant that is directly proportional to the average particle surface energy and governing diffusion coefficient[101]. For systems that undergo Ostwald ripening, this relationship highlights the significance of surface energies on hindering coarsening, which becomes increasingly relevant at the nanoscale due to the substantial rise in surface area[141].

Krill et al. derived a model describing the systematic reduction of interfacial energies from dopant segregation based on the Gibbs adsorption isotherm, which can potentially be applied to improve thermodynamic stability at the nanoscale[92,143]. The model describes the relationship between interfacial energy and number of segregated species as shown in **Equation 4.2**:

$$\gamma_s = \gamma_{s0} - \Gamma_B(RTlnX_B - \Delta H_{seg}) \qquad \textbf{(4.2)}$$

where γ_s is the surface energy of the doped material, γ_{s0} represents the surface energy of the undoped material, Γ_B is the solute excess at the interface, X_B is the concentration of the dopant, and ΔH_{seg} is the enthalpy of segregation of the dopant to the surface[85]. The relationship highlights the idea that dopants with spontaneous segregation enthalpies reduce the surface energy, hence decreasing the driving force for coarsening.

Exploiting this concept, Hasan et al. observed limited grain growth in rare-earth doped magnesium aluminate, a material isostructural with zinc aluminate. After calcination at 1000°C, the specific surface area for La-doped magnesium aluminate remained ~50% larger than that of the undoped sample[104]. Surface energy measurements revealed a reduction of ~0.3 J/m^2 in the doped samples, attributed to the ion surface segregation. Similar studies have not been performed on zinc aluminate, but Yang et al. did show evidence of grain growth inhibition in Al-rich zinc aluminate nanoparticles as compared to the stoichiometric system[118]. Since excess Al has commonly been found to accumulate at spinel interfaces[95–97], the shift in zinc aluminate growth kinetics suggests dopant segregation may induce a similar effect.

In this work, we study the effect of four different dopants [Sc^{3+} (74.5 pm), In^{3+} (80.0 pm), Y^{3+} (90.0 pm), and Nd^{3+} (98.3 pm)] on the surface thermodynamics and stability of zinc aluminate nanoparticles. All dopants are isovalent with Al^{3+} but span a range of ionic radii to systematically assess the effects of the elastic strain energies (due to the size mismatch with Al^{3+}) on the surface energetics. Atomistic simulations on a 4 nm nanoparticle computed a realistic particulate system and consistently showed the preferential Y^{3+} segregation to surfaces when substituting for Al^{3+} ions.

Experimental data on surface energies measured by water adsorption microcalorimetry confirmed the trends from simulations, demonstrating reduced surface energies caused by Y-doping. Coarsening studies further demonstrated the improved stability of Y-doped zinc aluminate, with the nanoparticles exhibiting reduced grain growth compared to their undoped counterparts. Fitting the data with the Ostwald ripening model led to an enriched understanding of the interdependence between thermodynamic and kinetic effects of the doping.

The results imply that nanoparticle morphology can be tailored by introducing a solute excess at the surface and indicate atomistic simulations can have a significant role in the design of stable nano-catalysts.

4.2: Methods and Experimental Procedures

4.2.1: Atomistic simulations on a 4 nm nanoparticle

The relative segregation potentials of four dopants (Sc^{3+}, In^{3+}, Y^{3+}, Nd^{3+}) to zinc aluminate surfaces were investigated using molecular dynamics simulations on a 4 nm (3427 atom) nanoparticle. The particle was built by adjusting a replicated zinc aluminate unit cell while maintaining a net zero charge across the particle. Visualization of the structure was done in OVITO[144], while all calculations were performed with LAMMPS[145] using Buckingham pair potentials to estimate short-range interactions as represented by **Equation 4.3**:

$$E = Ae^{-r/\rho} - \frac{C}{r^6} \qquad \textbf{(4.3)}$$

where A, ρ, and C are coefficients unique to each atom pair, E is the potential energy between a pair of atoms, and r is the interatomic distance[146]. Buckingham coefficients for all atom pairs used in this study are included in **Table 4.1** below:

Atom Pair	A (eV)	ρ (Å)	C (eVÅ^6)	Reference
O^{2-}—O^{2-}	9548.0	0.2192	32.0	Grimes et al.[147]
O^{2-}—Zn^{2+}	529.7	0.3581	0	Grimes et al.[147]
O^{2-}—Al^{3+}	1725.2	0.2897	0	Grimes et al.[147]
O^{2-}—In^{3+}	1495.7	0.3327	4.3	Grimes et al.[147]
O^{2-}—Y^{3+}	1766.4	0.3385	19.4	Grimes et al.[147]
O^{2-}—Sc^{3+}	1575.9	0.3211	0	Busker et al.[148]
O^{2-}—Nd^{3+}	3300.1	0.2868	0	Migliorati et al.[149]

Table 4.1: Buckingham pair potentials used for each cation-oxygen (derived by Grimes et al.[147], Busker et al.[148], and Migliorati et al.) pair in the study. All other interactions were taken to be zero, as assumed by Hasan et al. in previous work on magnesium aluminate[50].

The resultant nanoparticle was annealed at 1273 K for 4 ns followed by slow quenching to approximately 0 K. After minimizing the quenched structure, its surface energy was calculated as the difference between the potential energy of the nanoparticle and the potential energy of a bulk structure with the same number of atoms as in **Equation 4.4**.

$$\gamma_{s0,MD} = \frac{1}{A}(E_{NP} - E_{bulk}) \qquad \textbf{(4.4)}$$

Here $\gamma_{s0,MD}$ is the surface energy of the undoped 4 nm nanoparticle, A is the surface area of the nanoparticle, and E_{NP} and E_{bulk} are the potential energies of the nanoparticle and bulk structure with the same number of atoms[50].

A methodology similar to that proposed by Hasan et al. was used to determine the segregation potential for each dopant in this system. The method operates under the assumption that the lowest energy defect involves trivalent dopants substituting for Al^{3+} atoms[50]. Therefore, a series of dopant substitutions was performed on the nanoparticle where one dopant atom is substituted into every Al^{3+} site followed by an energy minimization[50]. Segregation energies were estimated for each surface site in the nanoparticle by taking the difference in potential energy between a substitution in the bulk and the substitution at every surface site (defined as 1 Å in thickness from the vacuum). The average of the surface segregation energies was taken to represent the surface segregation energy (E_{seg}) of each dopant in the zinc aluminate nanoparticle since the

experimental system involves dopant concentrations beyond the dilute limit: 10-25% of trivalent surface sites will be occupied by Y^{3+} depending on the particle size.

Surface energies were then calculated for 4 nm zinc aluminate nanoparticles doped in quantities equivalent to experimental systems using **Equation 4.5**:

$$\gamma_{s,MD} = \gamma_{s0,MD} - (\frac{n}{A})E_{seg} \qquad \textbf{(4.5)}$$

where $\gamma_{s,MD}$ is the surface energy of the doped nanoparticle, n is the number of dopants in the system (approximately 0.5 mol% Y_2O_3) A is the surface area of the nanoparticle, and E_{seg} is the segregation energy of each dopant. Surface energies calculated from simulations cannot be directly compared due to experimentally measured values due to the complex defect chemistry not considered here (e.g., spinel site inversion, kinetically driven self-segregation within the particle originating from the space charge layer, local dipole effects of Y_2O_3 complexes, etc.). Nonetheless, the trends in segregation energies provide useful information on the relative stabilities of the four dopants in zinc aluminate.

4.2.2: Synthesis and nanopowder characterization

Y-doped (YZAO) and undoped (ZAO) zinc aluminate nanoparticles were synthesized via a modified co-precipitation route[26,118,150,151]. Prior to synthesis, water contents were measured for each nitrate precursor to ensure stoichiometric ratios were maintained. $Zn(NO_3)_2 \cdot 6H_2O$ and $Al(NO_3)_3 \cdot 9H_2O$ (Sigma Aldrich, >98%) were dissolved in deionized water in the metal stoichiometric molar ratio of 1:2. Hydroxides were precipitated using a 2 mol/L aqueous ammonia solution under a constant pH of 8.75 to inhibit the formation of $Zn(NH_3)_4^{2+}$: precipitation of this complex limits the number of Zn^{2+} ions in the solution leading to an Al-rich environment[26,118,150,151]. Precipitates were washed three times with ethanol and dried in an oven at 80°C for 48 hours. In the case of Y-doped zinc aluminate (YZAO), $Y(NO_3)_3 \cdot 6H_2O$ (Sigma Aldrich, >98%) was also dissolved in the nitrate precursor solution to give 0.5 mol% Y_2O_3. Upon drying, the hydroxide precipitates were ground into fine powders and calcined in a Thermo Scientific Lindberg/Blue M (Thermo Fisher Scientific Inc., Waltham, MA) box furnace at 550°C for 4 hours. Calcination temperatures were chosen to ensure complete crystallization while limiting grain growth[26,118,152].

Phase analysis and crystallite size measurements were performed on both sets of powders using x-ray diffraction (XRD) on a Bruker D8 (Bruker, Billerica, MA) operated at 40 kV, 40 mA (CuKα radiation, λ=1.5406 Å). The crystallite size estimation tool in the Match! (Crystal Impact, Bonn, Germany) software along with reference pattern #96-900-7021 (Levy et al.[153]) were used to measure crystallite sizes for all x-ray analysis in this work.

As-synthesized powders were imaged using scanning transmission electron microscopy (STEM) on a JEOL-ARM300F Grand ARM (JEOL, Peabody, MA) to validate crystallite size measurements from XRD. Elemental mapping was performed on coarsened YZAO nanoparticles (900°C, 1 hour) using electron energy loss spectroscopy (EELS) to confirm Y^{3+} segregation to surfaces.

ZAO and YZAO powders were also analyzed by electron microprobe analysis (EMPA) with a Cameca SX-100 (Cameca, Gennevulliers, France) to compare Al:Zn ratios. Scans were taken at 10 different points on each sample and averaged to give Al:Zn ratios of 2.16 (±0.14) and 2.11 (±0.06) for ZAO and YZAO, respectively. These results confirmed that cationic ratios of both powders were within error of one another.

It has been well-documented that materials rich in Zn readily form carbonate species with CO_2 and moisture in air[154,155]. Such species could potentially impact nanoparticle coarsening behaviors (e.g., by pinning interfaces), so Fourier transform infrared spectroscopy (FTIR) was performed using a Bruker Tensor 27 (Bruker, Billerica, MA) to screen particles for Zn-rich carbonates prior to coarsening. Samples were compared to a reference pattern for zinc carbonate.

4.2.3: Coarsening experiments

Before subjecting powders to coarsening experiments, each powder was cleaned in a box furnace (700°C, 4 hours, O_2 environment) to remove residual carbonate species which could potentially affect the results. All coarsening experiments were performed within 12 hours of cleaning with powders being stored in a desiccator to prevent readsorption of carbonate species.

Powders were coarsened at two temperatures, 850°C and 950°C, in a Lindberg/Blue M (Thermo Fisher Scientific Inc., Waltham, MA) tube furnace for 0.5 min, 1 min, 5 min, 15, min 30 min, 60 min, 120 min, and 240 min to study the effects of Y-doping on zinc aluminate's Ostwald ripening behavior. Limited grain growth was observed due to the moderate temperatures, so all

grain sizes in this study were able to be measured using XRD and microstructures confirmed with electron microscopy.

4.2.4: Surface energy measurements

Surface stability was evaluated for ZAO and YZAO nanoparticles (cleaned at 700°C for 4 hours under O_2) by comparing surface energies measured by water adsorption microcalorimetry[98,156–159]. This technique is comprised of a water vapor dosing system (3Flex, Micromeritics Instrument Corp., Norcross GA) attached to a differential scanning calorimeter (Sensys Evo, Setaram Inc., France). After degassing at 400°C for 16 hours and a subsequent series of three O_2 and vacuum cycles to ensure particle surfaces are rid of any adsorbed carbonate species, samples are dosed in the 3Flex with controlled amounts of water vapor (one μmol) until surfaces are fully saturated with water. While this is happening, the calorimeter records a series of peaks associated with water adsorption occurring with each individual dose; when taken together with the adsorption isotherm from the 3Flex, surface energies can be calculated using thermodynamic models developed by Castro and Quach[158].

In this study, approximately 20 mg of ZAO and YZAO powders (previously degassed at 700°C for 4 hours under an O_2 environment in addition to the degassing described above) were analyzed by water adsorption microcalorimetry to calculate average surface energies.

4.3: Results and Discussion

4.3.1: Dopant selection using simulations

Molecular dynamics (MD) simulations were used to compare the surface segregation potentials of four candidate dopants (Sc^{3+}, In^{3+}, Y^{3+}, and Nd^{3+}) in zinc aluminate. A 4 nm nanoparticle of undoped zinc aluminate was initially built and annealed at 1273 K for 4 ns where it developed specific facets as highlighted in **Figure 4.1**. The predominant surfaces were (100) and (111), which was expected since those have previously been identified as the lowest energy surfaces in other spinel oxides[160–162].

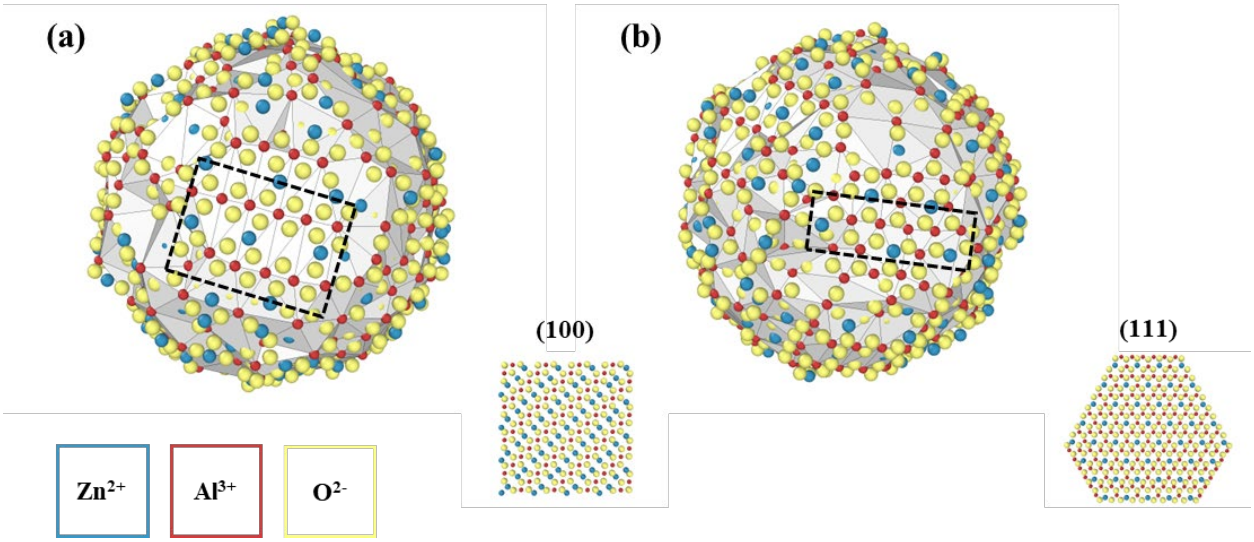

Figure 4.1: Different angles of the 4 nm zinc aluminate nanoparticle with Zn^{2+}, Al^{3+}, and O^{2-} represented in blue, red, and yellow, respecitvely. Dashed lines highlight (a) (100) and (b) (111) surfaces that developed from annealing at 1273 K for 4 ns. Inset images show reference structures of each of the planes. A surface mesh generated in OVITO[144] is overlaid on the nanoparticle.

The nanoparticle in **Figure 4.1** was then used as the starting point for simulations concerning dopant segregation. Al^{3+} ions were replaced by dopants one at a time starting from the center of the particle and the energy was minimized after each replacement step. **Figure 4.2** summarizes the results where all four dopants were found to have positive segregation energies between 0.3-3 eV per dopant atom. These energies are comparable to those calculated by Hasan et al. for magnesium aluminate using two planar surfaces[50]. The positive segregation energies indicate zinc aluminate nanoparticles are in a lower energy state when dopants substitute at surface sites as opposed to the bulk, predicting that during synthesis, these dopants would likely undergo surface segregation. Y^{3+} had the highest segregation energy of all dopants considered at 2.78 eV with a corresponding surface energy (assuming 0.5 mol% Y_2O_3) of 1.50 J/m^2, about 0.04 J/m^2 lower than that of the undoped nanoparticle.

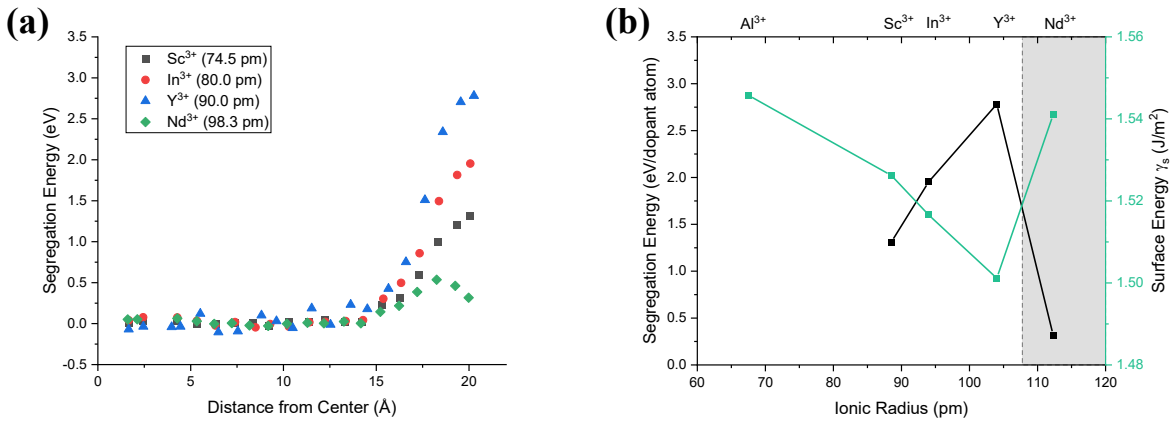

Figure 4.2: (a) Segregation energies for Sc^{3+}, In^{3+}, Y^{3+}, and Nd^{3+} in zinc aluminate calculated using molecular dynamics simulations on a 4 nm nanoparticle. Energies are binned by distance from the center the particle. (b) Segregation (squares) and surface (circles) energies plotted against ionic radii for each dopant as well as Al^{3+} for the undoped case. A Y_2O_3 concentration of 0.5 mol%, was used to estimate surface energies. Surface energies decrease as dopant ionic radius increases with a breakdown in this trend (area shaded in grey) as ionic radii approach that of Nd^{3+}.

In general, the decrease in surface energies is attributed to dopants satisfying bonds within the surface region due to their relatively large ionic radii. This ionic size mismatch is also responsible for the segregation itself, since larger ions would show elevated elastic strain in the lattice[50]. Unlike previous studies[50], the proportionality between the segregation energy and the ionic radius broke down for the largest studied ion, Nd^{3+}, which showed the lowest segregation energy. No such breakdown has been reported in computational or experimental studies on interfacial segregation of dopants prior to this. The limited surface segregation for Nd^{3+} compared to Y^{3+} can be explained by comparing the nearest neighbors for both dopants in the bulk. Y^{3+} and Nd^{3+} have the same coordination in the bulk where both are surrounded by six O^{2-} nearest neighbors, however, the nearest neighbors are ~0.1 Å closer to Nd^{3+} atoms than Y^{3+} atoms. This decrease in nearest neighbor distance for Nd^{3+} leads to enhanced stability in the bulk compared to Y^{3+} which limits surface segregation. This change in nearest neighbor distance is likely due to the complex unique *f* orbital behavior found in Nd^{3+} which reportedly leads to a seven-fold coordination in neodymium oxide[163].

The molecular dynamics studies also provide key insight into the local environments that support the excess elastic strain caused by doping zinc aluminate with Y^{3+}. **Figure 4.3** shows two angles of the 4 nm zinc aluminate nanoparticle with a surface mesh color coded to represent the segregation energy of Y^{3+} the nearest trivalent sites. **Figure 4.3a** denotes a (100) facet that developed during the annealing and quenching process; the red coloring that spans the entire facet indicates low segregation energies (1-1.8 eV) of Y^{3+}. In fact, low segregation energies for highly ordered sites are found throughout the particle: **Figure 4.3b** shows another (100) facet where trivalent sites show low energies (e.g., site (ii)).

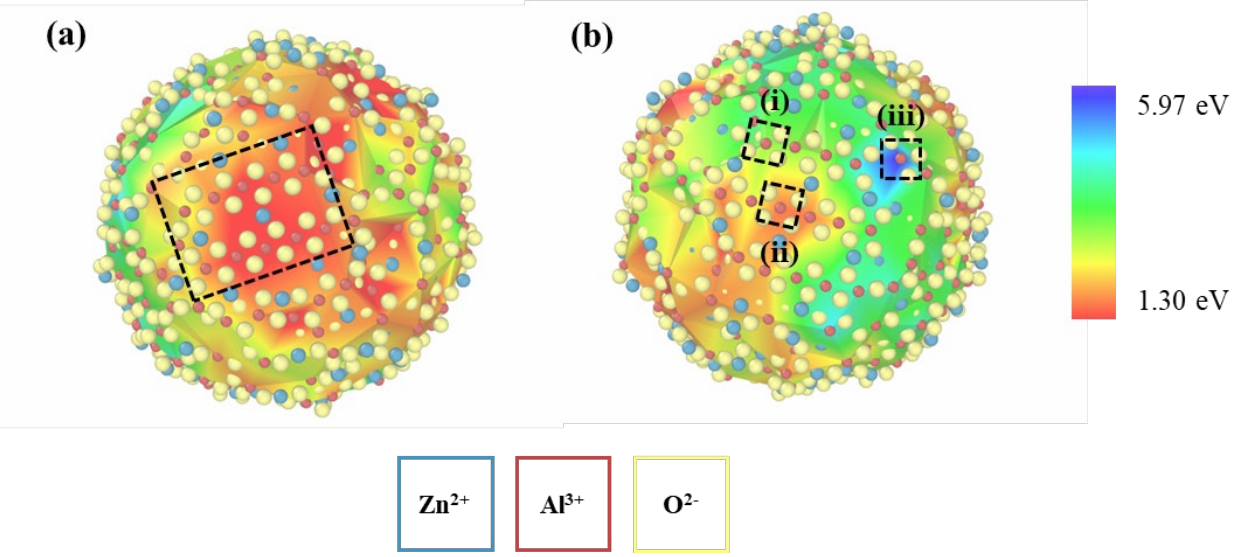

Figure 4.3: Two angles of the 4 nm zinc aluminate particle with a color gradient representing the segregation energies of Y^{3+} to trivalent surface sites. (a) Depicts a dashed (100) surface plane with relatively high segregation energies while (b) shows three Al^{3+} sites with distinct energies: (i) 3.02 eV, (ii) 1.61 eV, and (iii) 5.97 eV where sites (i) and (ii) lie in a (100) facet.

Upon further examination of the facet in **Figure 4.3b**, we find a higher spread of energies in this facet. Sites (i) and (ii) are near the same facet and are surrounded by similar local environments but have segregation energies of 3.02 eV and 1.61 eV, respectively. This energy difference between similar sites highlights the role of nearest neighbor coordination on dopant segregation energies: the O^{2-} atoms neighboring site (ii) are highly coordinated relative to those in site (i) due to being near the center of a facet, thus causing more elastic strain on Y^{3+}. This is even more apparent in site (iii) which has a lower coordination than the other two sites (only three O^{2-} atoms on the surface) which results in a segregation energy of 5.97 eV.

This relationship between segregation energies and relative positions of sites on the surface (e.g., proximity to facets and nearest neighbor coordination) predicts that Y^{3+} will preferentially segregate to sites with lower coordination. This idea has been proposed in literature[64] and is consistent with the fact that nanoparticles show higher energies at edges and corners as demonstrated by Hummer et al. for titanium oxide[164]. These effects tend to decrease at particle sizes larger than ~7 nm. This suggests that the segregation trends predicted by molecular dynamics here may break down as facets develop in zinc aluminate nanoparticles, i.e., as grains enlarge and edge contributions to surfaces are minimized. Larger particles are however challenging to simulate and beyond the scope of this work.

4.3.2: Synthesis and coarsening study

Based on the segregation behaviors in atomistic simulations, Y^{3+} was identified as the most likely dopant to segregate in zinc aluminate and selected for the subsequent experimental work. X-ray diffraction patterns (**Figure 4.4**) of undoped (ZAO) and Y-doped (YZAO) zinc aluminate nanoparticles synthesized by co-precipitation and calcined at 550°C revealed both sets of powders consisted of a single spinel phase with crystallite sizes of 5.9 nm and 6.5 nm, respectively. These results were consistent with TEM images of both sets of nanoparticles also shown in **Figure 4.4**.

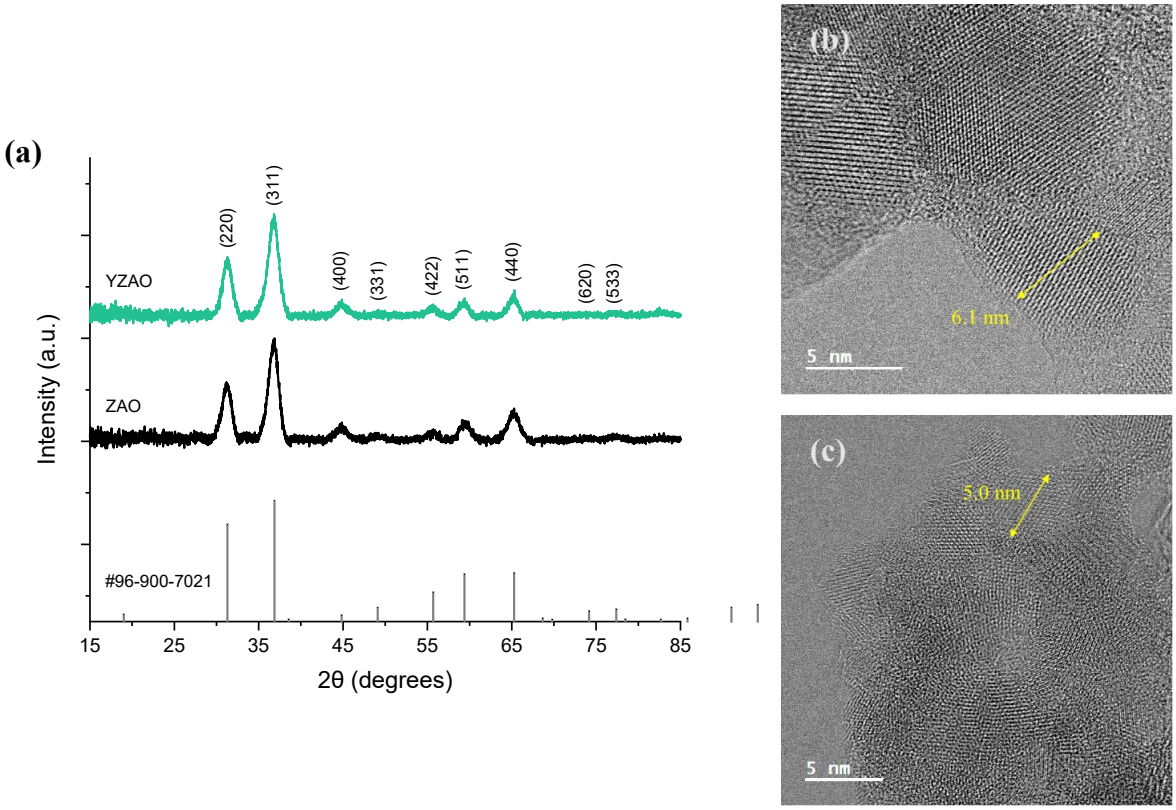

Figure 4.4: (a) X-ray diffraction patterns of ZAO (black) and YZAO (green) nanoparticles calcined at 550°C for 4 hours along with reference pattern #96-900-7021 from Levy et al.[153], (b) bright field transmission electron microscopy (TEM) images taken of ZAO nanoparticles, and (c) YZAO nanoparticles. XRD peaks and TEM images both confirm particles exhibit a single spinel phase along with uniform crystallite sizes in the nanoscale.

Since zinc and yttrium are likely to form stable carbonate structures, both doped and undoped nanoparticles were screened for carbonate species using FTIR prior to the coarsening studies. ZAO and YZAO prepared at 550°C and 700°C (under O_2) for 4 hours were compared to a zinc carbonate standard. **Figure 4.5** shows that both ZAO and YZAO contain zinc carbonate peaks around 1480 and 135 cm^{-1} when calcined at 550°C. The broad peak around 1630-1650 cm^{-1} in both patterns is attributed to the vibration of adsorbed water[165]. Each of the three peaks are absent in ZAO cleaned at 700°C, confirming these conditions are appropriate for removing zinc carbonates in zinc aluminate. Although YZAO cleaned at 700°C did show two broad peaks at lower wavenumbers, the shift in peak positions indicates these carbonates are more weakly bound compared to those in the 550°C sample and of a different nature, i.e., likely readsorbed from

atmospheric CO_2 during the transferring of the samples from the furnace to the FTIR[166]. Because they are loosely bound, such carbonates should have a negligible effect on coarsening and water adsorption studies as we assume the exposure to elevated temperatures (850°C and 900°C in coarsening experiments and degassing at 400°C for 16 hours) for even short times should effectively remove these species.

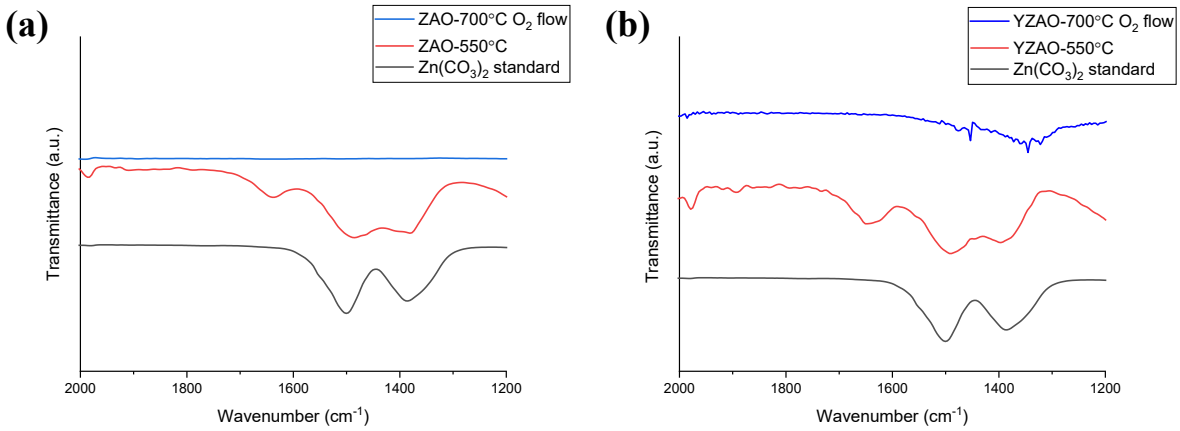

Figure 4.5: FTIR scans of (a) ZAO calcined at 550°C for 4 hours, ZAO cleaned at 700°C under O_2 flow for 4 hours, and a zinc carbonate standard along with (b) YZAO prepared at the same two conditions. Zinc carbonate shows two characteristic peaks around wavenumbers 1481 and 1385 cm^{-1} which are also present in ZAO and YZAO calcined at 550°C. A broader peak from 1630-1650 cm^{-1} was also found in both sets of powders at 550°C as a result of vibrations from water adsorbed to particle surfaces[165]. Upon cleaning, these peaks are eliminated in ZAO; however, broader peaks at lower wavenumbers (1454 and 1345 cm^{-1}) are found in YZAO, suggesting carbonates are partially removed and more loosely-bound relative to those present at 550°C[166].

ZAO and YZAO nanoparticles were coarsened at 850°C and 900°C for up to 4 hours to analyze the effects of doping on coarsening. ZAO and YZAO crystallite sizes were measured at 13.0 nm and 13.3 nm, respectively, after cleaning. All curves showed a typical coarsening pattern, with fast grain enlargement in early stages of coarsening and a plateau at longer times which is dependent on temperature and composition. As shown in **Figure 4.6**, ZAO nanoparticles coarsened to an average diameter of 24.5 nm when subjected to a temperature of 850°C for 4 hours while YZAO only grew to 19.0 nm. Similar trends were observed at 900°C where ZAO underwent more growth (29.8 nm) than YZAO (22.6 nm) at 4 hours. The coarsening curves at both temperatures

show a clear difference in growth behaviors for doped and undoped nanoparticles where YZAO particles undergo limited growth, potentially due to enhanced surface stability from Y^{3+} segregation as discussed further in the paper.

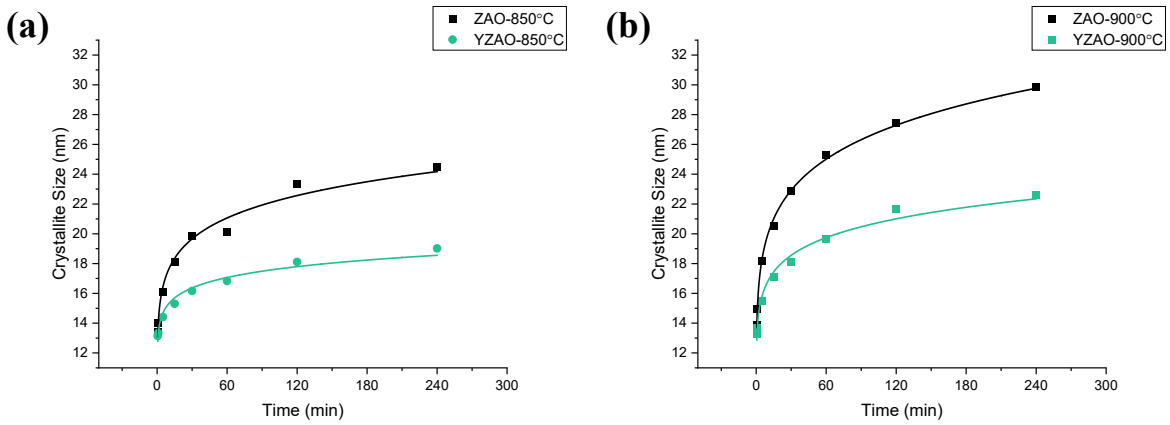

Figure 4.6: Coarsening curves at (a) 850°C and (b) 900°C for clean ZAO and YZAO powders with crystallite sizes estimated using XRD. YZAO particles grow less than 1 nm between 2 and 4 hours at 850°C while ZAO continues growing up until the 4-hour mark, with a similar trend found in data collected at 900°C. These results indicate doped nanoparticles undergo limited growth relative to their undoped counterparts which may be attributed to surface segregation of dopants.

4.3.3: Surface stability characterization

Anhydrous surface energies of clean ZAO and YZAO were measured using water adsorption microcalorimetry to understand the difference in coarsening behaviors and directly test the predicted reduction in surface energies. The method relies on using water as a probe for surface reactivity and utilizing thermodynamic models to correlate the heats of adsorption to the surface energies of the particles. **Figure 4.7** shows the adsorption isotherm along with the enthalpies of water adsorption for ZAO and YZAO. In **Figure 4.7a**, a typical type-II isotherm demonstrates water molecules adsorbed strongly to surfaces as low pressures, consistent with a chemisorption process (i.e., dissociative) and a change in slope above a relative pressure of 0.05. As shown in the inset, Y-doped samples show slightly lower slopes, consistent with lower surface reactivities. As the adsorption progresses, the curves converge as water adsorption becomes more physical (i.e., without dissociation). The small step at 0.4 is an artificial inconsistency caused by an automatic

shift in the pressure gauge. **Figure 4.7b** shows the enthalpies of adsorption as a function of water coverage. For both samples, the water reactivity is high at low coverages, attributed to dissociation reactions, and decreases with increasing coverage. Generally, more exothermic heats at similar coverages are observed in ZAO compared to YZAO, indicating improved surface stability (less reactivity) of Y-doped zinc aluminate nanoparticles.

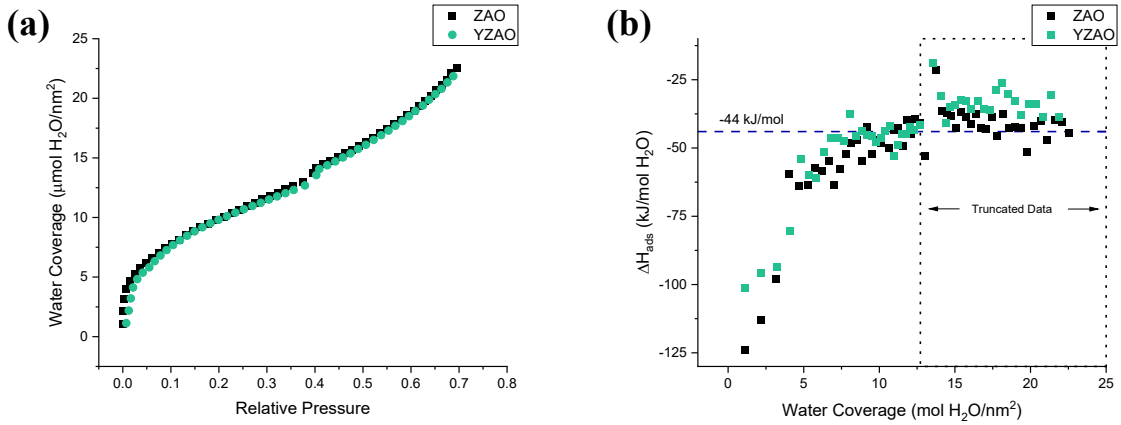

Figure 4.7: (a) Adsorption isotherm and (b) enthalpies of adsorption as a function of surface coverage for both ZAO and YZAO nanoparticles obtained via water adsorption microcalorimetry with a dashed line at the heat of liquefaction of water (-44 kJ/mol)[157]. The dotted line indicates data that was neglected for surface energy measurements due to low (in magnitude) heats of adsorption resulting from a combination of heat effects. Lower (in magnitude) enthalpies of adsorption in YZAO imply enhanced surface stability upon doping.

After successive dosing, the enthalpies of water adsorption converged to the enthalpy of liquefaction of water which has a theoretical value of -44 kJ/mol[157]. In **Figure 4.7**, both ZAO and YZAO particles plateau at -44 kJ/mol between coverages of 10.5-12.5 mol H_2O/nm^2 but continue to decrease in magnitude past this point. This increase signals an additional endothermic reaction taking place throughout the process of physical adsorption of water, such as the formation of yttrium and zinc hydroxides on the surface which is thermodynamically favorable[167,168]. These additional processes convolute the heat effects at high coverages, making it difficult to determine the enthalpy of water adsorption. Because processes like hydroxide formation have relatively slow kinetics at room temperature and neutral pHs, we assume these reactions are negligible at low coverages and, therefore, both sets of data could be safely truncated prior to the endothermic event

at 12.5 H_2O/nm^2.This does not impact the surface energy calculations as detailed by Castro and Quach[158] and later by Drazin and Castro[157]. Therefore, anhydrous surface energies were calculated for both samples using the thermodynamic model for water adsorption developed by Castro and Quach[158]. The method uses a thermodynamic description of the adsorption of water to the surfaces of particles. During the process, the free energy of the system is reduced as water adsorption progresses. If the bulk energy is unaffected by the adsorption process and one assumes negligible entropic and PV terms, the surface energy change can be calculated by:

$$\gamma_{S,\theta} = \gamma_s + \theta \cdot \Delta H_{ads} \qquad \textbf{(4.6)}$$

where ΔH_{ads} is the measured heat of adsorption, γ_s is the anhydrous surface energy, and $\gamma_{S,\theta}$ is the surface energy at a given surface coverage, θ. To minimize the contributions from the chemical potential of water, the surface energy was assumed to be equivalent to the surface energy of liquid water, 0.072 J/m^2, at the point where the heats of adsorption converged to -44 kJ/mol. Beyond this point, adsorption peaks represent water molecules adhering to layers of water on the surface[157]. By doing so, the heat of adsorption data was used to calculate the anhydrous surface energies of both sets of nanoparticles as with other nanocrystalline oxides[98,100,156,158].

The calculations resulted in surface energies of 0.99 (±0.02) and 0.85 (±0.02) J/m^2 for ZAO and YZAO, respectively. The decrease in measured surface energy for YZAO from that of ZAO suggests that surface stability is indeed enhanced by doping zinc aluminate with Y^{3+} which further supports the predictions from molecular dynamics simulations. Reported errors result from assuming a 0.15% uncertainty in relative pressures in addition to a 2% uncertainty in BET surface areas[158].

As simulations indicate the cause for the reduced surface energies to be dopant segregation to the surfaces, EELS mapping was performed on coarsened YZAO particles to analyze the segregation behavior of Y^{3+}. EELS maps and results from successive box scans on an individual Y-doped nanoparticle are included in **Figure 4.8**. **Figure 4.8a** shows the survey image, with **Figure 4.8b** indicating the box for the spectroscopic study. Due to its low concentration, it is difficult to visualize Y^{3+} in the EELS map, but it is apparent that Al^{3+} ions are accumulated near the vicinity of the surface as evident from the purple shade. This is supported by the results from the box scans which illustrate that there is Al^{3+} enrichment (represented in red) within 3 nm of the surface edge, corroborating previous reports of excess Al segregating to interfaces in Al-rich

spinels[95,96,118]. The box scans further reveal this region is depleted in Y^{3+}, but as we move toward the surface edge, the spectrum detects a sharp increase in Y^{3+}. This increase in Y^{3+} concentration coincides with lowering of Zn^{2+} and Al^{3+}, further validating the claims of Y^{3+} segregation to zinc aluminate surfaces. It is interesting to observe that the defect chemistry involved in the segregation of Y^{3+} to the surface is significantly more complex than the molecular dynamics simulations. That is, the surface effect on ion distribution impacts a thickness of roughly 3 nm because of the redistribution of Al^{3+} and Y^{3+}. The Zn^{2+} distribution remains mostly constant, suggesting Y^{3+} and Al^{3+} are sharing octahedral sites in the spinel structure. The large ionic radii of Y^{3+} atoms lead to large lattice strains which drive them toward the surfaces which forces Al^{3+} to redistribute accordingly. Despite the simplified defect chemistry, molecular dynamics effectively predicted the segregation of Y^{3+}.

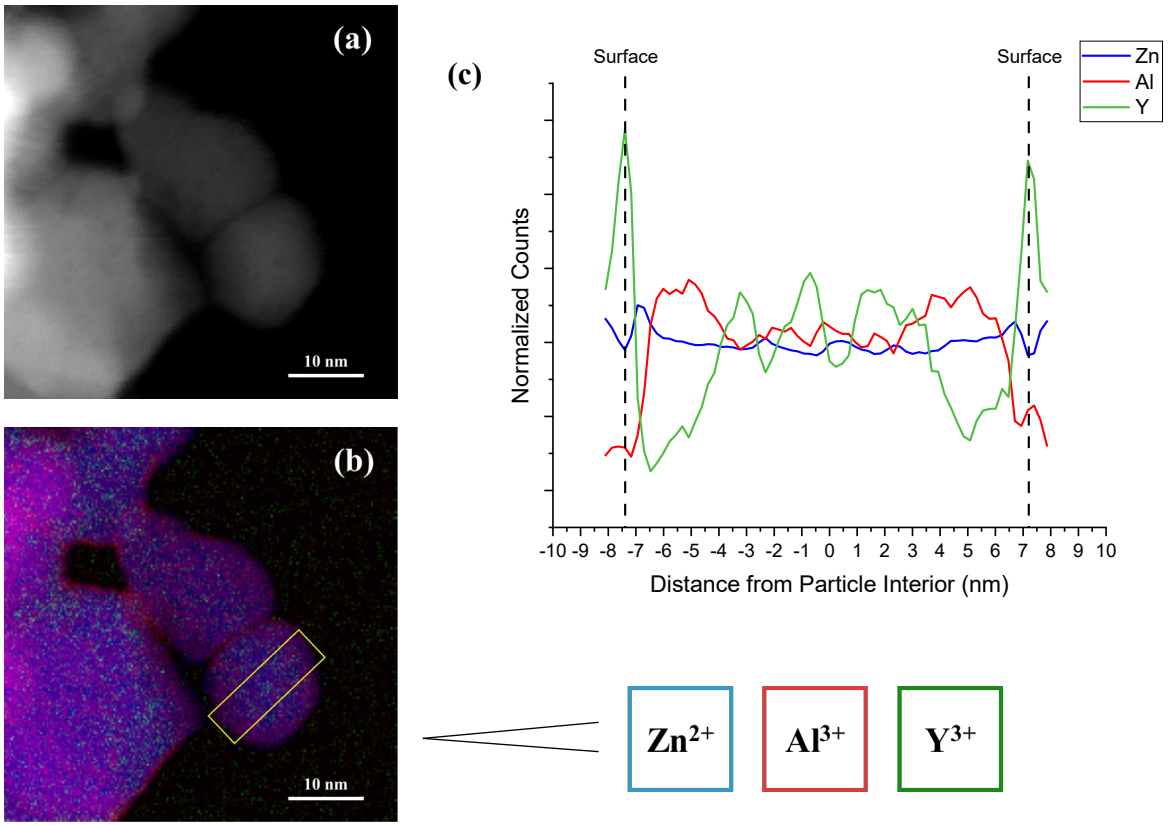

Figure 4.8: (a) Dark field TEM image of YZAO nanoparticles coarsened at 900°C for 1 hour, (b) elemental map of Zn (blue), Al (red), and Y (green) taken with EELS, and (c) normalized counts of each zinc aluminate cation measured by successive box scans across the region boxed in yellow. The EELS map indicates there are two layers near particle surfaces that contain different compositions than the bulk: approximately 3-6 nm away from the center of the particle, there is an increase in the Al content followed by a spike in Y at the surface. Al-enrichment near particle surfaces is also obvious in the colored map (b).

4.3.4: Discussion

Ostwald ripening theory states that particle growth follows a cubic time dependence with as outlined in **Equation 4.1**. The equation presents two main parameters to potentially control grain enlargement: the surface energy and diffusion coefficient. There is limited work focused on decoupling these components to provide a holistic understanding of coarsening control; to that end, each coarsening curve for doped and undoped zinc aluminate was plotted with a cubic dependence (**Figure 4.9**).

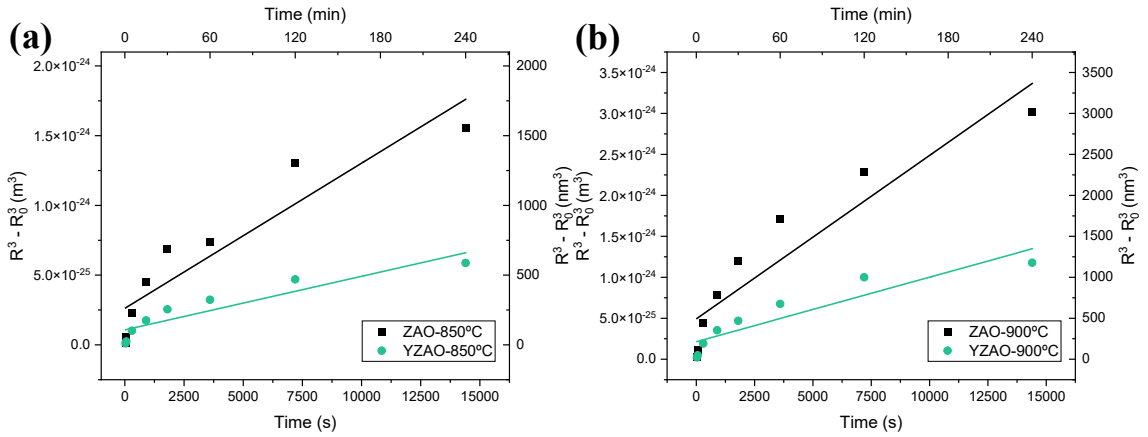

Figure 4.9: Coarsening data for both compositions at (a) 850°C and (b) 900°C plotted according to the Ostwald ripening equation[101]. A linear fit is overlayed on each set of data, although crystallite sizes deviate from this fit as particles grow.

At first glance, each set of data in **Figure 4.9** reasonably fits a linear dependence with time; however, upon further inspection, the linear approximation overestimates crystallite sizes at short times (less than 5 minutes) and underestimates them at longer times. The fact that this crossover is present in all four curves suggests that either (1) the defining rate constant for Ostwald ripening changes throughout the coarsening process or (2) the growth mechanism transitions from Ostwald ripening to a slower mechanism (e.g., migration and coalescence) as particles enlarge.

Shifts in growth mechanisms involving Ostwald ripening have been reported in the past for metal nanoparticles[140,169]. Hansen et al. observed nickel nanoparticles in a magnesium aluminate matrix under a TEM where they noticed particle migration and coalescence even 13 seconds after being exposed to elevated temperatures[140]. A transition in growth mechanisms is indicative of a change in the relative activation energies for two mechanisms; in the case of the nickel nanoparticles, the transition from Ostwald ripening to migration and coalescence is attributed to the severe decrease in vapor pressure as particle sizes increase[140]. Shifts away from Ostwald ripening are more likely in metals than ceramics: ceramic vapor pressures are much lower than in metals even at the nanoscale[170], so ripening likely occurs via different transport mechanisms than in metals. Additionally, these types of transitions typically lead to sharp changes in slopes for plots of crystallite sizes over time[169]. The coarsening curves in **Figure 4.6** instead show gradual changes in growth rate for both compositions at 850°C and 900°C which imply that

this shift in zinc aluminate growth behavior is unlikely to be due to a change in the dominant growth mechanism. Instead, the crossover in the Ostwald ripening curves could be attributed to a decrease in the rate constant throughout the growth process. This change could result from a reduced diffusion coefficient or a continuous decrease in surface energies as particles grow.

For the purposes of comparing the effects of dopant segregation on the coarsening behaviors of doped and undoped zinc aluminate nanoparticles, we assume that changes in growth mechanisms and/or rate constants (i.e., surface energies) are negligible within the first five minutes of coarsening. Data before and at five minutes was used to calculate self-diffusion coefficients for both samples at 850°C and 900°C using a modified version of the Ostwald ripening rate constant developed by Lifshitz and Slyozov which assumes atmospheric air acts as an ideal gas:

$$K = \frac{8\gamma_s P V_m^2 D}{9R^2T^2} \qquad \textbf{(4.7)}$$

where γ_s is the surface energy, P is the vapor pressure, V_m is the molar volume, D is the diffusion coefficient of the material, R is the ideal gas constant, and T is the temperature[101]. Although the ideal gas assumption is questionable at room temperature, these calculations still provide a basis for comparing the kinetics of Ostwald ripening in both zinc aluminate samples. Diffusion coefficients for ZAO and YZAO along with experimental and computational surface energies are summarized in **Table 4.2**. Diffusion coefficients calculated for both undoped and Y-doped zinc aluminate are on the order of 10^{-12} cm^2/s which agrees well with diffusion coefficients calculated for other solids at similar temperatures[171,172]. Juxtaposing these values makes it evident that self-diffusion is faster in undoped zinc aluminate than Y-doped zinc aluminate at both temperatures.

Dopant Content	γ_s (J/m^2)	$\gamma_{s,MD}$ (J/m^2)	$D_{850°C}$ (cm^2/s)	$D_{900°C}$ (cm^2/s)
Undoped	0.99 (±0.02)	1.55	4.8×10^{-12}	10.1×10^{-12}
0.5 mol% Y_2O_3	0.85 (±0.02)	1.50	2.5×10^{-12}	5.1×10^{-12}

Table 4.2: Surface energies and self-diffusion coefficients calculated for doped and undoped zinc aluminate nanoparticles.

On an atomistic scale, a change in diffusion coefficient for YZAO represents a change in the rate-controlling defect for zinc aluminate self-diffusion. This defect can be identified experimentally by calculating activation energies for self-diffusion from coarsening studies and comparing with literature values for defect formation energies; however, the present coarsening studies were limited to two temperatures which would skew such calculations. Unfortunately, to the best of our knowledge, no work has been done to identify the defects dominating diffusion in zinc aluminate, but Ting and Lu found diffusion in magnesium aluminate to be controlled primarily by Schottky defects with the slowest diffusing species being oxygen vacancies[102]. Given that magnesium aluminate is isostructural with zinc aluminate (spinel), it is reasonable to assume defect formation energies in to be similar in both materials. Hence, the dominant defect reaction in zinc aluminate may be described by:

$$\Phi = V_{Zn}'' + 2V_{Al}'' + 4V_O^{\cdot\cdot} \qquad \textbf{(4.8)}$$

with oxygen vacancies being the rate-controlling species. This would corroborate the trends in diffusion coefficients between doped and undoped samples: because oxygen vacancies are positively charged defects, cationic dopants in zinc aluminate (e.g., Y^{3+}) would prevent the formation of oxygen vacancies, thus hindering diffusion. Furthermore, the positive charge caused by excess Y^{3+} in the surface layer would need to be accommodated by negatively charged defects[97]. A candidate defect reaction is the delocalization of Al^{3+}:

$$Al_{Al}^{\times} + Y_i^{\cdots} \rightarrow Y_{Al}^{\times} + Al_i^{\cdots} \qquad \textbf{(4.9)}$$

where this would likely be compensated by site inversion with the tetrahedral site, similar to magnesium aluminate[97]. Some accumulation of Al^{3+} is already found in the elemental maps in **Figure 4.8**, which supports the claim that this series of defects could be leading to the distinct diffusive properties in ZAO and YZAO.

4.4: Conclusions

This work focused on the possibility of tailoring the growth behavior of zinc aluminate nanoparticles by tuning the thermochemistry of its surfaces. Molecular dynamics simulations indicated that among several trivalent dopants, Y^{3+} is the most likely to segregate to the surface of nanoparticles. Despite the assumptions made in the simulations, synthesized zinc aluminate doped with 0.5 mol% Y_2O_3 indeed showed excess Y^{3+} was located at particle surfaces along with a more complex distribution of ions near the surface regions. Al^{3+} ions were depleted from the surface edge but enriched in the immediate vicinity (within 3 nm of surfaces). Water adsorption microcalorimetry estimated a reduction in surface energy for doped samples consistent with the segregated Y^{3+}. Coarsening studies demonstrated that doped (YZAO) and undoped (ZAO) zinc aluminate nanoparticles grow by Ostwald ripening, where YZAO exhibits resistance to coarsening compared to ZAO. This behavior results from a combination of a reduced driving force for coarsening and a decrease in diffusion coefficient. The latter likely stems from the unique chemistry in the surface regions which impedes the formation of the rate-limiting defect in zinc aluminate. The present work represents an important step toward controlling the coarsening behavior of nanoparticles to enable the design of stable catalytic materials.

Chapter 5: Enhanced Grain Boundary Stabilities in Y-Doped Zinc Aluminate

Abstract

The idea that ceramics exhibit elevated mechanical properties at the nanoscale has been shrouded in controversy, primarily due to conflicting reports of grain size hardening at small grain sizes. This study focuses on improving the stability of nanocrystalline zinc aluminate grain boundaries to better control and predict its mechanical behavior. Atomistic simulations on Σ3 and Σ9 grain boundaries showed that trivalent ions of varying ionic radii [Sc^{3+} (74.5 pm), In^{3+} (80.0 pm), Y^{3+} (90.0 pm), and Nd^{3+} (98.3 pm)] tend to segregate to both interfaces, with Y^{3+} having the highest segregation potential. Average grain boundary energies were measured for nanoceramics fabricated by high-pressure spark plasma sintering using differential scanning calorimetry. The results revealed that doping zinc with Y^{3+} (at 0.5 mol% Y_2O_3) reduces the average grain boundary energy of zinc aluminate from 1.1-1.3 J/m^2 to 0.6-0.8 J/m^2. The noted decrease in interfacial energies for doped samples suggests it is indeed possible to alter the stability of zinc aluminate grain boundaries via dopant segregation and implies that the mechanical performance of doped samples will surpass that of undoped ones.

5.1: Introduction

Nanocrystalline ceramics exhibit elevated hardness and optical transparency that make them prime candidates for next-generation armored windows[24,26,27,70]. These properties combined with its relatively high thermal conductivity (20-25 $W \cdot m^{-1} \cdot K^{-1}$) make nanocrystalline zinc aluminate ($ZnAl_2O_4$) particularly interesting in environments with high temperature gradients, such as missile domes and laser gain media[173].

High hardness values around 20 GPa are consistently reported across this class of ceramics[24,26,27,70], but deformation mechanics remain difficult to predict and are not well-understood. For instance, the Hall-Petch relationship which defines grain size hardening has conflicting reports surrounding its breakdown at small grain sizes even within the same material system[24,27,33]. Additionally, there is limited knowledge of the fracture mechanics of nanocrystalline ceramics due to experimental limitations surrounding these measurements[64,125,174]. Researchers have recently begun to use grain boundary thermochemistry to elucidate the mechanical behavior

of these systems[64,70]. Nanomaterials inherently exist in metastable states due to the high excess energy contributed by their extensive network of grain boundaries. This excess energy can lead to significant coarsening during processing or operating steps as well as activate deformation mechanisms such as grain boundary shearing, affecting the mechanical performance during operation[13,24,26,27,33].

Solute segregation to grain boundaries has been found to improve grain boundary stability in a number of metals[10,59,110] and ceramics[50,54,55,64]. **Equation 5.1** is derived from the Gibbs adsorption isotherm and establishes the relationship between the concentration of segregated dopants and the grain boundary energy of doped systems[85,92].

$$\gamma_{gb} = \gamma_{gb0} - \Gamma_B(RTlnX_B - \Delta H_{seg}) \qquad \textbf{(5.1)}$$

Here γ_{gb} represents the grain boundary energy of the doped material, γ_{gb0} is the grain boundary energy of the undoped material, Γ_B is the solute excess at the grain boundary, X_B is the concentration of the dopant, and ΔH_{seg} is the enthalpy of segregation of the dopant to the grain boundary[85,92]. This relationship states that the average grain boundary energy of a doped specimen will always be lower than that of an undoped specimen, provided the dopant has a favorable segregation enthalpy. Ionic radius and valence state differences between the dopant and matrix ions are among the key parameters affecting the segregation energy[94]. However, more studies are still needed to establish a predictive function.

Hu et al. applied this concept to nanocrystalline Ni-Mo alloys by comparing the Hall-Petch breakdown for samples with varying concentrations of Mo[110]. This work found that the critical grain size for the Hall-Petch inversion could be lowered by increasing the concentration of Mo since Mo segregates to Ni grain boundaries[110]. Using transmission electron microscopy, Hu et al. revealed that samples with high Mo contents underwent limited amounts of grain boundary migration, even at low grain sizes[110]. In essence, this showed that Mo segregation enhanced grain boundary stability in nanocrystalline Ni which preserved dislocation dominated deformation at small grain sizes[110].

Dopant segregation has also been found to impact fracture toughness in nanocrystalline ceramics[64]. A study by Bokov et al. involved doping yttria-stabilized zirconia with three different concentrations of La and juxtaposing the indentation toughness with average grain boundary energies (as measured by differential scanning calorimetry) for each[64]. In doing so, Bokov et al.

did estimate a reduction in grain boundary energies with increasing La contents as predicted by the Gibbs adsorption isotherm[64]. Furthermore, the lowering of grain boundary energies coincided with increases in indentation fracture toughness[64]. The calculated increase in toughness was reportedly due to the preferential segregation of La to high-energy grain boundaries: this served to level the energetic landscape within the material which, in turn, made cracking more stochastic in nature[64]. By directly correlating improved grain boundary stabilities with enhanced toughness in nanocrystalline yttria-stabilized zirconia, Bokov et al. demonstrated that interfacial energies can provide direct insight into a nanoceramics' mechanical performance.

The grain size dependence of a nanomaterial's grain boundary energies must be known to fully predict its mechanical properties; however, this dependence becomes unclear when using dopant segregation to reduce grain boundary energies. As grain boundary area decreases in a material (i.e., grain sizes increase), the amount of dopant in the system will remain the same, so the grain boundary excess (Γ_B in **Equation 5.1**) will increase until reaching a saturation point. Beyond this point, dopant-rich second phases begin forming which can negatively impact hardness and toughness[175]. Muche et al. observed this in La-doped magnesium aluminate which had grain boundary energies about 0.15 J/m^2 lower than those in undoped samples[55]. Despite lowering grain boundary energies, La-doped samples were found to have a weak grain size dependence, indicating grain boundaries were saturated with dopants at fairly low grain sizes.

The present work examines the dependence of the grain boundary energy of zinc aluminate on the presence of ionic dopants. Initially, the grain boundary stabilities of undoped zinc aluminate are compared with those of zinc aluminate doped with four different trivalent solutes [Sc^{3+} (74.5 pm), In^{3+} (80.0 pm), Y^{3+} (90.0 pm), and Nd^{3+} (98.3 pm)]. All dopants have the same charge as Al^{3+} but the range of ionic radii allows us to gauge the effects of elastic strain on the segregation behavior. Molecular dynamics simulations on two zinc aluminate grain boundary structures (Σ3 and Σ9) indicated Y^{3+} has the highest propensity to segregate among the studied dopants, assuming the dominant defect involves substituting for Al^{3+} in octahedral sites.

Following the simulation results, high-pressure spark plasma sintering was used to produce fully dense undoped zinc aluminate and zinc aluminate doped with 0.5 mol% Y_2O_3. The sintered nanoceramics were were subjected to a set of differential scanning calorimetry experiments to determine their grain boundary energies as a function of grain size. The results showed lower grain boundary energies for Y-doped zinc aluminate for all studied grain sizes, consistent with the

theoretical predicts. The results from this work show that trivalent dopants can indeed alter the grain boundary stabilities of nanocrystalline zinc aluminate, suggesting that zinc aluminate hardness and fracture toughness will improve by decorating its grain boundaries with Y^{3+}.

5.2: Methods and Experimental Procedures

5.2.1: Atomistic simulations on grain boundary structures

Molecular dynamics simulations were used to analyze the segregation behavior of four dopants [Sc^{3+} (74.5 pm), In^{3+} (80.0 pm), Y^{3+} (90.0 pm), and Nd^{3+} (98.3 pm)] to zinc aluminate grain boundaries. Two grain boundary structures were analyzed: one featured two Σ3 (111) tilt grain boundaries (22176 atoms) while the other had two Σ9 (001) tilt grain boundaries (22400 atoms). The Σ3 structure was the same structure generated in GB Studio by Hasan et al. for magnesium aluminate[50,176]. The Σ9 structure was developed by constructing gamma surface maps for grain boundary structures with misorientation angles between 0 and 180° while ensuring the resulting structure had both grain boundaries in the simulation cell and relatively low energies. Each structure was visualized with OVITO[144] and all calculations were performed with LAMMPS[145] using Buckingham pair potentials (listed in **Table 4.1**) to estimate short-range interactions[146].

The grain boundary energy of each structure was calculated after minimization by taking the difference between the potential energy of the grain boundary structure and the potential energy of a bulk structure using **Equation 5.2**:

$$\gamma_{gb0,MD} = \frac{1}{2A}(E_{gb} - E_{bulk}) \qquad \textbf{(5.2)}$$

where $\gamma_{gb0,MD}$ is the grain boundary energy of the undoped grain boundary structure, A is the grain boundary area, and E_{gb} and E_{bulk} are the potential energies of the grain boundary and bulk structure with the same number of atoms[50].

Segregation energies for each dopant were estimated using the dopant replacement method as detailed by Hasan et al.[50]. Dopants were substituted into Al^{3+} sites then the nanoparticle was subjected to an energy minimization step to record its potential energy as a function of the dopant position in the structure[50]. Segregation energies, E_{seg}, were estimated for each dopant as the difference between a substitution in the bulk and a substitution in the grain boundary. The dopant concentration in the grain boundary layer was assumed to be beyond the dilute limit since the range

of grain sizes in the experimental work are expected to have a non-negligible number (about 5%) of trivalent sites occupied by the dopant. Given this, all segregation and grain boundary energies were taken as averages across all trivalent sites.

Segregation energies and experimental dopant concentrations (measured by electron microprobe analysis) were used to calculate grain boundary energies for both structures with **Equation 5.3**:

$$\gamma_{gb,MD} = \gamma_{gb0,MD} - (\frac{n}{A})E_{seg} \qquad \textbf{(5.3)}$$

where $\gamma_{gb,MD}$ is the grain boundary energy of the doped structure, n is the number of dopants in the system (about 0.5 mol% Y_2O_3), A is the grain boundary area of the structure, and E_{seg} is the segregation energy of each dopant. Only qualitative conclusions can be extracted from this computational study due to the number of assumptions made regarding the electrostatic interactions between dopants and the zinc aluminate matrix, but trends across each structure and dopant will serve to enrich the experimental portion of this work.

5.2.2: Synthesis and nanopowder characterization

Undoped zinc aluminate (ZAO) powder was synthesized using a modified co-precipitation method[26,118,150,151]. $Zn(NO_3)_2 \cdot 6H_2O$ and $Al(NO_3)_3 \cdot 9H_2O$ (Sigma Aldrich, >98%) were dissolved in deionized water in the metal stoichiometric molar ratio of 1:2. Water contents of each nitrate precursor were measured prior to synthesis to ensure the stoichiometric ratios were accurately maintained. Hydroxide nanoparticles were precipitated under a 2 mol/L aqueous ammonia solution at a constant pH of 8.75 to limit the formation of $Zn(NH_3)_4^{2+}$, which would ultimately lead to a Zn-deficient precipitate[26,118,150,151]. Following the synthesis, hydroxide precipitates were immediately washed three times with ethanol and dried in an oven at 80°C for 48 hours. The same technique was used to synthesize Y-doped zinc aluminate (YZAO), except $Y(NO_3)_3 \cdot 6H_2O$ (Sigma Aldrich, >98%) was also dissolved in the nitrate precursor solution to give a concentration of 0.5 mol% Y_2O_3 in the precipitate. Dried precipitates were ground into fine powders and calcined in a Thermo Scientific Lindberg/Blue M (Thermo Fisher Scientific Inc., Waltham, MA) box furnace at 550°C for 4 hours to crystallize the spinel phase with limited grain growth[26,118,152].

X-ray diffraction (XRD) on a Bruker D8 (Bruker, Billerica, MA) operated at 40 kV, 40 mA (CuKα radiation, λ=1.5406 Å) was used to perform phase and crystallite size analyses of each set of powders. Crystallite sizes were estimated using Match! (Crystal Impact, Bonn, Germany) software with reference pattern #96-900-7021 (Levy et al.[153]). These measurements were supported by scanning transmission electron microscopy (STEM) images from both powders on a JEOL-ARM300F Grand ARM (JEOL, Peabody, MA).

Electron microprobe analysis (EMPA) on a Cameca SX-100 (Cameca, Gennevulliers, France) was used to estimate Al:Zn stoichiometric ratios of ZAO and YZAO powders. 10 scans were taken across each sample and averaged to reveal that stoichiometric ratios were within error of one another: 2.16 (±0.14) and 2.11 (±0.06) for ZAO and YZAO, respectively.

5.2.3: Spark plasma sintering

Doped and undoped powders were degassed at 400°C for over 16 hours in a Micromeritics SmartVacPrep (Micromeritics Instrument Corp., Norcross, GA) to remove water adsorbed onto particle surfaces. Following this, powders were transferred to a glovebox where they were preserved in a dry nitrogen atmosphere (below 0.6% relative humidity) prior to sintering.

Each sample was sintered by high-pressure spark plasma sintering (HP-SPS) where the setup consisted of an inner die (inner diameter (ID): 4 mm, outer diameter (OD): 19 mm) made of diamond/SiC composite (Hyperion Materials & Technologies, Deerfield Beach, FL)[27,64,70,93]. Punches composed of the same material with diameters that fit those of the inner die were placed on the top and bottom of the die to transfer the load onto the green body. This setup was encapsulated by a larger graphite die (ID: 19 mm, OD: 45 mm) which served to maintain the current path and insulate the inner die.

Samples were sintered in an SPS model 825S (Syntex Inc., Kawasaki, Japan) at temperatures of 800-900°C and pressures of 1.2-2.0 GPa to achieve full density at a range of grain sizes. After sintering, each pellet was annealed at 150°C below its sintering temperature to release residual strain and allow for oxidation of carbon and any potentially reduced elements.

5.2.4: Pellet characterization

After polishing flat with 800 grit sandpaper, relative densities were measured for each sample using an Archimedes' balance. Theoretical densities of 4.58 g/cm^3 were used for both ZAO

and YZAO since Rietveld refinement on x-ray diffraction patterns revealed the dopant has a negligible effect on the lattice parameter[177]. Each sample across both compositions was optically transparent and, as such, had relative densities greater than 98%.

Grain sizes before and after differential scanning calorimetry were measured by XRD since all grain sizes were within the range of Scherrer's equation[178]. Match! software and reference pattern #96-900-7021 were used for all grain size measurements[153].

5.2.5: Differential scanning calorimetry

Grain boundary energies were calculated as a function of grain size by subjecting sintered pellets to a series of differential scanning calorimetry (DSC) experiments in a Netzch DSC 404 (Netzch GmbH, Selb, Germany). Samples were heated to final temperatures between 850 and 900°C at 50°C/min to activate grain growth[179]. Following the heating profile, samples were maintained at the final temperature for 15 minutes to ensure grain growth peaks were fully developed. This procedure was repeated three times to establish a baseline to extract the grain growth peak from[179]. High heating rates were employed in this study to help deconvolute the multiple heat signals associated with grain growth. Experiments were run under an Ar environment to prevent oxidation of carbon residue from spark plasma sintering[179].

Grain boundary energies were calculated by normalizing heat signals with the change in grain boundary area using **Equation 5.4**:

$$\Delta H = \Delta\gamma_{gb}\,\Delta A_{gb} \qquad \textbf{(5.4)}$$

where ΔH is the heat from grain growth as measured by DSC, $\Delta\gamma_{gb}$ is the change in grain boundary energy from grain growth, and ΔA_{gb} is the change in grain boundary area[179]. This equation assumes the heat signal at elevated temperatures is entirely attributed to the elimination of grain boundary area (i.e., grain growth), which is an appropriate approximation for this system due to the high densities measured for samples before DSC[50,70]. Grain boundary areas were calculated using **Equation 5.5** with grain sizes measured by XRD:

$$A_{gb} = \frac{S}{D\rho} e^{-2.5(ln\sigma)^2} \qquad \textbf{(5.5)}$$

where A_{gb} is the grain boundary area, S is the shape factor taken to be 3.55 (tetrakaidecahedron grains), D is the grain size, ρ is the density, and σ is the standard deviation of normalized grain

sizes[50,70,179]. The exponential factor associated with grain size distribution was assumed to have a negligible effect on the grain boundary areas since grain sizes were measured by XRD.

Following the protocol by Bokov et al., a set of six DSC experiments were run to solve **Equation 5.4** as a function of grain boundary area (i.e., grain size), where each experiment represented a permutation of three initial states with three final states[70]. The system of equations was then solved by applying realistic boundary conditions: (1) all grain boundary energies are positive and (2) grain boundary energies must increase with grain size[55]. The second assumption is validated in doped samples by the Gibbs adsorption isotherm: grain growth reduces the grain boundary area in a material which further increases dopant concentrations at grain boundaries, hence lowering grain boundary energies[85,92]. This holds true for undoped samples since larger-grained samples are prepared from sintering at higher temperatures and/or for longer times which leads to more stable grain boundary configurations[180].

5.3: Results and Discussion

5.3.1: Analysis of dopant segregation to Σ3 and Σ9 grain boundaries

The Al^{3+} octahedral sites in zinc aluminate were replaced by each individual dopant (Sc^{3+}, In^{3+}, Y^{3+}, Nd^{3+}) in structures containing Σ3 and Σ9 grain boundaries. Dopants were substituted in the bulk region of the grain and moved stepwise toward the grain boundary regions. The energy was minimized after each substitution. **Figure 5.1** outlines the results from these molecular dynamics simulations which identified Y^{3+} as the dopant with the highest segregation energies to both grain boundaries. **Figure 5.1a** and **Figure 5.1b** depict cumulative distribution functions for each dopant in the Σ3 and Σ9 grain boundary, indicating Y^{3+} contains the highest number of favorable sites (high segregation energy) of all dopants.

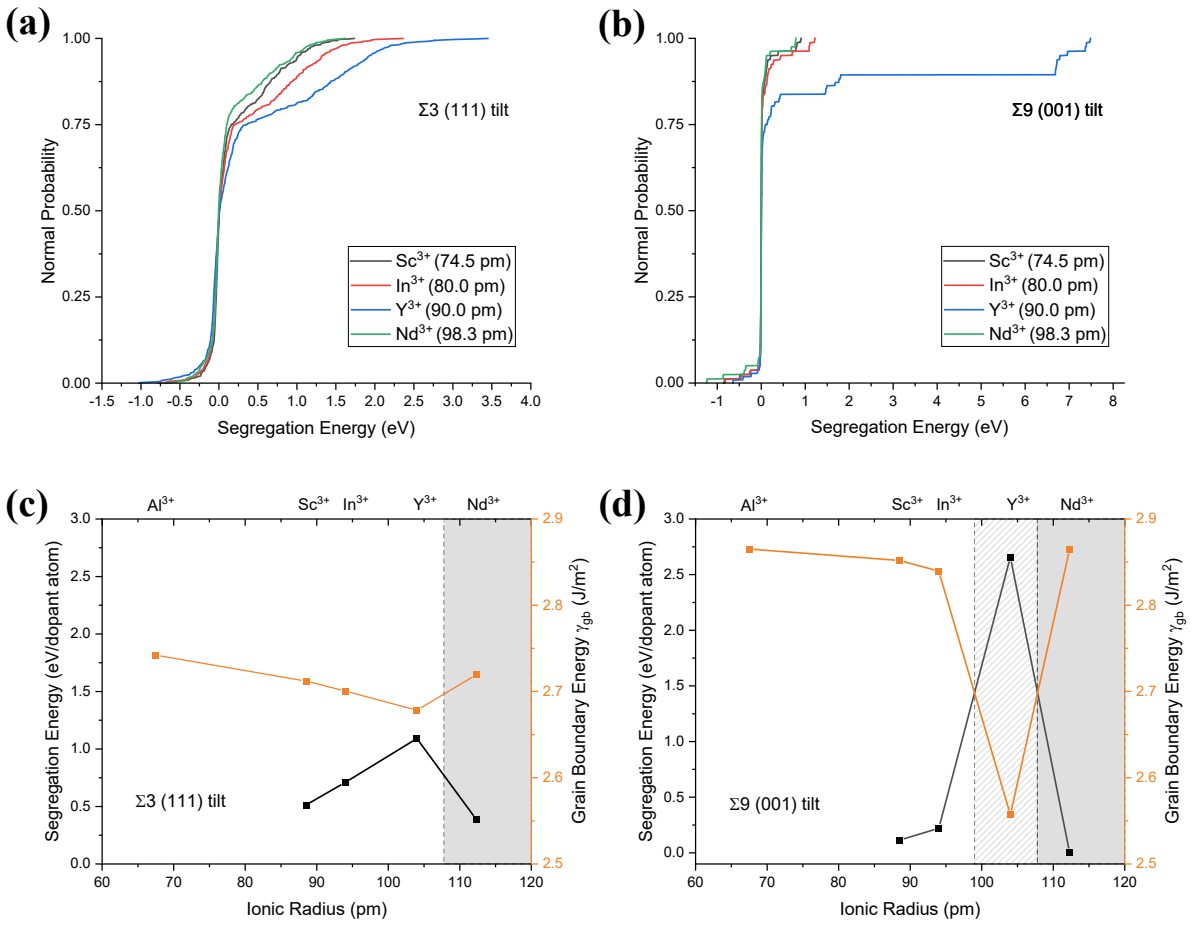

Figure 5.1: (a) and (b): Segregation energies for each dopant to zinc aluminate (a) Σ3 (111) and (b) Σ9 (001) tilt grain boundaries plotted as cumulative distribution functions. (c) and (d): Average segregation and grain boundary energies calculated assuming 0.5 mol% Y_2O_3 for (c) Σ3 (111) and (b) Σ9 (001) tilt grain boundaries. The regions shaded in grey in (c) and (d) indicate a breakdown in the correlation between segregation energy and dopant ionic radius, while the light grey region in (d) points out the remarkably high segregation energy for Y^{3+}.

Average segregation energies for all four dopants were positive in both grain boundary structures, indicating grain boundary sites are more favorable substitution sites than bulk sites. This is likely due to the limited coordination at the grain boundary region: this allows for improved accommodation of the elastic strain introduced by large dopants as previously proposed for Y-doped alumina. Grain boundary energies were calculated for each structure to explore the potential link between segregation and grain boundary energy outlined in **Equation 5.1**.

Grain boundary energies were around 2.5-2.9 J/m^2 for each of the two structures which are significantly higher than those experimentally reported for zinc aluminate and other nanocrystalline oxides[55,64,70,104,118]. The discrepancy can either be related to the uncertainty in the pair potentials used or the assumptions made in the simulations. For example, the formation of space charge layers and spontaneous site inversion have been reported to lower excess energies in spinel interfaces by rearranging atoms in lower energy states[94,97]. This explanation is consistent with data available in literature for simulations on doped and undoped magnesium aluminate which showed similar discrepancies in grain boundary energies under the same assumptions[50].

Each plot in **Figure 5.1** indicates that Y^{3+} has more favorable segregation than all other dopants in the study. Conversely, structures doped with Nd^{3+} have the lowest segregation energies despite having the highest ionic radius in the study (98.3 pm). This result is intriguing as one generally expects a direct correlation between segregation energies and ionic radii since higher ionic radii introduce greater elastic strain in the bulk, making the more relaxed interfacial regions more energetically favorable[94]. The fact that this expected behavior breaks down for Nd^{3+} may be suggesting there is maximum ionic radius that the grain boundary can accommodate. Beyond this, added strain leads to diminishing improvements in grain boundary energies. It is important to note that segregation is still energetically favorable for this ion, but with lower segregation energy.

As shown in **Figure 5.1d**, the large segregation energies calculated for Y^{3+} in the Σ9 structure also suggests there is a critical range of ionic radii where dopants segregate to the grain boundaries to a greater extent. A similar behavior is seen for Σ3, but with less intensity. This range could depend on the nature of the grain boundary in terms of misorientation, but a more systematic study across more dopants and grain boundary structures would be required to evaluate this hypothesis.

By comparing segregation energy trends between both grain boundaries, it is apparent that Y^{3+} exhibits elevated segregation to Σ9 grain boundaries in comparison to Σ3 boundaries. This behavior is expected since the low coordination of Σ9 boundaries makes it easier to compensate for the elastic strain introduced by large dopants[64]. This result suggests that Y^{3+} may preferentially segregate to high-energy grain boundaries in zinc aluminate.

5.3.2: Experimental grain boundary energy measurements

Doped and undoped zinc aluminate pellets were sintered to three distinct grain sizes by spark plasma sintering at various temperatures and pressure between 800-900°C and 1.2-2.0 GPa. The sintering conditions are listed in **Table 5.1** demonstrating that generally higher temperatures lead to further densification and coarsening, while pressure helps preserve small grain sizes. The conditions used in this study were based on previous experience using an experimental grid targeting roughly 1/3 of the melting point to minimize coarsening. XRD indicated all produced samples had the characteristic zinc aluminate spinel structure.

For the grain boundary energy measurements, the sintered samples were subjected to grain growth inside a DSC up to three maximum temperatures: 850°C, 875°C, and 900°C. Maximum DSC temperatures were selected to activate measurable heats of grain growth while reaching significantly different final (post-DSC) grain sizes and preventing the formation of second phases in doped zinc aluminate samples. Different final states are needed due to the mathematical nature of the protocols used to calculate grain boundary energies. That is, the initial (pre-DSC) and final (post-DSC) grain sizes along with the heats of grain growth between the two states were used to establish a linear system of equations according to **Equation 5.4** for ZAO and YZAO. The measured heats of grain growth represented transitions between two of the distinct initial and final states shown in **Table 5.1**:

Sample	Initial State (Pre-DSC)		Final State (Post-DSC)	
	Designation (State X)	**SPS Temperature (°C)**	**Designation (State Y)**	**DSC Temperature (°C)**
ZAO-14	State 1	800	State 4	850
ZAO-15	State 1	800	State 5	875
ZAO-16	State 1	800	State 6	900
ZAO-25	State 2	850	State 5	875
ZAO-26	State 2	850	State 6	900
ZAO-36	State 3	900	State 6	900
YZAO-14	State 1	850	State 4	850
YZAO-15	State 1	850	State 5	875
YZAO-16	State 1	850	State 6	900
YZAO-25	State 2	900	State 5	875
YZAO-26	State 2	900	State 6	900
YZAO-36	State 3	950	State 6	900

Table 5.1: Initial (pre-DSC) and final (post-DSC) states for the six ZAO and six YZAO samples in the study. The naming convention used follows the template ZAO-*XY* where *X* and *Y* represent the initial and final states in the DSC measurement. Higher SPS temperatures were used for YZAO samples due to limited densification and grain growth compared to ZAO.

For the heat measurement, samples were heated at a constant rate and held at the maximum temperature for 15 minutes to fully develop the grain growth peak. Peak integrations were performed by fitting the background to a Bezier function to estimate the enthalpy of grain growth. This function allows for correction of the change in heat capacity of the sample during coarsening. Example peaks for ZAO-16 and YZAO-16 with subtracted backgrounds are included in **Figure 5.2**:

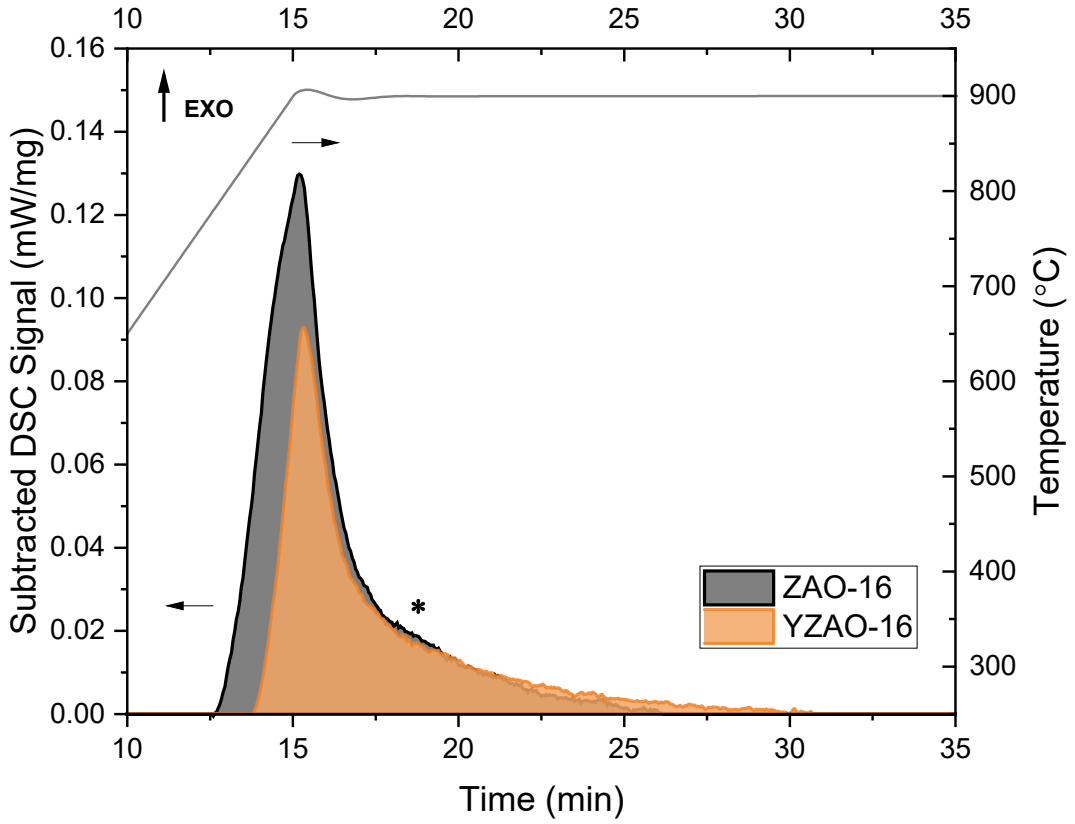

Figure 5.2: Background-subtracted DSC curves for ZAO-16 and YZAO-16 with exothermic signals represented as positive values. Samples were heated to 900°C under an Ar environment and maintained at the final temperature for 15 minutes to allow grain growth peaks to fully develop. Peak integrals indicate lower heats of grain growth in YZAO compared to ZAO. A small shoulder on the ZAO-16 peak is denoted by an asterisk.

Figure 5.2 highlights measurable exothermic heats attributed to grain growth. Heats of grain growth were lower in YZAO samples compared to ZAO samples. This is attributed to both the reduced grain evolution and lower grain boundary energies. This behavior can be taken as a sign of dopant segregation to grain boundaries due to the numerous reports of grain growth inhibition from dopant segregation[50,51,54]. The curves in **Figure 5.2** also indicate a small shoulder in the heat signal past the maximum of the heat effect in the undoped sample; in fact, these shoulders were present in the majority of ZAO and YZAO peaks although sometimes difficult to identify. Such shoulders have been recorded in similar calorimetric studies of the isostructural

magnesium aluminate and were attributed to Al^{3+} inversion from octahedral to tetrahedral sites[181]. Due to the structural similarities, it is presumed that the shoulders observed in DSC peaks for zinc aluminate also represent some degree of inversion. Unlike magnesium aluminate, these heat effects are relatively small and are estimated to account for under 3% of the total are of the peak. This is because site inversion is limited in zinc aluminate compared to magnesium aluminate due to the crystal field stabilization energy of the Zn^{2+} ion[182]. Therefore, contributions from this phenomenon to the heats of grain growth were assumed to be negligible.

In order to quantify the microstructural evolution attributed to each individual heat effect, samples were analyzed using XRD to perform phase analysis and calculate crystallite sizes. **Figure 5.3** includes XRD patterns for two sintered samples (ZAO-16 and YZAO-16) before and after DSC experiments at 900°C, showing each is single phased with grain sizes in the limit of Scherrer's equation. These results represent the behavior observed in all studied samples. Samples that showed second phases at large grain sizes (post-DSC) were discarded from this study as second phase formation would introduce additional heat effects to the peak that could not be easily deconvoluted.

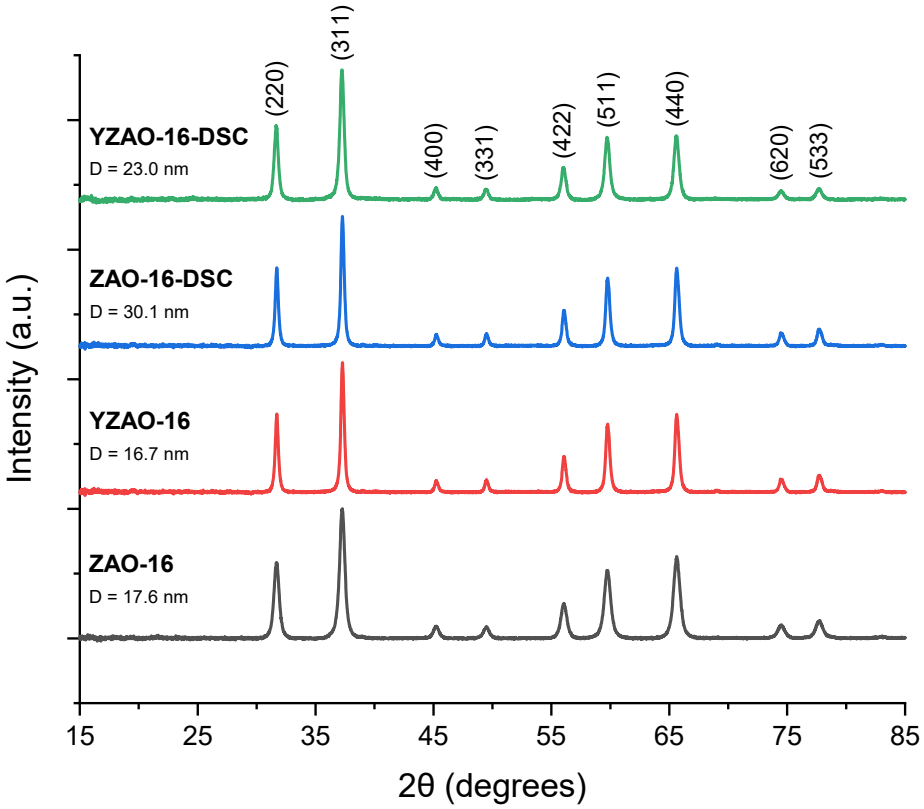

Figure 5.3: XRD patterns of ZAO-16 and YZAO-16 before (black and red) and after (blue and green) grain growth at 900°C in a DSC. Upon heating to 900°C, ZAO and YZAO grains grow by approximately 13 and 6 nm, respectively. The spinel phase was the only one detected in both samples before and after DSC experiments.

Measured crystallite sizes and heats of sintering are summarized in **Table 5.2** for each ZAO and YZAO sample in the study.

Sample	Grain Size (nm)		Grain Boundary Area (m^2/g)		ΔH (J/g)
	Initial D_0	Final D_f	Initial $A_{gb,0}$	Final $A_{gb,f}$	
ZAO-14	17.1	25.3	45.4	30.6	24.56
ZAO-15	17.1	27.3	45.4	28.4	29.16
ZAO-16	17.6	30.1	44.0	25.8	23.18
ZAO-25	21.4	28.4	36.2	27.3	11.18
ZAO-26	20.4	30.3	38.1	25.6	18.28
ZAO-36	28.4	32.6	27.3	23.8	5.29
YZAO-14	17.1	21.2	45.4	36.6	7.68
YZAO-15	17.0	22.5	45.8	34.4	12.58
YZAO-16	16.7	23.0	46.5	33.7	15.50
YZAO-25	22.6	24.4	34.3	31.8	1.41
YZAO-26	21.1	25.7	36.7	30.1	6.46
YZAO-36	28.1	29.3	27.6	26.5	0.03

Table 5.2: Grain sizes, grain boundary areas, and enthalpies of grain growth for each ZAO and YZAO sample in the study. The naming convention is representative of the initial and final states as described in **Table 5.1**. Enthalpies were calculated by integrating DSC peaks using a Bezier function to fit the background.

Grain sizes and enthalpies of grain growth from **Table 5.2** support the idea that Y-doped samples undergo less grain growth than undoped samples likely due to grain boundary stabilization from segregated dopants[50,51,54]. The values were averaged across each state and used in a system of equations based on **Equation 5.4** to calculate grain boundary energies for each composition. The calculated grain boundary energies are plotted as functions of grain size in **Figure 5.4**:

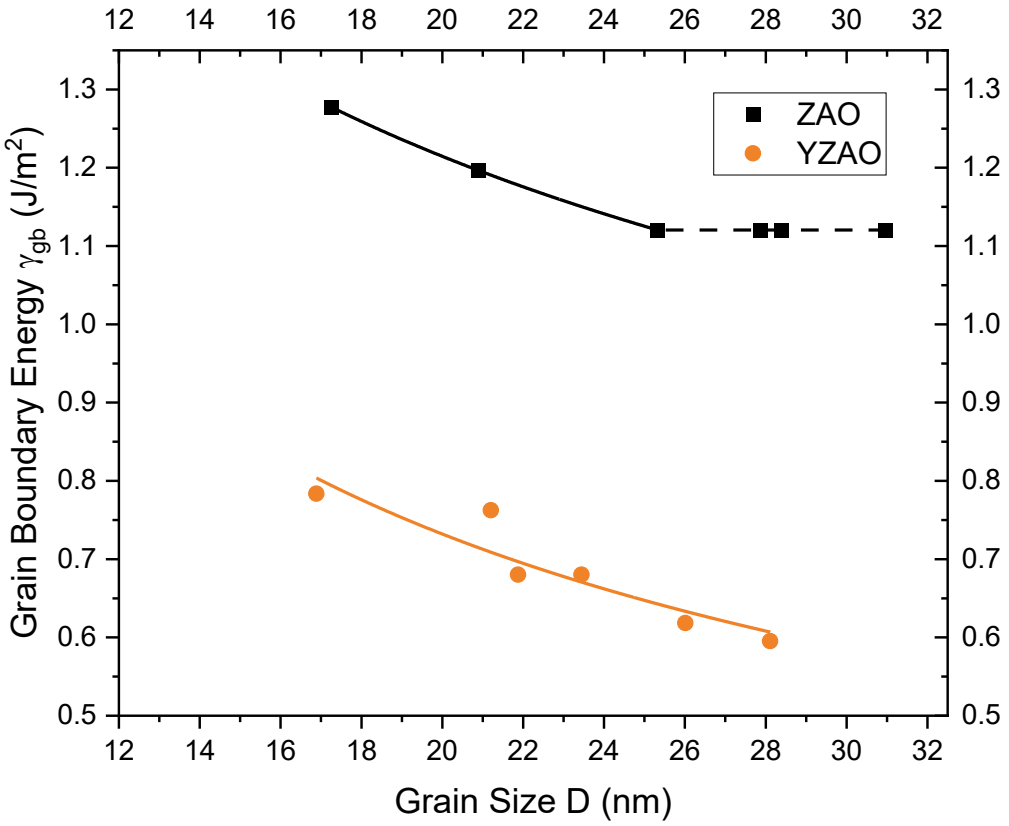

Figure 5.4: Grain boundary energies plotted as functions of grain size for ZAO and YZAO. Exponential fits were calculated and plotted with solid lines for each set of data to highlight the grain size dependence of grain boundary energies. Lower energies are calculated at each grain size for doped samples, which aligns with the consistently low heats of grain growth in **Table 5.2**.

Grain boundary energies measured for YZAO are approximately 38-46% lower than those for ZAO: energies range from 1.1 to 1.3 J/m^2 for ZAO and 0.6 to 0.8 J/m^2 for YZAO. Yang et al. reported grain boundary energies of 0.47 J/m^2 for quasi-stoichiometric zinc aluminate which are significantly lower than those measured here[118]. The discrepancy with the literature is attributed to three possible reasons: (1) differences in sample densities, (2) difference in grain boundary character, or (3) variations in Al:Zn stoichiometric ratios at grain boundaries. The first explanation relates to the fact that measurements in this study were performed on fully dense samples, unlike Yang et al.'s work which focused on green bodies utilizing the heat of sintering. The dense initial

states in our study led us to assume that changes in surface areas during DSC experiments were negligible, while Yang et al. had to account for this in their calculations. Accounting for reduction in surface area during DSC measurements can result in artificially low grain boundary energies if surface area calculations are inaccurate, which may be the case for zinc aluminate if carbonates are adsorbed on powder surfaces[154,155]. Secondly, it is expected that samples prepared by high-pressure spark plasma sintering would have more random orientations of grain boundaries. This is because of the rate of sintering which fundamentally forges grain boundaries with greater excess energy compared to those formed by slower pressure-less sintering. Aside from this, Yang et al. found that Al-rich (Al:Zn = 2.4) zinc aluminate had higher grain boundary energies of 0.70 J/m^2 than quasi-stoichiometric (Al:Zn = 2.1) samples[118]. ZAO in this study had a stoichiometric ratio of 2.16 which is slightly higher.

The measured reduction in grain boundary energies of roughly 40% in zinc aluminate aligns with previous results for Y-doped magnesium aluminate and La-doped yttria-stabilized zirconia where grain boundary energies were reduced by up to 40% and 44%, respectively[50,64]. However, when taking into consideration the relatively low dopant concentration (0.5 mol% Y_2O_3), the individual effect of Y^{3+} doping in zinc aluminate stands out substantially. For comparison, the reductions in magnesium aluminate and yttria-stabilized zirconia were for dopant concentrations of 3 mol% Y_2O_3 and 1.5 mol% La_2O_3, respectively. This remarkable lowering of grain boundary energies is possibly related to the cooperative self-segregation of excess Al^{3+} to interfaces, which has been reported in the past for magnesium aluminate[95,96]. Al enrichment was evident at the surfaces of zinc aluminate nanoparticles (**Figure 4.8**), but more EELS scans must be taken on dense samples to confirm that this is also the case for grain boundaries.

Figure 5.4 also indicates a grain size dependence of the grain boundary energy for both ZAO and YZAO. For undoped oxides, this is usually attributed to a change in the grain boundary population since grain growth quickly eliminates grain boundaries with higher energies, lowering the average grain boundary energy of the system[45]. ZAO grain boundary energies plateau around grain sizes of 20-28 nm, which is consistent with the fact that this phenomenon becomes marginal as grain boundaries approach their equilibrium configurations

Decreasing grain boundary energies as a function of grain sizes in doped samples are instead a result of decreasing grain boundary area or increasing grain boundary excess as described by the Gibbs adsorption isotherm[65,92]. To highlight this, grain boundary areas were calculated as a

function of grain size for zinc aluminate using **Equation 5.5**. These are plotted along with YZAO grain boundary energies in **Figure 5.5**:

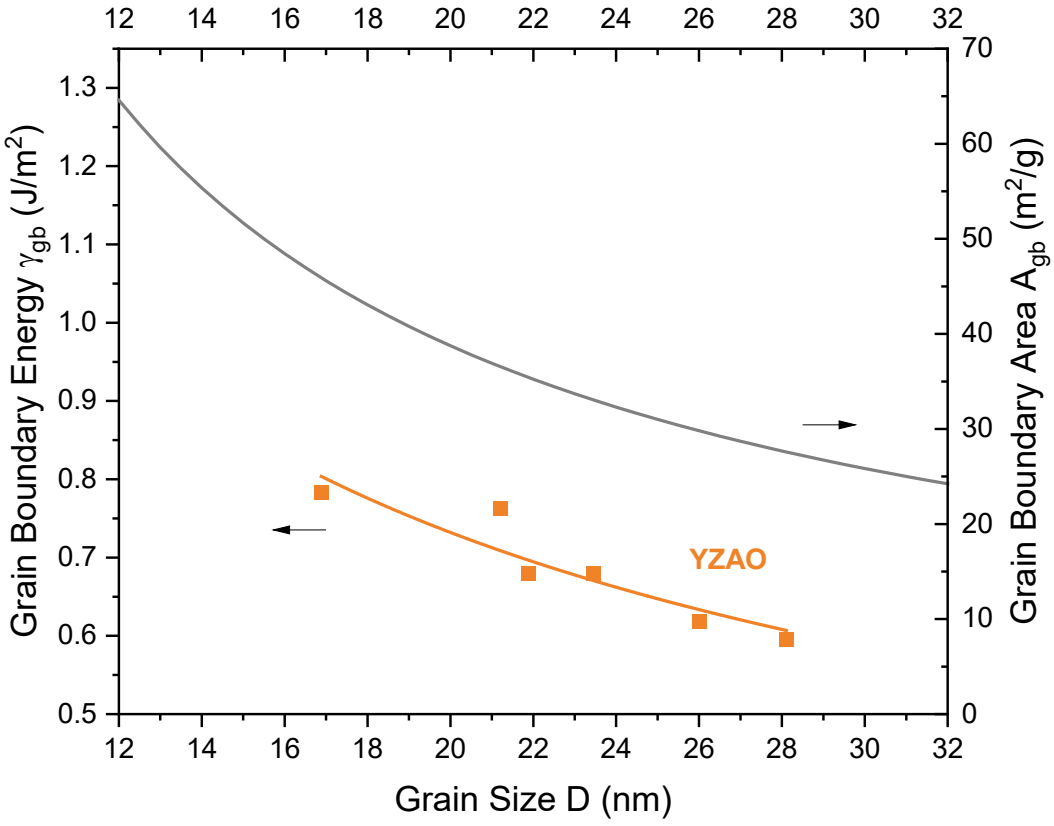

Figure 5.5: Grain boundary energies for YZAO plotted with an exponential fit (solid line) along with grain boundary areas plotted as functions of grain size. Grain boundary areas were calculated using **Equation 5.5** for tetrakaidecahedron grains and grain boundary thicknesses of 1 nm. The similar slopes between grain boundary energies and grain boundary areas suggest there is a correlation between the two as predicted for dopant segregation.

Figure 5.5 shows good correlation exists between grain boundary area and grain boundary energies for Y-doped zinc aluminate (with ZAO having a lower slope). The Gibbs adsorption isotherm predicts that, at constant dopant concentrations, decreases in grain boundary area result in further enrichment of grain boundaries and a consequent reduction of excess energy. Eventually, the grain boundary energies will plateau when grain boundaries are saturated with dopants, as observed by Muche et al. in La-doped magnesium aluminate[55] and Nafsin et al. in Gd-doped yttria-

stabilized zirconia[52]. The fact that grain boundary energies continue decreasing at 28 nm indicates that doped grain boundaries are not fully saturated with dopants.

5.4: Conclusions

Grain boundary stability of nanocrystalline zinc aluminate was investigated using molecular dynamics and calorimetric techniques to evaluate the segregation behavior of four dopants: Sc^{3+}, In^{3+}, Y^{3+}, and Nd^{3+}. Molecular dynamics simulations estimated that Y^{3+} has the highest propensity for segregating to zinc aluminate grain boundaries. Despite the simplified defect chemistry in simulations, the method was able to successfully predict Y^{3+} segregation to zinc aluminate grain boundaries. Further experimental studies are needed to analyze the effects of Y^{3+} on space charge layers and to confirm the potential anisotropic segregation predicted by simulations.

High-pressure spark plasma sintering allowed the fabrication of dense nanocrystalline Y-doped and undoped zinc aluminate. Y-doped samples generally had smaller grain sizes than their undoped counterparts which was consistent with coarsening inhibition observed in differential scanning calorimetry studies. Calorimetric experiments showed a reduction in average grain boundary energies for zinc aluminate doped with 0.5 mol% Y_2O_3 at each grain size in the study, which is consistent with dopant segregation as predicted by the simulation work. Grain boundary energy was estimated to be a function of grain size for both doped and undoped zinc aluminate with Y-doped samples having a stronger dependence due to the effects of grain boundary area reduction on the dopant concentration at the grain boundaries. Combining the results from this study with previous reports of grain boundary stabilization in nanomaterials, it is expected that doping zinc aluminate grain boundaries with Y^{3+} will also result in increases in hardness and fracture toughness. This result will be used in future work to tailor mechanical behavior in zinc aluminate to prove its viability as a material for next-generation armored windows.

Chapter 6: Mechanical Performance of Y-Doped Nanocrystalline Zinc Aluminate

Abstract

Nanocrystalline zinc aluminate has been highly touted as a potential armor ceramic due to its mechanical, thermal, and optical properties. The hardness and fracture toughness of undoped zinc aluminate and zinc aluminate doped with 0.5 mol% Y_2O_3 were measured by means of indentations to expand on previous work that demonstrated enhanced grain boundary stabilities in doped samples. It was found that both compositions had similar Vickers hardness values at grain sizes below 25 nm (approximately 18.1 GPa) while Y-doped samples had superior hardness at grain sizes higher than this point. Fracture toughness values were also in the same range for doped and undoped samples (2.9-3.5 $MPa \cdot m^{0.5}$) with values decreasing as a function of grain size. Overall, these results represent the first reported fracture toughness values for nanocrystalline zinc aluminate where values are similar to those reported for nanocrystalline magnesium aluminate. This work additionally highlights the role of dopant concentration in controlling mechanical properties despite previous reports of significantly enhanced grain boundary stabilities in zinc aluminate with same Y^{3+} concentration.

6.1: Introduction

Researchers have demonstrated that nanocrystalline zinc aluminate ($ZnAl_2O_4$) can exhibit optical transparency and hardness close to that of aluminum oxynitride (ALON) and sapphire[26,152,183,184] while displaying higher thermal conductivity[185], making it a candidate material for the next generation of armored windows. Although stoichiometric zinc aluminate has repeatedly registered hardness values near 20 GPa at the nanoscale, the grain size dependence of this value remains difficult to predict[26,152].

One study by Yang et al. looked to analyze the grain size hardening behavior of spark plasma sintered zinc aluminate to compare with previous results on other nanocrystalline oxides[26]. This study reported increasing hardness values in zinc aluminate down to grain sizes close to 10 nm; however, small-grained samples were found to have extensive networks of cracks compared to their larger-grained counterparts[26]. The observed cracking behavior foreshadowed a reversal in this trend at smaller grain sizes which was eventually confirmed by a separate study that recorded

a decrease in hardness at grain sizes below 20 nm for stoichiometric zinc aluminate[152]. This recent study also implied that the grain size hardening behavior in zinc aluminate may be directly related to the stability of its grain boundaries: Al-rich zinc aluminate showed elevated hardness at small grain sizes which was presumed to be due to interfacial segregation[152]. Similar conclusions had been reached before by Hu et al. who found a correlation between grain boundary stability and hardness in Ni-Mo alloys[110] as well as Bokov et al. who showed a breakdown in grain size hardening coincident with an increase in average grain boundary energies in yttria-stabilized zirconia[70].

Y^{3+} has been shown to segregate to zinc aluminate grain boundaries and significantly improve their stability (**Figure 5.4**) which, combined with results from other materials, would predict superior hardness for Y-doped zinc aluminate. This work aims to substantiate this claim by comparing the hardness of undoped zinc aluminate to that of zinc aluminate doped with 0.5 mol% Y_2O_3. A separate goal of this study will focus on analyzing the effects of Y^{3+} segregation on zinc aluminate fracture toughness to complement results from Bokov et al. that measured elevated fracture toughness in La-doped yttria-stabilized zirconia[64]. By investigating this, we also seek to enrich the set of literature data for fracture toughness of nanocrystalline oxides which, in its current state, is narrow. These results will have implications on the design of nanostructured ceramics for the development of next-generation armored windows.

6.2: Experimental Procedures

6.2.1: Synthesis and nanopowder characterization

Undoped zinc aluminate (ZAO) powder was synthesized using reverse-strike co-precipitation where an aqueous metal nitrate solution [$Zn(NO_3)_2 \cdot 6H_2O$ and $Al(NO_3)_3 \cdot 9H_2O$ (Sigma Aldrich, >98%)] was mixed dropwise with a 2 mol/L aqueous ammonia solution[26,118,150,151]. Before synthesis, water contents of each nitrate precursor were measured to ensure stoichiometric ratios were maintained. Additionally, the synthesis was carried out under a constant pH of 8.75 to prevent the formation of $Zn(NH_3)_4^{2+}$ to preserve the initial stoichiometry[26,118,150,151]. Y-doped zinc aluminate (YZAO) was also synthesized by this method, but $Y(NO_3)_3 \cdot 6H_2O$ (Sigma Aldrich, >98%) was dissolved in the nitrate precursor solution in this case to give a concentration of 0.5 mol% Y_2O_3. Both sets of powder were ground from dried precipitates before calcining in a Thermo Scientific Lindberg/Blue M (Thermo Fisher Scientific

Inc., Waltham, MA) box furnace at 550°C for 4 hours to induce a transition into the spinel phase with limited coarsening[26,118,152].

Phase and crystallite size analysis was performed on both powders by examining x-ray diffraction (XRD) patterns taken on a Bruker D8 (Bruker, Billerica, MA) operated at 40 kV, 40 mA (CuKα radiation, λ=1.5406 Å). Crystallite sizes were calculated on Match! (Crystal Impact, Bonn, Germany) software using reference pattern #96-900-7021 (Levy et al.[153]). These measurements were validated by images captured using scanning transmission electron microscopy (STEM) on a JEOL-ARM300F Grand ARM (JEOL, Peabody, MA).

The stoichiometric ratios of Al:Zn were measured for each set of powders using electron microprobe analysis (EMPA) on a Cameca SX-100 (Cameca, Gennevulliers, France) since studies have shown this correlates with mechanical and sintering behaviors in spinels[34,95,96,152]. Measurements were averaged over 10 scans taken across each sample and showed that the ratios were similar for both powders: 2.16 (±0.14) and 2.11 (±0.06) for ZAO and YZAO, respectively.

6.2.2: Spark plasma sintering

Calcined powders were degassed in a Micromeritics SmartVacPrep (Micromeritics Instrument Corp., Norcross, GA) at 400°C for a minimum of 16 hours to remove water adsorbed on surfaces. Dry powders were stored in a dry nitrogen atmosphere (under 0.6% relative humidity) in a glovebox until being sintered.

High-pressure spark plasma sintering (HP-SPS) was used to sinter samples in this study[27,64,70,93]. The setup consisted of two concentric dies with an inner die (inner diameter (ID): 4 mm, outer diameter (OD): 19 mm) made of a diamond/SiC composite (Hyperion Materials & Technologies, Deerfield Beach, FL)[27,64,70,93]. Punches made from the same composite were placed in the inner die on either side of the green body. This setup was inside of a larger graphite die (ID: 19 mm, OD: 45 mm) to insulate the inner die and maintain a current path in the SPS.

An SPS model 825S (Syntex Inc., Kawasaki, Japan) was used to sinter each sample at temperatures of 800-900°C and pressures of 1.2-2.0 GPa to achieve full density. Each pellet was annealed at 150°C below its maximum sintering temperature to remove residual strain and oxidize any carbon and elements reduced during the sintering process.

6.2.3: Pellet characterization

Upon annealing, each sintered pellet was polished flat with 800 grit sandpaper. Relative densities were measured for each sample using an Archimedes' balance while assuming a theoretical density of 4.58 g/cm^3 since Rietveld refinement estimated similar lattice parameters for doped and undoped samples[177]. All samples were optically transparent with relative densities greater than 98%. XRD analysis confirmed that each pellet was single phased with grain sizes under 30 nm.

6.2.4: Mechanical testing

Each pellet was polished with diamond paste to micron sizes of 0.1 μm to minimize curvature and scratches on surfaces before indenting. A Mitutoyo HM-220A (Mitutoyo Corporation, Sakado, Japan) microindenter with a Vickers pyramid was used to indent each sample at a constant load of 40 gf. The load was chosen to limit spallation since studies have shown this can result in artificially low hardness measurements[33]. Reports show that indentation loads have negligible effects on Vickers hardness measurements in zinc aluminate[26]. Indentations were imaged using scanning electron microscopy (SEM) with a Thermo Scientific Scios DualBeam SEM/FIB (Thermo Fisher Scientific Inc., Waltham, MA) using an accelerating voltage of 5 kV and a beam current of 0.1 nA. The dimensions of each indentation were estimated using ImageJ software.

Around 60 indentations were used to estimate hardness and fracture toughness as a function of grain size for each composition: about 30 per composition and 10 for each grain size. Fracture toughness was calculated using the same method as Bokov et al. to maintain a reference for measurements in this study[64]. This method involved averaging the fracture toughness from three equations developed by Lankford[186], Laugier[187], and Shetty et al.[188].

6.3: Results and Discussion

Vickers hardness was measured for three samples average grain sizes between 15 and 30 nm for doped and undoped zinc aluminate. Results plotted in the form of the Hall-Petch equation are included in **Figure 6.1** below:

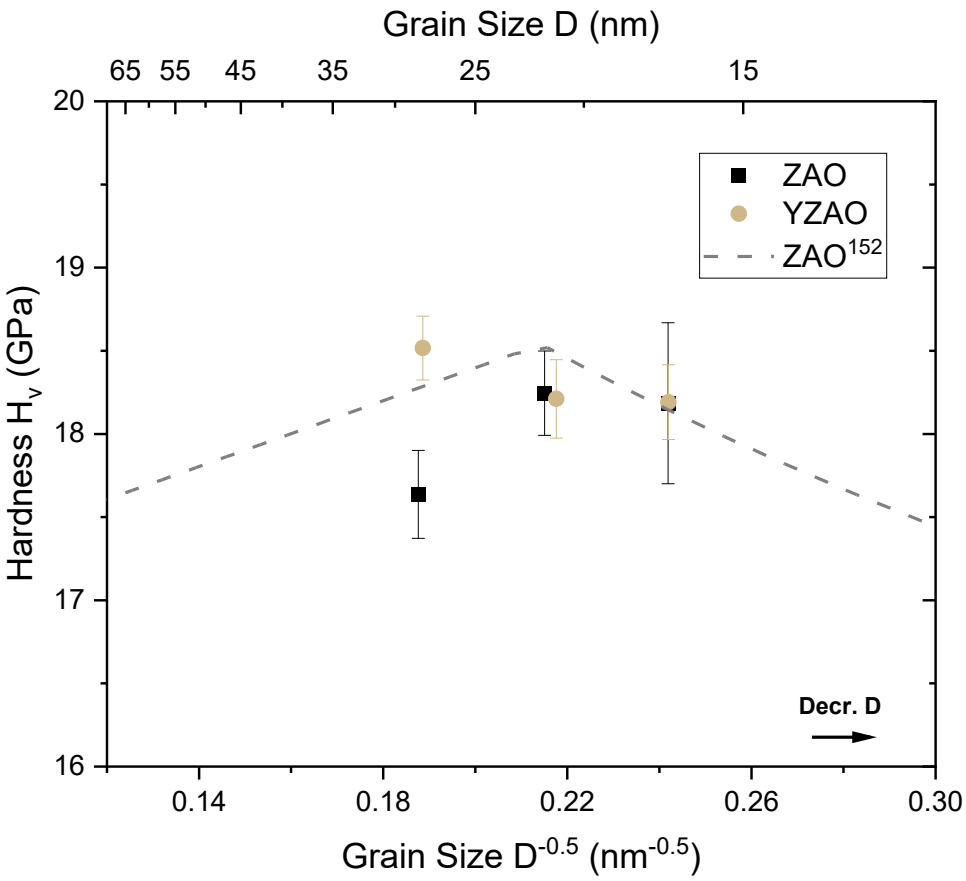

Figure 6.1: Vickers hardness plotted as a function of the inverse square root of grain size (grain size decreasing to the right) for ZAO and YZAO. Dashed line represents previous data for stoichiometric (Al:Zn = 2.01:1) zinc aluminate[152]. Error bars represent 95% confidence intervals around the mean hardness values.

Calculated hardness values range between 17.5 and 18.5 GPa, which agrees well with data reported for stoichiometric (Al:Zn ratio of 2.01:1) zinc aluminate that predicts an inversion in the grain size hardening behavior around 20 nm[152]. Additionally, doped and undoped samples with grain sizes below 25 nm were found to have statistically similar hardness values, suggesting that Y^{3+} has a negligible impact on zinc aluminate hardness at these grain sizes. The data in **Figure 6.1** goes against the initial hypothesis that Y^{3+} grain boundary segregation elevates hardness in doped samples.

The negligible effect of Y^{3+} on hardness at low grain sizes could be a result of (1) limited grain boundary excess at small grain sizes or improved hardness convoluted by (2) nanopores at

triple junctions[45,189,190] or (3) a second phase undetectable by XRD[50]. If present in the system, nanopores and second phases could serve to concentrate the stress applied by the indenter, which would lead to lower observed hardness values. Transmission electron microscopy images would need to be collected for doped samples to rule out the effects of nanopores and second phases, which are not included here. Nonetheless, this behavior is more likely a result of the low dopant concentrations used in this study. Other studies on doped nanoceramics featured dopant concentrations of at least 1 mol% (e.g., 1 mol% X_2O_3)[50,54,55,98], while YZAO in the present study contained only 0.5 mol% Y_2O_3. If this is in fact the reason for the similar hardness values, there may still be an evident difference in the cracking behavior for YZAO samples. Previous work on zinc aluminate has shown that Al-rich samples undergo significantly less lateral cracking than stoichiometric samples, even in samples with similar hardness values[152]. Similar behavior may be observed in YZAO samples as a result of dopant segregation, which makes this an intriguing subject for future work.

By examining data in **Figure 6.1** above 25 nm, it is apparent that YZAO has significantly higher hardness values than ZAO at grain sizes near 28 nm: ZAO registered a hardness of 17.6 (±0.3) GPa while YZAO had a hardness of 18.5 (±0.3) GPa. At these grain sizes, it is presumed that sample hardness is defined by a mix of dislocation pinning and grain boundary deformation as cited in previous studies[13,124,152]. This result could then be explained by two reasons: (1) reduced grain boundary deformation in YZAO samples or (2) enhanced dislocation pinning in YZAO samples. Although results at small grain sizes imply that Y^{3+} concentrations at grain boundaries are too low to impact hardness values, the grain boundary excess is expected to increase with decreasing grain boundary area (i.e., increasing grain size). This increase in dopant concentration at grain boundaries could increase the activation energy for grain boundary shearing, leading to higher hardness[124,152]. The other possibility is that Y^{3+} segregates to charged dislocation cores and serves as a pinning agent which has been reported for doped semiconductors[191]. Improved hardness would become more obvious at higher dopant concentrations, which will be addressed in future work.

Fracture toughness was measured on the same set of samples to complement the discussion on zinc aluminate mechanical properties. The results are shown in the figure below:

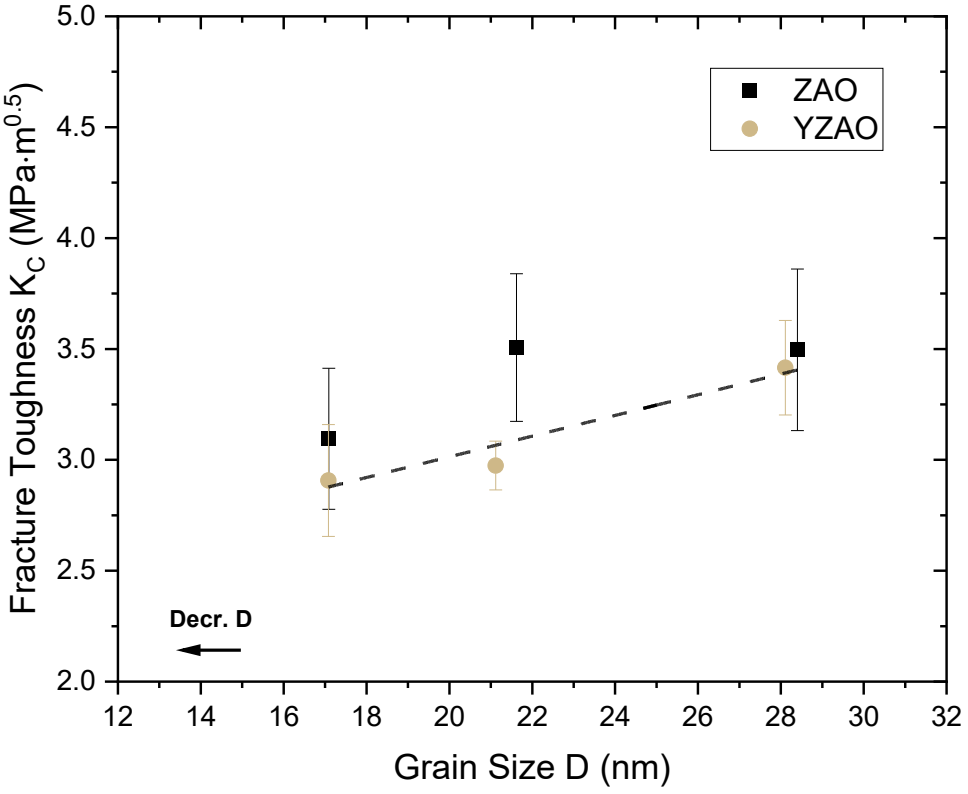

Figure 6.2: Indentation fracture toughness ($\boldsymbol{K_C}$) plotted as a function of grain size (grain size decreasing to the left) for ZAO and YZAO. Data is plotted along with a linear fit across solely for visual purposes. Error bars represent 95% confidence intervals around the mean fracture toughness.

Figure 6.2 shows that mean toughness values lie between 2.5 and 3.5 MPa·m$^{0.5}$ with a clear grain size dependence for both ZAO and YZAO. These values are comparable to those measured for nanocrystalline yttria-stabilized zirconia and magnesium aluminate using a similar technique, which led to values around 1.7 and 3.6 MPa·m$^{0.5}$, respectively[35,64]. Similar to findings for hardness, this data shows that Y-doped samples had toughness values within error of the undoped values. This result is consistent with the idea that the dopant concentration in this study is too low to impact macroscopic mechanical properties.

Previous work indicates that zinc aluminate undergoes a transition from transgranular to intergranular cracking with decreasing grain size[26]. Materials that undergo primarily intergranular cracking will naturally exhibit lower toughness with decreasing grain size due to the increased population of high-energy grain boundaries[64,81,192]. This explains the decrease in fracture toughness with grain size found in both samples and indicates that higher concentrations of Y^{3+} may limit this reduction in toughness by stabilizing the energetic landscape and improving the crack branching behavior as with La^{3+} in yttria-stabilized zirconia[64].

6.4: Conclusions

The present work reports hardness and toughness values measured by means of indentations for undoped and Y-doped (0.5 mol% Y_2O_3) zinc aluminate. Vickers hardness values were around 17.6-18.5 GPa for both samples, indicating that Y^{3+} segregation to grain boundaries has a minimal effect on hardness for the concentration used in this study. However, hardness in doped samples before the Hall-Petch inversion (near 28 nm) was statistically higher than in undoped samples. This implies that either (1) the low grain boundary area in larger-grained samples led to sufficiently high Y-excess at grain boundaries which raised the activation energy for grain boundary deformation mechanisms or (2) Y^{3+} segregated to dislocations and enhanced dislocation pinning in zinc aluminate. Microscopy on indentation cross-sections is needed to reveal the true behavior.

Zinc aluminate fracture toughness values were also measured for the first time in this study where values ranged between 2.9 and 3.5 $MPa \cdot m^{0.5}$ for both sets of samples. A similar conclusion was reached here, that doped samples had similar toughness values to their undoped counterparts potentially due to low dopant concentrations at grain boundaries. Fracture toughness was found to decrease with decreasing grain sizes in both zinc aluminate compositions. Due to previous reports of transgranular cracking at low grain sizes in zinc aluminate, this grain size dependence of fracture toughness is presumably related to the elevated population of high-energy grain boundaries with decreasing grain size. This work suggests that higher dopant concentrations are needed to impact mechanical properties which will be the subject of future work.

Chapter 7: Conclusions and Future Work

7.1: Conclusions

This work focused on analyzing the thermal stability and mechanical performance of nanocrystalline zinc aluminate ($ZnAl_2O_4$) through the lens of interfacial thermochemistry. The stabilities of zinc aluminate surfaces and grain boundaries were tuned using dopant segregation, a technique proven to lower interfacial energetics in other nanocrystalline oxides. Molecular dynamics simulations on a nanoparticle and two grain boundary structures were used to screen four potential dopants for their propensity to segregate to zinc aluminate interfaces. Y^{3+} was found to have the highest segregation energies to both types of interfaces despite having the second highest ionic radius; therefore, this was chosen as the dopant for all experimental work. Undoped zinc aluminate was synthesized along with zinc aluminate doped with 0.5 mol% Y_2O_3 to experimentally measure grain boundary and surface energies. Water adsorption microcalorimetry was used to estimate surface energies of doped and undoped nanopowders, where doped powders had lower grain boundary energies around 0.85 J/m^2. Doped powder was also found to have lower self-diffusion coefficients which, together, led to improved coarsening behavior compared to undoped zinc aluminate. Grain boundary energies were measured as a function of grain size using differential scanning calorimetry experiments on sintered samples. Similar to surface energies, lower grain boundary energies were estimated at each grain size for Y-doped zinc aluminate. This behavior was found to result in limited grain growth for doped samples, potentially due to favorable thermodynamics and kinetics.

Previous work on doped nanocrystalline oxides led us to predict that lower grain boundary energies could lead to elevated mechanical properties (e.g., hardness and fracture toughness) in zinc aluminate. To test this idea, pellets were sintered from doped and undoped powders to measure hardness and fracture toughness from indentations. Measured hardness and toughness values were similar regardless of the composition which we believe to be due to the low dopant concentration (0.5 mol% Y_2O_3) used in this work. This idea is supported by the fact that higher hardness was measured in larger-grained samples: these samples contain lower grain boundary area which would result in higher dopant concentrations at each grain boundary. The improved hardness was assumed to be a result of either enhanced dislocation pinning from Y^{3+} segregation to dislocations or delayed activation of grain boundary mediated deformation (e.g., shearing and rotation. This study also found that fracture toughness decreased with decreasing grain size in both

doped and undoped samples. This behavior is likely due to the greater population of high-energy grain boundaries found in small-grained samples which facilitate crack propagation. A separate study focused on the grain size hardening behavior of zinc aluminate with varying concentrations of Al. This study found that Al-rich samples (Al:Zn = 2.87:1) exhibited extended grain size hardening compared to stoichiometric samples (Al:Zn = 2.01:1). Al-rich samples were found to have a limited number of lateral vents compared to stoichiometric samples; these types of cracks are indicative of extensive grain boundary deformation. This led to the conclusion that excess Al was primarily located at zinc aluminate grain boundaries which led to enhanced stability and postponed grain boundary deformation in these samples.

This work provides some insight into the mechanical and thermal behavior of nanocrystalline zinc aluminate which can be applied to most nanocrystalline oxides. Conclusions from these studies bring us closer to designing the next generation of armored windows, laser gain media, and catalysts made from nanocrystalline ceramics.

7.2: Future Work

Future work on nanocrystalline zinc aluminate will primarily focus on its mechanical behavior since there is still a dearth of understanding surrounding the dominant deformation mechanisms in the undoped and doped/Al-rich states. Sub-surface cracks were analyzed for Al-rich samples, but it is still unclear whether doping with Y^{3+} has a similar effect on grain boundary deformation as Al enrichment. Additionally, the present work did not succeed in analyzing the effects of Y^{3+} on the grain size hardening behavior at small grain sizes. This was due to difficulties associated with sintering zinc aluminate to full density at low enough temperatures to limit grain growth. More efforts will be made on this end, potentially using sintering aids or higher pressures to ensure small-grained samples were fully dense. Follow-up work will also employ higher concentrations of Y^{3+} to analyze its effects on zinc aluminate hardness and toughness at the nanoscale.

Another focus of future work will be on Al-rich zinc aluminate, particularly looking at its grain boundary energies and fracture toughness. Samples rich in Al showed signs of improved grain boundary energies, but this was unfortunately not investigated here. If grain boundary energies are indeed improved in Al-rich samples, it is possible that these samples may exhibit higher toughness and/or a limited grain size dependence of fracture toughness.

To enhance our fundamental understanding of dopant segregation to individual interfaces, it would be interesting to conduct a more systematic molecular dynamics study on zinc aluminate that spans more dopants and different types of interfaces. This would reveal whether Y^{3+} segregation to zinc aluminate grain boundaries becomes unfavorable with higher misorientation angles and would provide useful insights on the dependence of segregation energy on dopant ionic radius as well as charge. These results could be applied experimentally to co-dope zinc aluminate with several dopants at a time to further stabilize its coarsening behavior and enhance mechanical properties.

References

1. Suryanarayana C. Nanocrystalline materials. *Int Mater Rev*. 1995;40(2):41-63. doi:10.1179/imr.1995.40.2.41

2. Koch CC. Structural nanocrystalline materials: An overview. *J Mater Sci*. 2007;42(5):1403-1414. doi:10.1007/s10853-006-0609-3

3. Meyers MA, Mishra A, Benson DJ. Mechanical properties of nanocrystalline materials. *Prog Mater Sci*. 2006;51(4):427-556. doi:10.1016/j.pmatsci.2005.08.003

4. Patsalas P, Logothetidis S, Metaxa C. Optical performance of nanocrystalline transparent ceria films. *Appl Phys Lett*. 2002;81(3):466-468. doi:10.1063/1.1494458

5. Pradhan N, Das Adhikari S, Nag A, Sarma DD. Luminescence, Plasmonic, and Magnetic Properties of Doped Semiconductor Nanocrystals. *Angew Chemie - Int Ed*. 2017;56(25):7038-7054. doi:10.1002/anie.201611526

6. Vitta S, Khuntia A, Ravikumar G, Bahadur D. Electrical and magnetic properties of nanocrystalline Fe100-xNix alloys. *J Magn Magn Mater*. 2008;320(3-4):182-189. doi:10.1016/j.jmmm.2007.05.021

7. Dong H, Wen B, Melnik R. Relative importance of grain boundaries and size effects in thermal conductivity of nanocrystalline materials. *Sci Rep*. 2014;4:7037. doi:10.1038/srep07037

8. Birringer R. Nanocrystalline Materials : Mechanical. *Mater Sci Eng A*. 1995;117:33-43.

9. Anaya J, Rossi S, Alomari M, et al. Control of the in-plane thermal conductivity of ultra-thin nanocrystalline diamond films through the grain and grain boundary properties. *Acta Mater*. 2016;103:141-152. doi:10.1016/j.actamat.2015.09.045

10. Schuh CA, Lu K. Stability of nanocrystalline metals: The role of grain-boundary chemistry and structure. *MRS Bull*. 2021;46(3):225-235. doi:10.1557/s43577-021-00055-x

11. Van Swygenhoven H, Derlet PM. Grain-boundary sliding in nanocrystalline fcc metals. *Phys Rev B - Condens Matter Mater Phys*. 2001;64(22):1-9. doi:10.1103/PhysRevB.64.224105

12. Shan Z, Stach EA, Wiezorek JMK, Knapp JA, Follstaedt DM, Mao SX. Grain Boundary – Mediated Plasticity in Nanocrystalline Nickel. *Science (80-)*. 2004;305(July):654-658.

13. Ratzker B, Wagner A, Sokol M, Meshi L, Kalabukhov S, Frage N. Deformation in nanocrystalline ceramics: A microstructural study of MgAl2O4. *Acta Mater*. 2020;183:137-144. doi:10.1016/j.actamat.2019.11.015

14. Yamashita I, Tsukuma K. Light scattering by residual pores in transparent zirconia ceramics. *J Ceram Soc Japan*. 2011;119(1386):133-135. doi:10.2109/jcersj2.119.133

15. Benitez T, Y. Gómez S, de Oliveira APN, Travitzky N, Hotza D. Transparent ceramic and glass-ceramic materials for armor applications. *Ceram Int*. 2017;43(16):13031-13046. doi:10.1016/j.ceramint.2017.07.205

16. Palmero P, Bonelli B, Fantozzi G, et al. Surface and mechanical properties of transparent polycrystalline YAG fabricated by SPS. *Mater Res Bull*. 2013;48(7):2589-2597. doi:10.1016/j.materresbull.2013.03.003

17. Ghosh S, Teweldebrhan D, Morales JR, Garay JE, Balandin AA. Thermal properties of the optically transparent pore-free nanostructured yttria-stabilized zirconia. *J Appl Phys*. 2009;106(11). doi:10.1063/1.3264613

18. Fu P, Wang ZY, Lin ZD, Liu YQ, Roy VAL. The microwave dielectric properties of transparent ZnAl2O4 ceramics fabricated by spark plasma sintering. *J Mater Sci Mater Electron*. 2017;28(13):9589-9595. doi:10.1007/s10854-017-6707-y

19. Goldstein A, Yeshurun Y, Vulfson M, Kravits H. Fabrication of transparent polycrystalline ZnAl 2 O 4 - A new optical bulk ceramic. *J Am Ceram Soc*. 2012;95(3):879-882. doi:10.1111/j.1551-2916.2011.05063.x

20. Tran TB, Hayun S, Navrotsky A, Castro RHR. Transparent nanocrystalline pure and Ca-doped MgO by spark plasma sintering of anhydrous nanoparticles. *J Am Ceram Soc*. 2012;95(4):1185-1188. doi:10.1111/j.1551-2916.2012.05103.x

21. Fedyk R, Hreniak D, Łojkowski W, et al. Method of preparation and structural properties of transparent YAG nanoceramics. *Opt Mater (Amst)*. 2007;29(10):1252-1257. doi:10.1016/j.optmat.2006.05.016

22. Liu K, He D, Wang H, Lu T, Li F, Zhou X. High-pressure sintering mechanism of yttrium aluminum garnet (Y 3Al 5O 12) transparent nanoceramics. *Scr Mater*. 2012;66(6):319-322. doi:10.1016/j.scriptamat.2011.11.012

23. Wang C, Zhao Z. Transparent MgAl2O4 ceramic produced by spark plasma sintering. *Scr Mater*. 2009;61(2):193-196. doi:10.1016/j.scriptamat.2009.03.039

24. Muche DNF, Drazin JW, Mardinly J, Dey S, Castro RHR. Colossal grain boundary strengthening in ultrafine nanocrystalline oxides. *Mater Lett*. 2017;186(October 2016):298-300. doi:10.1016/j.matlet.2016.10.035

25. Zhang HB, Kim BN, Morita K, Yoshida H, Lim JH, Hiraga K. Optimization of high-pressure sintering of transparent zirconia with nano-sized grains. *J Alloys Compd*. 2010;508(1):196-199. doi:10.1016/j.jallcom.2010.08.045

26. Yang C, Thron A, Castro RHR. Grain boundary strengthening in nanocrystalline zinc aluminate. *J Am Ceram Soc*. 2019;102(11):6904-6912. doi:10.1111/jace.16512

27. Sokol M, Halabi M, Mordekovitz Y, Kalabukhov S, Hayun S, Frage N. An inverse Hall-Petch relation in nanocrystalline MgAl2O4 spinel consolidated by high pressure spark plasma sintering (HPSPS). *Scr Mater*. 2017;139:159-161. doi:10.1016/j.scriptamat.2017.06.049

28. Frage N, Kalabukhov S, Sverdlov N, Kasiyan V, Rothman A, Dariel MP. Effect of the spark plasma sintering (SPS) parameters and LiF doping on the mechanical properties and the transparency of polycrystalline Nd-YAG. *Ceram Int*. 2012;38(7):5513-5519. doi:10.1016/j.ceramint.2012.03.066

29. Wollmershauser JA, Feigelson BN, Gorzkowski EP, et al. An extended hardness limit in bulk nanoceramics. *Acta Mater*. 2014;69:9-16. doi:10.1016/j.actamat.2014.01.030

30. Zhou Z, Li W, Song J, Yi G, Mei B, Su L. Synthesis and characterization of Nd3+ doped SrF2 nanoparticles prepared by precipitation method. *Ceram Int*. 2018;44(4):4344-4350. doi:10.1016/j.ceramint.2017.12.028

31. Zhang J, Lu T, Chang X, Wei N, Xu W. Related mechanism of transparency in MgAl2O4 nano-ceramics prepared by sintering under high pressure and low temperature. *J Phys D*

Appl Phys. 2009;42(5). doi:10.1088/0022-3727/42/5/052002

32. Singh R, Khardekar RK, Kumar A, Kohli DK. Preparation and characterization of nanocrystalline Nd-YAG powder. *Mater Lett*. 2007;61(3):921-924. doi:10.1016/j.matlet.2006.06.013

33. Ryou H, Drazin JW, Wahl KJ, et al. Below the Hall-Petch Limit in Nanocrystalline Ceramics. *ACS Nano*. 2018;12(4):3083-3094. doi:10.1021/acsnano.7b07380

34. Muche DNF, Marple MAT, Hung I, Gan Z, Castro RHR, Sen S. Size-Induced Structural Disorder Enables Ultrahard Oxides. *J Phys Chem C*. 2017;121(25):13898-13905. doi:10.1021/acs.jpcc.7b03323

35. Costa ILM, Miagava J, Castro RHR. Sodium as densification aid in MgAl 2 O 4 nanoceramics. *Mater Lett*. 2022;324(June):132693. doi:10.1016/j.matlet.2022.132693

36. Rogers BM, Costa ILM, Zhu W, Sen S, Castro RHR. Sintering, hardness and cation inversion of nanocrystalline Beryllium – Magnesium aluminate ceramics. *Ceram Int*. 2022;48(11):15116-15123. doi:10.1016/j.ceramint.2022.02.041

37. Ikesue A, Aung YL. Ceramic laser materials. *Nat Photonics*. 2008;2(12):721-727. doi:10.1038/nphoton.2008.243

38. Mu S, Chen X, Sun R, et al. Nano-size boron carbide intercalated graphene as high performance catalyst supports and electrodes for PEM fuel cells. *Carbon N Y*. 2016;103:449-456. doi:10.1016/j.carbon.2016.03.044

39. Diaz-Torres LA, Mtz-Enriquez AI, Garcia CR, et al. Efficient hydrogen generation by ZnAl2O4 nanoparticles embedded on a flexible graphene composite. *Renew Energy*. 2020;152:634-643. doi:10.1016/j.renene.2020.01.074

40. Khan MR, Uddin MR, Abdullah H, Karim KR, Yousuf A. Preparation and Characterization of CuFe2O4TiO2 Photocatalyst for the Conversion of CO2. *Int J Chem Mol Eng*. 2016;10(10):1273-1280.

41. Rezvani MA, Hadi M, Mirsadri SA. Synthesis of new nanocomposite based on nanoceramic and mono substituted polyoxometalate, PMo11Cd@MnFe2O4, with superior catalytic

activity for oxidative desulfurization of real fuel. *Appl Organomet Chem*. 2020;34(10):1-14. doi:10.1002/aoc.5882

42. Teimouri A, Chermahini AN. An efficient and one-pot synthesis of 2,4,5-trisubstituted and 1,2,4,5-tetrasubstituted imidazoles catalyzed via solid acid nano-catalyst. *J Mol Catal A Chem*. 2011;346(1-2):39-45. doi:10.1016/j.molcata.2011.06.007

43. Rohrer GS. Grain boundary energy anisotropy: A review. *J Mater Sci*. 2011;46(18):5881-5895. doi:10.1007/s10853-011-5677-3

44. Gouvêa D, Castro RHR. Sintering: The role of interface energies. *Appl Surf Sci*. 2003;217(1-4):194-201. doi:10.1016/S0169-4332(03)00539-7

45. Castro RHR, van Benthem K. *Sintering*. Springer; 2013. doi:10.1007/978-3-642-31009-6

46. Siegel RW, Thomas GJ. Grain boundaries in nanophase materials. *Ultramicroscopy*. 1992;40:376-384.

47. Castro RHR. On the thermodynamic stability of nanocrystalline ceramics. *Mater Lett*. 2013;96:45-56. doi:10.1016/j.matlet.2013.01.007

48. Joo SH, Bae JW, Park WY, et al. Beating Thermal Coarsening in Nanoporous Materials via High-Entropy Design. *Adv Mater*. 2020;32(6):1-9. doi:10.1002/adma.201906160

49. Terwllliger CD, Chiang Y -M. Measurements of Excess Enthalpy in Ultrafine-Grained Titanium Dioxide. *J Am Ceram Soc*. 1995;78(8):2045-2055. doi:10.1111/j.1151-2916.1995.tb08616.x

50. Hasan MM, Dholabhai PP, Dey S, Uberuaga BP, Castro RHR. Reduced grain boundary energies in rare-earth doped MgAl2O4 spinel and consequent grain growth inhibition. *J Eur Ceram Soc*. 2017;37(13):4043-4050. doi:10.1016/j.jeurceramsoc.2017.04.073

51. Dey S, Chang CH, Gong M, Liu F, Castro RHR. Grain growth resistant nanocrystalline zirconia by targeting zero grain boundary energies. *J Mater Res*. 2015;30(20):2991-3002. doi:10.1557/jmr.2015.269

52. Nafsin N, Aguiar JA, Aoki T, Thron AM, van Benthem K, Castro RHR. Thermodynamics versus kinetics of grain growth control in nanocrystalline zirconia. *Acta Mater*.

2017;136:224-234. doi:10.1016/j.actamat.2017.07.005

53. Nakajima K, Li H, Shlesinger N, Rodrigues Neto JB, Castro RHR. Low-temperature sintering of magnesium aluminate spinel doped with manganese: Thermodynamic and kinetic aspects. *J Am Ceram Soc*. 2020;103(8):4167-4177. doi:10.1111/jace.17162

54. Nakajima K, Dahl S, Thron A, Castro RHR. Thermodynamic and kinetic analyses of sintering in Al-doped Y2O3 nanoparticles. *J Am Ceram Soc*. 2022;105(1):147-158. doi:10.1111/jace.18083

55. Muche DNF, da Silva AL, Nakajima K, Gouvêa D, Castro RHR. Simultaneous segregation of lanthanum to surfaces and grain boundaries in MgAl2O4 nanocrystals. *Appl Surf Sci*. 2020;529(June). doi:10.1016/j.apsusc.2020.147145

56. Roy TK, Ghosh A, Bhowmick D, Sanyal D, Koley S, Chakrabarti A. Effect of silica doping on the densification and grain growth in zinc oxide. *Ceram Int*. 2011;37(7):2679-2687. doi:10.1016/j.ceramint.2011.04.017

57. Ruiz AM, Cornet A, Morante JR. Study of La and Cu influence on the growth inhibition and phase transformation of nano-TiO2 used for gas sensors. *Sensors Actuators, B Chem*. 2004;100(1-2):256-260. doi:10.1016/j.snb.2003.12.043

58. Liu F, Kirchheim R. Nano-scale grain growth inhibited by reducing grain boundary energy through solute segregation. *J Cryst Growth*. 2004;264(1-3):385-391. doi:10.1016/j.jcrysgro.2003.12.021

59. Li Y, Raabe D, Herbig M, et al. Segregation stabilizes nanocrystalline bulk steel with near theoretical strength. *Phys Rev Lett*. 2014;113(10):1-5. doi:10.1103/PhysRevLett.113.106104

60. Özerinç S, Tai K, Vo NQ, Bellon P, Averback RS, King WP. Grain boundary doping strengthens nanocrystalline copper alloys. *Scr Mater*. 2012;67(7-8):720-723. doi:10.1016/j.scriptamat.2012.06.031

61. Liu H, Huang J, Wang C, et al. Effects of grain boundaries and nano-precipitates on helium bubble behaviors in lanthanum-doped nanocrystalline steel. *Scr Mater*. 2021;200:113900. doi:10.1016/j.scriptamat.2021.113900

62. Asgharzadeh H, Mcqueen HJ, Asgharzadeh H, Mcqueen HJ. Grain growth and stabilisation of nanostructured aluminium at high temperatures : review Grain growth and stabilisation of nanostructured aluminium at high temperatures : review. 2015;0836. doi:10.1179/1743284714Y.0000000706

63. Li H, Dey S, Castro RHR. Kinetics and thermodynamics of densification and grain growth: Insights from lanthanum doped zirconia. *Acta Mater*. 2018;150:394-402. doi:10.1016/j.actamat.2018.03.033

64. Bokov A, Zhang S, Feng L, Dillon SJ, Faller R, Castro RHR. Energetic design of grain boundary networks for toughening of nanocrystalline oxides. *J Eur Ceram Soc*. 2018;38(12):4260-4267. doi:10.1016/j.jeurceramsoc.2018.05.007

65. Michels A, Krill CE, Ehrhardt H, Birringer R, Wu DT. Modelling the influence of grain-size-dependent solute drag on the kinetics of grain growth in nanocrystalline materials. *Acta Mater*. 1999;47(7):2143-2152. doi:10.1016/S1359-6454(99)00079-8

66. Guo D, Song S, Luo R, et al. Grain Boundary Sliding and Amorphization are Responsible for the Reverse Hall-Petch Relation in Superhard Nanocrystalline Boron Carbide. *Phys Rev Lett*. 2018;121(14):1-6. doi:10.1103/PhysRevLett.121.145504

67. Qi ZB, Sun P, Zhu FP, Wang ZC, Peng DL, Wu CH. The inverse Hall-Petch effect in nanocrystalline ZrN coatings. *Surf Coatings Technol*. 2011;205(12):3692-3697. doi:10.1016/j.surfcoat.2011.01.021

68. Szlufarska I, Nakano A, Vashishta P. Materials science: A crossover in the mechanical response of nanocrystalline ceramics. *Science (80-)*. 2005;309(5736):911-914. doi:10.1126/science.1114411

69. Wang Y, Zhang J, Zhao Y. Strength weakening by nanocrystals in ceramic materials. *Nano Lett*. 2007;7(10):3196-3199. doi:10.1021/nl0718723

70. Bokov A, Rodrigues Neto JB, Lin F, Castro RHR. Size-induced grain boundary energy increase may cause softening of nanocrystalline yttria-stabilized zirconia. *J Am Ceram Soc*. 2020;103(3):2001-2011. doi:10.1111/jace.16886

71. Conrad H, Narayan J. Mechanism for grain size softening in nanocrystalline Zn. *Appl Phys*

Lett. 2002;81(12):2241-2243. doi:10.1063/1.1507353

72. Weertman JR. Hall-Petch strengthening in nanocrystalline metals. *Mater Sci Eng A*. 1993;166(1-2):161-167. doi:10.1016/0921-5093(93)90319-A

73. Giga A, Kimoto Y, Takigawa Y, Higashi K. Demonstration of an inverse Hall-Petch relationship in electrodeposited nanocrystalline Ni-W alloys through tensile testing. *Scr Mater*. 2006;55(2):143-146. doi:10.1016/j.scriptamat.2006.03.047

74. Lu K, Wei WD. Microhardness and fracture properties of nanocrystalline Ni-P alloy. *Scr Metall Mater*. 1990;24(c):2319-2323.

75. Hahn H, Mondal P, Padmanabhan KA. Plastic deformation of nanocrystalline materials. *Nanostructured Mater*. 1997;9(1-8):603-606. doi:10.1016/S0965-9773(97)00135-9

76. Masumura RA, Hazzledine PM, Pande CS. Yield stress of fine grained materials. *Acta Mater*. 1998;46(13):4527-4534. doi:10.1016/S1359-6454(98)00150-5

77. Chen B, Huang Y, Xu J, et al. Revealing the ductility of nanoceramic MgAl2O4. *J Mater Res*. 2019;34(9):1489-1498. doi:10.1557/jmr.2019.114

78. Cottom BA, Mayo MJ. Fracture toughness of nanocrystalline ZrO2-3mol% y2o3 determined by vickers indentation. *Scr Mater*. 1996;34(5):809-814. doi:10.1016/1359-6462(95)00587-0

79. Kaminskiĭ AA, Akchurin MS, Gaĭnutdinov R V., et al. Microhardness and fracture toughness of Y2O3- and Y3Al5O12-based nanocrystalline laser ceramics. *Crystallogr Reports*. 2005;50(5):869-873. doi:10.1134/1.2049410

80. Ostojic P, McPherson R. A review of indentation fracture theory: its development, principles and limitations. *Int J Fract*. 1987;33(4):297-312. doi:10.1007/BF00044418

81. Ovid'ko IA. Review on the fracture processes in nanocrystalline materials. *J Mater Sci*. 2007;42(5):1694-1708. doi:10.1007/s10853-006-0968-9

82. Asta M, Kauzlarich SM, Liu K, Navrotsky A, Osterloh FE. Inorganic Nanoparticles — Unique Properties and Novel Applications. *Mater Matters*. 2011;2(1):2-6.

83. Mohamed FA, Li Y. Creep and superplasticity in nanocrystalline materials: Current

understanding and future prospects. *Mater Sci Eng A*. 2001;298(1-2):1-15. doi:10.1016/S0928-4931(00)00190-9

84. Chokshi AH. Grain Boundary Processes in Strengthening, Weakening, and Superplasticity. *Adv Eng Mater*. 2020;22(1):1-9. doi:10.1002/adem.201900748

85. Krill CE, Ehrhardt H, Birringer R. Thermodynamic stabilization of nanocrystallinity. *Int J Mater Res*. 2005;96:1134-1141.

86. Kingery WD. Plausible Concepts Necessary and Sufficient for Interpretation of Ceramic Grain-Boundary Phenomena: II, Solute Segregation, Grain-Boundary Diffusion, and General Discussion. *J Am Ceram Soc*. 1974;57(2):74-83. doi:10.1111/j.1151-2916.1974.tb10818.x

87. Chen S, Avila-Paredes HJ, Kim S, Zhao J, Munir Z, Navrotsky A. Direct calorimetric measurement of grain boundary and surface enthalpies in yttria-stabilized zirconia. *Phys Chem Chem Phys*. 2009;11(17):3039-3042. doi:10.1039/b905911n

88. Costa GCC, Ushakov S V., Castro RHR, Navrotsky A, Muccillo R. Calorimetric measurement of surface and interface enthalpies of Yttria-Stabilized Zirconia (YSZ). *Chem Mater*. 2010;22(9):2937-2945. doi:10.1021/cm100255u

89. Chen S, Costa GCC, Wang S, Munir ZA, Kim S, Navrotsky A. Grain-boundary enthalpies of cubic yttria-stabilized zirconia. *J Am Ceram Soc*. 2011;94(7):2181-2184. doi:10.1111/j.1551-2916.2010.04365.x

90. Li H, Souza FL, Castro RHR. Kinetic and thermodynamic effects of manganese as a densification aid in yttria-stabilized zirconia. *J Eur Ceram Soc*. 2018;38(4):1750-1759. doi:10.1016/j.jeurceramsoc.2017.10.041

91. Pereira GJ, Bolis K, Muche DNF, Gouvêa D, Castro RHR. Direct measurement of interface energies of magnesium aluminate spinel and a brief sintering analysis. *J Eur Ceram Soc*. 2017;37(13):4051-4058. doi:10.1016/j.jeurceramsoc.2017.05.035

92. Kirchheim R. Reducing grain boundary, dislocation line and vacancy formation energies by solute segregation. II. Experimental evidence and consequences. *Acta Mater*. 2007;55(15):5139-5148. doi:10.1016/j.actamat.2007.05.033

93. Bokov A, Aguiar JA, Gong ML, Nikonov A, Castro RHR. A Strategy to Mitigate Grain Boundary Blocking in Nanocrystalline Zirconia. *J Phys Chem C*. 2018;122(46):26344-26352. doi:10.1021/acs.jpcc.8b08877

94. Yan MF, Cannon RM, Bowen HK. Space charge, elastic field, and dipole contributions to equilibrium solute segregation at interfaces. *J Appl Phys*. 1983;54(2):764-778. doi:10.1063/1.332035

95. Chiang Y -M, Kingery WD. Grain-Boundary Migration in Nonstoichiometric Solid Solutions of Magnesium Aluminate Spinel: II, Effects of Grain-Boundary Nonstoichiometry. *J Am Ceram Soc*. 1990;73(5):1153-1158. doi:10.1111/j.1151-2916.1990.tb05172.x

96. Chiang Y -M, Kingery WD. Grain-Boundary Migration in Nonstoichiometric Solid Solutions of Magnesium Aluminate Spinel: I, Grain Growth Studies. *J Am Ceram Soc*. 1989;72(2):271-277. doi:10.1111/j.1151-2916.1989.tb06113.x

97. Halabi M, Ezersky V, Kohn A, Hayun S. Charge distribution in nano-scale grains of magnesium aluminate spinel. *J Am Ceram Soc*. 2017;100(2):800-811. doi:10.1111/jace.14610

98. Nakajima K, Souza FL, Freitas ALM, Thron A, Castro RHR. Improving Thermodynamic Stability of nano-LiMn2O4for Li-Ion Battery Cathode. *Chem Mater*. 2021;33(11):3915-3925. doi:10.1021/acs.chemmater.0c04305

99. Chiang Y, Dunbar PB, Kingery WD. *Physical Ceramics: Principles for Ceramic Science and Engineering*. 409th ed. New York: Wiley; 1997.

100. Wu L, Dey S, Gong M, Liu F, Castro RHR. Surface segregation on manganese doped ceria nanoparticles and relationship with nanostability. *J Phys Chem C*. 2014;118(51):30187-30196. doi:10.1021/jp508663p

101. Lifshitz I, Slyozov V. The Kinetics of Precipitation from Supersaturated Solid Solutions. *J Phys Chem Solids*. 1961;19:35-50.

102. Ting CJ, Lu HY. Defect reactions and the controlling mechanism in the sintering of magnesium aluminate spinel. *J Am Ceram Soc*. 1999;82(4):841-848. doi:10.1111/j.1151-

2916.1999.tb01844.x

103. Gouvêa D, Pereira GJ, Gengembre L, et al. Quantification of MgO surface excess on the SnO 2 nanoparticles and relationship with nanostability and growth. *Appl Surf Sci*. 2011;257(9):4219-4226. doi:10.1016/j.apsusc.2010.12.023

104. Hasan MM, Dey S, Nafsin N, et al. Improving the Thermodynamic Stability of Aluminate Spinel Nanoparticles with Rare Earths. *Chem Mater*. 2016;28(14):5163-5171. doi:10.1021/acs.chemmater.6b02577

105. Koch CC, Narayan J. The inverse Hall-Petch effect - Fact or artifact? *Mater Res Soc Symp - Proc*. 2001;634:1-11. doi:10.1557/proc-634-b5.1.1

106. Trunec M, Chlup Z. Higher fracture toughness of tetragonal zirconia ceramics through nanocrystalline structure. *Scr Mater*. 2009;61(1):56-59. doi:10.1016/j.scriptamat.2009.03.019

107. Lawn BR, Swain M V. Microfracture beneath point indentations in brittle solids. *J Mater Sci*. 1975;10(1):113-122. doi:10.1007/BF00541038

108. Mitchell TE, Lagerlöf KPD, Heuer AH, Lagerlöf KPD, Dislocations AHH. Dislocations in ceramics. 2013;0836(1985). doi:10.1179/mst.1985.1.11.944

109. Conrad H, Narayan J. On the grain size softening in nanocrystalline materials. *Scr Mater*. 2000;42(11):1025-1030. doi:10.1016/S1359-6462(00)00320-1

110. Hu J, Shi YN, Sauvage X, Sha G, Lu K. Grain boundary stability governs hardening and softening in extremely fine nanograined metals. *Science (80-)*. 2017;355(6331):1292-1296. doi:10.1126/science.aal5166

111. Koch CC, Cho YS. Nanocrystals by high energy ball milling. *Nanostructured Mater*. 1992;1:207-212.

112. Qin XY, Wu XJ, Zhang LD. The microhardness of nanocrystalline silver. *Nanostructured Mater*. 1995;5(1):101-110. doi:10.1016/0965-9773(95)00003-W

113. Yuan R, Beyerlein IJ, Zhou C. Coupled crystal orientation-size effects on the strength of nano crystals. *Sci Rep*. 2016;6:1-9. doi:10.1038/srep26254

114. Ehre D, Chaim R. Abnormal Hall-Petch behavior in nanocrystalline MgO ceramic. *J Mater Sci*. 2008;43(18):6139-6143. doi:10.1007/s10853-008-2936-z

115. Conrad H. Grain-size dependence of the flow stress of Cu from millimeters to nanometers. *Metall Mater Trans A*. 2004;35A:2681-2695.

116. Chokshi AH, Rosen A, Karch J, Fleiter H. On the validity of the Hall-Petch relationship in nanocrystalline materials. *Scr Metall*. 1989;23:1679-1684.

117. Halabi M, Ezersky V, Kohn A, Hayun S. Charge distribution in nano-scale grains of magnesium aluminate spinel. 2017;(June 2016):800-811. doi:10.1111/jace.14610

118. Yang C, Zhu W, Sen S, Castro RHR. Site Inversion Induces Thermodynamic Stability against Coarsening in Zinc Aluminate Spinel. *J Phys Chem C*. 2019;123(14):8818-8826. doi:10.1021/acs.jpcc.8b11378

119. Schaffer M, Schaffer B, Ramasse Q. Sample preparation for atomic-resolution STEM at low voltages by FIB. *Ultramicroscopy*. 2012;114:62-71. doi:10.1016/j.ultramic.2012.01.005

120. Baram M, Kaplan WD. Quantitative HRTEM analysis of FIB prepared specimens. *J Microsc*. 2008;232(3):395-405. doi:10.1111/j.1365-2818.2008.02134.x

121. Sokol M, Meir S, Strumza E, Kalabukhov S, Hayun S, Frage N. On the effects of LiF on the synthesis and reactive sintering of gahnite (ZnAl2O4). *Ceram Int*. 2017;43(17):14891-14896. doi:10.1016/j.ceramint.2017.08.005

122. Pabst W, Hostaša J, Esposito L. Porosity and pore size dependence of the real in-line transmission of YAG and alumina ceramics. *J Eur Ceram Soc*. 2014;34(11):2745-2756. doi:10.1016/j.jeurceramsoc.2013.12.053

123. Feng Q, Song X, Liu X, Liang S, Wang H, Nie Z. Compression deformation of WC: Atomistic description of hard ceramic material. *Nanotechnology*. 2017;28(47). doi:10.1088/1361-6528/aa9270

124. Sheinerman AG, Castro RHR, Gutkin MY. A model for direct and inverse Hall-Petch relation for nanocrystalline ceramics. *Mater Lett*. 2020;260:126886.

doi:10.1016/j.matlet.2019.126886

125. Lawn B, Wilshaw R. Indentation fracture: principles and applications. *J Mater Sci*. 1975;10(6):1049-1081. doi:10.1007/BF00823224

126. Pun SC, Wang W, Khalajhedayati A, Schuler JD, Trelewicz JR, Rupert TJ. Nanocrystalline Al-Mg with extreme strength due to grain boundary doping. *Mater Sci Eng A*. 2017;696(November 2016):400-406. doi:10.1016/j.msea.2017.04.095

127. Otero Areán C, Sintes Sintes B, Turnes Palomino G, Mas Carbonell C, Escalona Platero E, Parra Soto JB. Preparation and characterization of spinel-type high surface area Al2O3-ZnAl2O4 mixed metal oxides by an alkoxide route. *Microporous Mater*. 1997;8(3-4):187-192. doi:10.1016/S0927-6513(96)00073-9

128. Li X, Zhu Z, Zhao Q, Wang L. Photocatalytic degradation of gaseous toluene over ZnAl2O4 prepared by different methods: A comparative study. *J Hazard Mater*. 2011;186(2-3):2089-2096. doi:10.1016/j.jhazmat.2010.12.111

129. Zhu Z, Zhao Q, Li X, et al. Photocatalytic performances and activities of ZnAl2O4 nanorods loaded with Ag towards toluene. *Chem Eng J*. 2012;203:43-51. doi:10.1016/j.cej.2012.07.035

130. Wrzyszcz J, Zawadzki M, Trzeciak AM, Ziółkowski JJ. Rhodium complexes supported on zinc aluminate spinel as catalysts for hydroformylation and hydrogenation: Preparation and activity. *J Mol Catal A Chem*. 2002;189(2):203-210. doi:10.1016/S1381-1169(02)00073-0

131. Wrzyszcz J, Zawadzki M, Trzeciak AM, Tylus W, Ziółkowski JJ. Catalytic activity of rhodium complexes supported on Al2O3-ZrO2 in isomerization and hydroformylation of 1-hexene. *Catal Letters*. 2004;93(1-2):85-92. doi:10.1023/b:catl.0000016954.95871.bb

132. Zhang X, Zhang G, Liu W, et al. Reaction-driven surface reconstruction of ZnAl2O4 boosts the methanol selectivity in CO2 catalytic hydrogenation. *Appl Catal B Environ*. 2021;284(October 2020):119700. doi:10.1016/j.apcatb.2020.119700

133. Huš M, Dasireddy VDBC, Strah Štefančič N, Likozar B. Mechanism, kinetics and thermodynamics of carbon dioxide hydrogenation to methanol on Cu/ZnAl2O4 spinel-type heterogeneous catalysts. *Appl Catal B Environ*. 2017;207:267-278.

doi:10.1016/j.apcatb.2017.01.077

134. Pandey R, Gale JD, Sampath SK, Recio JM. Atomistic simulation study of spinel oxides: Zinc aluminate and zinc gallate. *J Am Ceram Soc*. 1999;82(12):3337-3341. doi:10.1111/j.1151-2916.1999.tb02248.x

135. Zawadzki M, Miśta W, Kępiński L. Metal-support effects of platinum supported on zinc aluminate. *Vacuum*. 2001;63(1-2):291-296. doi:10.1016/S0042-207X(01)00204-4

136. Zhang C, Wang K, Liu C, et al. Effects of high surface energy on lithium-ion intercalation properties of Ni-doped Li3VO4. *NPG Asia Mater*. 2016;8(7):1-7. doi:10.1038/am.2016.95

137. Wang F, Richards VN, Shields SP, Buhro WE. Kinetics and Mechanisms of Aggregative Nanocrystal Growth. *Chem Mater*. 2014;26(1):5-21. doi:10.1021/cm402139r

138. Castro RHR, Gouvêa D. Sintering and Nanostability: The Thermodynamic Perspective. *J Am Ceram Soc*. 2016;99(4):1105-1121. doi:10.1111/jace.14176

139. Chen XY, Ma C, Zhang ZJ, Wang BN. Ultrafine gahnite (ZnAl2O4) nanocrystals: Hydrothermal synthesis and photoluminescent properties. *Mater Sci Eng B*. 2008;151(3):224-230.

140. Hansen TW, Delariva AT, Challa SR, Datye AK. Sintering of catalytic nanoparticles: Particle migration or ostwald ripening? *Acc Chem Res*. 2013;46(8):1720-1730. doi:10.1021/ar3002427

141. Baldan A. Progress in Ostwald ripening theories and their applications to nickel-base superalloys. Part I: Ostwald ripening theories. *J Mater Sci*. 2002;37:2171-2202. https://link.springer.com/content/pdf/10.1023%2FA%3A1015388912729.pdf.

142. Thanh NTK, Maclean N, Mahiddine S. Mechanisms of nucleation and growth of nanoparticles in solution. *Chem Rev*. 2014;114(15):7610-7630. doi:10.1021/cr400544s

143. Castro RHR, Hidalgo P, Muccillo R, Gouvêa D. Microstructure and structure of NiO-SnO 2 and Fe 2 O 3 -SnO 2 systems. *Appl Surf Sci*. 2003;214(1-4):172-177. doi:10.1016/S0169-4332(03)00274-5

144. Stukowski A. Visualization and analysis of atomistic simulation data with OVITO-the Open

Visualization Tool. *Model Simul Mater Sci Eng*. 2010;18(1). doi:10.1088/0965-0393/18/1/015012

145. Plimpton S. Fast Parallel Algorithms for Short-Range Molecular Dynamics. *J Comput Phys*. 1995;117:1-19.

146. Buckingham RA. The classical equation of state of gaseous helium , neon and argon. *Proc R Soc Lond A*. 1938;168:264-283.

147. Grimes RW, Busker G, McCoy MA, Chroneos A, Kilner JA, Chen SP. The effect of ion size on solution mechanism and defect cluster geometry. *Berichte der Bunsengesellschaft/Physical Chem Chem Phys*. 1997;101(9):1204-1210. doi:10.1002/bbpc.199700026

148. Busker G, Chroneos A, Grimes RW, Chen IW. Solution mechanisms for dopant oxides in yttria. *J Am Ceram Soc*. 1999;82(6):1553-1559. doi:10.1111/j.1151-2916.1999.tb01954.x

149. Migliorati V, Serva A, Terenzio FM, D'Angelo P. Development of Lennard-Jones and Buckingham Potentials for Lanthanoid Ions in Water. *Inorg Chem*. 2017;56(11):6214-6224. doi:10.1021/acs.inorgchem.7b00207

150. Valenzuela MA, Bosch P, Aguilar-Rios G, Montoya A, Schifter I. Comparison between Sol-Gel, Coprecipitation and Wet Mixing Synthesis of ZnAl2O4. *J Sol-Gel Sci Technol*. 1997;8(1-3):107-110. doi:10.1007/BF02436826

151. Sunder S, Rohilla S, Kumar S, Aghamkar P. Structural characterization of spinel zinc aluminate nanoparticles prepared by coprecipitation method. *AIP Conf Proc*. 2011;1393(December 2011):123-124. doi:10.1063/1.3653640

152. Sotelo Martin LE, Castro RHR. Al excess extends Hall-Petch relation in nanocrystalline zinc aluminate. *J Am Ceram Soc*. 2022;105(2):1417-1427. doi:10.1111/jace.18176

153. Levy D, Pavese A, Sani A, Pischedda V. Structure and compressibility of synthetic ZnAl2O4 (gahnite) under high-pressure conditions, from synchrotron X-ray powder diffraction. *Phys Chem Miner*. 2001;28(9):612-618. doi:10.1007/s002690100194

154. Xin C, Hu M, Wang K, Wang X. Significant Enhancement of Photocatalytic Reduction of

CO2 with H2O over ZnO by the Formation of Basic Zinc Carbonate. *Langmuir*. 2017;33(27):6667-6676. doi:10.1021/acs.langmuir.7b00620

155. Sawada Y, Murakami M, Nishide T. Thermal analysis of basic zinc carbonate. Part 1. Carbonation process of zinc oxide powders at 8 and 13°C. *Thermochim Acta*. 1996;273(1-2):95-102. doi:10.1016/0040-6031(95)02631-2

156. Quach D V., Bonifacio AR, Castro RHR. Water adsorption and interface energetics of zinc aluminate spinel nanoparticles: Insights on humidity effects on nanopowder processing and catalysis. *J Mater Res*. 2013;28(15):2004-2011. doi:10.1557/jmr.2013.192

157. Drazin JW, Castro RHR. Water adsorption microcalorimetry model: Deciphering surface energies and water chemical potentials of nanocrystalline oxides. *J Phys Chem C*. 2014;118(19):10131-10142. doi:10.1021/jp5016356

158. Castro RHR, Quach D V. Analysis of anhydrous and hydrated surface energies of gamma-Al 2O3 by water adsorption microcalorimetry. *J Phys Chem C*. 2012;116(46):24726-24733. doi:10.1021/jp309319j

159. Nakajima K, Castro RHR. Thermodynamics and kinetics of sintering of Y2O3. *J Am Ceram Soc*. 2020;103(9):4903-4912. doi:10.1111/jace.17273

160. Cai Q, Wang JG, Wang Y, Mei D. First-Principles Thermodynamics Study of Spinel MgAl2O4 Surface Stability. *J Phys Chem C*. 2016;120(34):19087-19096. doi:10.1021/acs.jpcc.6b02998

161. Santos-Carballal D, Roldan A, Grau-Crespo R, de Leeuw NH. A DFT study of the structures, stabilities and redox behaviour of the major surfaces of magnetite Fe3O4. *Phys Chem Chem Phys*. 2014;16(39):21082-21097. doi:10.1039/c4cp00529e

162. Kim S, Aykol M, Wolverton C. Surface phase diagram and stability of (001) and (111) LiM n2 O4 spinel oxides. *Phys Rev B - Condens Matter Mater Phys*. 2015;92(11):7-10. doi:10.1103/PhysRevB.92.115411

163. Jiang S, Liu J, Bai L, et al. Anomalous compression behaviour in Nd2O3 studied by x-ray diffraction and Raman spectroscopy. *AIP Adv*. 2018;8(2). doi:10.1063/1.5018020

164. Hummer DR, Kubicki JD, Kent PRC, Post JE, Heaney PJ. Origin of nanoscale phase stability reversals in titanium oxide polymorphs. *J Phys Chem C*. 2009;113(11):4240-4245. doi:10.1021/jp811332w

165. Duan XL, Song CF, Wu YC, Yu FP, Cheng XF, Yuan DR. Preparation and optical properties of nanoscale MgAl2O4 powders doped with Co2+ ions. *J Non Cryst Solids*. 2008;354(29):3516-3519. doi:10.1016/j.jnoncrysol.2008.03.011

166. He F, He Z, Xie J, Li Y. IR and Raman Spectra Properties of Bi2O3-ZnO-B2O3-BaO Quaternary Glass System. *Am J Anal Chem*. 2014;05(16):1142-1150. doi:10.4236/ajac.2014.516121

167. Cao YC, Zhao L, Luo J, et al. Plasma etching behavior of Y 2 O 3 ceramics: Comparative study with Al 2 O 3. *Appl Surf Sci*. 2016;366(9):304-309. doi:10.1016/j.apsusc.2016.01.092

168. Degen A, Kosec M. Effect of pH and impurities on the surface charge of zinc oxide in aqueous solution. *J Eur Ceram Soc*. 2000;20(6):667-673. doi:10.1016/S0955-2219(99)00203-4

169. Rockenhäuser C, Rowolt C, Milkereit B, Darvishi Kamachali R, Kessler O, Skrotzki B. On the long-term aging of S-phase in aluminum alloy 2618A. *J Mater Sci*. 2021;56(14):8704-8716. doi:10.1007/s10853-020-05740-x

170. Limaye AU, Helble JJ. Morphological control of zirconia nanoparticles through combustion aerosol synthesis. *J Am Ceram Soc*. 2002;85(5):1127-1132. doi:10.1111/j.1151-2916.2002.tb00233.x

171. Kuper A, Letaw H, Slifkin L, Sonder E, Tomizuka CT. Self-diffusion in copper. *Phys Rev*. 1954;96(5):1224-1225. doi:10.1103/PhysRev.96.1224

172. Izaki T, Haneda H, Wataneba A, Tanaka J, Shirasaki S, Tsuji K. Self diffusion of oxygen in PLZT ceramics. 1993;101(1):133-138.

173. Zhong M, Guo Y, Wang J, et al. Facile preparation of highly thermal conductive ZnAl2O4@Al composites as efficient supports for cobalt-based Fischer-Tropsch synthesis. *Fuel*. 2019;253(May):1499-1511. doi:10.1016/j.fuel.2019.05.124

174. Bravo-Leon A, Morikawa Y, Kawahara M, Mayo MJ. Fracture toughness of nanocrystalline tetragonal zirconia with low yttria content. *Acta Mater*. 2002;50(18):4555-4562. doi:10.1016/S1359-6454(02)00283-5

175. Casellas D, Nagl MM, Llanes L, Anglada M. Fracture toughness of alumina and ZTA ceramics: Microstructural coarsening effects. *J Mater Process Technol*. 2003;143-144(1):148-152. doi:10.1016/S0924-0136(03)00396-0

176. Ogawa H. GBstudio: A builder software on periodic models of CSL boundaries for molecular simulation. *Mater Trans*. 2006;47(11):2706-2710. doi:10.2320/matertrans.47.2706

177. Viana KMS, Dantas BB, Nogueira NAS, et al. Influence of fuel in the synthesis of ZnAl2O4 catalytic supports by combustion reaction. *Mater Sci Forum*. 2010;660-661:52-57. doi:10.4028/www.scientific.net/MSF.660-661.52

178. Holzwarth U, Gibson N. The Scherrer equation versus the "Debye-Scherrer equation." *Nat Nanotechnol*. 2011;6(9):534. doi:10.1038/nnano.2011.145

179. Quach D V., Castro RHR. Direct measurement of grain boundary enthalpy of cubic yttria-stabilized zirconia by differential scanning calorimetry. *J Appl Phys*. 2012;112(8):3-8. doi:10.1063/1.4761992

180. Bhattacharjee PP, Sinha SK, Upadhyaya A. Effect of sintering temperature on grain boundary character distribution in pure nickel. *Scr Mater*. 2007;56(1):13-16. doi:10.1016/j.scriptamat.2006.09.003

181. Muche DNF, Marple MAT, Sen S, Castro RHR. Grain boundary energy, disordering energy and grain growth kinetics in nanocrystalline MgAl2O4 spinel. *Acta Mater*. 2018;149:302-311. doi:10.1016/j.actamat.2018.02.052

182. Navrotsky A. Cation-distribution energetics and heats of mixing in MgFe2O4-MgAl2O4, ZnFe2O4-ZnAl2O4, and NiAl2O4-ZnAl2O4 spinels; study by high-temperature calorimetry. *Am Mineral*. 1986;71(9-10):1160-1169.

183. Znal O, Sokol M, Meir S, et al. On the effects of LiF on the synthesis and reactive sintering of gahnite. 2017;43(August):14891-14896. doi:10.1016/j.ceramint.2017.08.005

184. Yong X, Ping F, Baohua Z, Juan G, Lin Z, Xuehua W. Optical properties of transparent ZnAl 2 O 4 ceramics : A new transparent material prepared by spark plasma sintering. *Mater Lett*. 2014;123:142-144. doi:10.1016/j.matlet.2014.03.013

185. van der Laag NJ, Snel MD, Magusin PCMM, With G De. Structural , elastic , thermophysical and dielectric properties of zinc aluminate (ZnAl 2 O 4). 2004;24:2417-2424. doi:10.1016/j.jeurceramsoc.2003.06.001

186. Lankford J. Indentation microfracture in the Palmqvist crack regime: implications for fracture toughness evaluation by the indentation method. *J Mater Sci Lett*. 1982;1(11):493-495. doi:10.1007/BF00721938

187. Laugier MT. New formula for indentation toughness in ceramics. *J Mater Sci Lett*. 1987;6(3):355-356. doi:10.1007/BF01729352

188. Shetty DK, Wright IG, Mincer PN, Clauer AH. Indentation fracture of WC-Co cermets. *J Mater Sci*. 1985;20(5):1873-1882. doi:10.1007/BF00555296

189. Perevezentsev VN, Pupynin AS, Ogorodnikov AE. Nanopore Evolution Kinetics during Annealing of Submicrocrystalline Materials. *Tech Phys*. 2018;63(10):1492-1496. doi:10.1134/S1063784218100171

190. Ovid'ko IA, Sheinerman AG. Triple junction nanocracks in deformed nanocrystalline materials. *Acta Mater*. 2004;52(5):1201-1209. doi:10.1016/j.actamat.2003.11.004

191. Justo JF, Schmidt TM, Fazzio A, Antonelli A. Segregation of dopant atoms on extended defects in semiconductors. *Phys B Condens Matter*. 2001;302-303:403-407. doi:10.1016/S0921-4526(01)00462-8

192. Birringer R. Nanocrystalline Materials. *Mater Sci Eng A*. 1989;117:33-43. doi:10.1016/B978-0-08-044697-4.X5013-3